LEABHARLANN CHOLÁISTE NA TRÍONÓIDE, BAILE ÁTHA CLIATH | TRINITY COLLEGE LIBRARY DUBLIN
Ollscoil Átha Cliath | The University of Dublin

Terms and Conditions of Use of Digitised Theses from Trinity College Library Dublin

Copyright statement

All material supplied by Trinity College Library is protected by copyright (under the Copyright and Related Rights Act, 2000 as amended) and other relevant Intellectual Property Rights. By accessing and using a Digitised Thesis from Trinity College Library you acknowledge that all Intellectual Property Rights in any Works supplied are the sole and exclusive property of the copyright and/or other IPR holder. Specific copyright holders may not be explicitly identified. Use of materials from other sources within a thesis should not be construed as a claim over them.

A non-exclusive, non-transferable licence is hereby granted to those using or reproducing, in whole or in part, the material for valid purposes, providing the copyright owners are acknowledged using the normal conventions. Where specific permission to use material is required, this is identified and such permission must be sought from the copyright holder or agency cited.

Liability statement

By using a Digitised Thesis, I accept that Trinity College Dublin bears no legal responsibility for the accuracy, legality or comprehensiveness of materials contained within the thesis, and that Trinity College Dublin accepts no liability for indirect, consequential, or incidental, damages or losses arising from use of the thesis for whatever reason. Information located in a thesis may be subject to specific use constraints, details of which may not be explicitly described. It is the responsibility of potential and actual users to be aware of such constraints and to abide by them. By making use of material from a digitised thesis, you accept these copyright and disclaimer provisions. Where it is brought to the attention of Trinity College Library that there may be a breach of copyright or other restraint, it is the policy to withdraw or take down access to a thesis while the issue is being resolved.

Access Agreement

By using a Digitised Thesis from Trinity College Library you are bound by the following Terms & Conditions. Please read them carefully.

I have read and I understand the following statement: All material supplied via a Digitised Thesis from Trinity College Library is protected by copyright and other intellectual property rights, and duplication or sale of all or part of any of a thesis is not permitted, except that material may be duplicated by you for your research use or for educational purposes in electronic or print form providing the copyright owners are acknowledged using the normal conventions. You must obtain permission for any other use. Electronic or print copies may not be offered, whether for sale or otherwise to anyone. This copy has been supplied on the understanding that it is copyright material and that no quotation from the thesis may be published without proper acknowledgement.

Theoretical Study of Topological Insulators: Models and Materials

Awadhesh Narayan

A thesis submitted for the degree of
Doctor of Philosophy
School of Physics
Trinity College Dublin

September 2014

Declaration

I, Awadhesh Narayan, hereby declare that this dissertation has not been submitted as an exercise for a degree at this or any other University.

It comprises work performed entirely by myself during the course of my Ph.D. studies at Trinity College Dublin. I was involved in a number of collaborations, and where it is appropriate my collaborators are acknowledged for their contributions.

A copy of this thesis may be lended or copied by the Trinity College Library upon request by a third party provided it spans single copies made for study purposes only, subject to normal conditions of acknowledgement.

Awadhesh Narayan
September, 2014

"Like faint glimmers of light in the dark, we have emerged for a moment from the nothingness of dark unconsciousness of material existence. We must make good the demands of reason and create a life worthy of ourselves and of the goals we only dimly perceive."

-Andrei Sakharov

Abstract

Topological insulators are a fascinating new class of materials, which have signalled a revival in exploration of topological aspects of condensed matter physics. Like usual insulators they have an energy gap separating valence and conduction bands, however, their surfaces host metallic states which cannot be gapped out unless one breaks the symmetry protecting such surface states. Crucially, a number of materials have been identified as time reversal symmetric topological insulators and their surface state signature has been verified by means of a number of experimental techniques. In this thesis we study different aspects of topological states in two and three dimensions, employing both model Hamiltonians as well as material specific first-principles density functional theory calculations.

Firstly, we present our investigation of Andreev reflection in topological insulator-superconductor junctions, finding perfect Andreev reflection, which is robust to disorder. We compare and contrast our results for $\mathbb{Z}_2$ and Chern insulators, and propose a transport experiment to distinguish between the two kinds of insulators. Next, we study spin-flip inelastic electron tunneling spectroscopy for magnetic adatoms deposited at the edge of two-dimensional topological insulator, and find that the impurity spin can be manipulated by passing current through the helical edge states. We also propose a four terminal device which is designed to manipulate the spin of the adatom by

all electrical means.

Then, we present *ab initio* transport studies of scattering of topological states. We investigate electron transmission across surface steps on Sb(111), where we find a good agreement with scanning tunneling microscopy experiments, in particular concerning lifetime of quantum well states and allowed scattering wave vectors. We also study effect of barriers on Bi_2Se_3(111) surface and compare our first-principles results with the often used Dirac-type low-energy model. Then, we report our finding of a single atom anisotropic magentoresistance on topological insulator surface, which stems from an interplay between the helical surface states and spin anisotropy of the magnetic adatom. Our *ab initio* calculations for Mn adatom on Bi_2Se_3 elucidate the underlying mechanism and also reveal the real space spin texture around the magnetic impurity.

Finally we report our investigations of two- and three-dimensional Dirac semimetals. We present our proposal to engineer a backscattering-free hybrid state in graphene by proximity with a three-dimensional topological insulator. Using transport calculations, we further confirm the robustness of this proximity induced state to disorder. Then we study the interplay of bulk and surface Dirac fermions in prototypical three-dimensional Dirac semimetals and reveal a topological phase transition in $Na_3Bi_{1-x}Sb_x$ alloy.

Acknowledgments

During the course of my PhD studies I have received help and support from a number of people and this work would not have been possible without them.

First of all I would like to thank Prof. Stefano Sanvito, who has been a remarkable mentor over the past four years. He introduced me to this wonderful field of Topological Insulators, and has suggested numerous interesting problems for me to work on. Importantly, he gave me complete freedom and encouragement to choose my own problems, while offering valuable advice on tackling them. His strong work ethic and an intuitive ability to reduce complicated problems to simple essentials have inspired me greatly.

Next, I must thank Dr. Ivan Rungger, who has patiently taught me the practical aspects of density functional and transport calculations. I am deeply grateful for his help and advice over the course of my studies. Then I would like to acknowledge Dr. Aaron Hurley, with whom I studied inelastic electron tunneling spectroscopy and who taught me the *ins* and *outs* of many body perturbation theory. I must then acknowledge Dr. Andrea Droghetti who helped me during the first few months of my studies, and we have also worked together on other topics since then. I must then thank Dr. Mauro Mantega and Dr. Igor Popov, with whom I worked on interfacing graphene

with topological insulators. Next, I must thank Dr. Kapildeb Dolui, who kept me informed about the developments in the field of two dimensional materials, and together we explored magnetoresistance in Fe/MoS_2 junctions. Finally, I would like to specially thank Dr. Thomas Archer for his constant help about all matters related to computing.

A special thanks must go to Ms. Stefania Negro, who took care of all the administrative aspects and to Ms. Jeanette Cummins, who provided countless letters for visa applications.

Next, I would like to thank our external collaborators. First of all I must acknowledge Domenico Di Sante and Prof. Silvia Picozzi at University of L'Aquila, with whom I am working on exotic materials GeTe (which is a ferroelectric with a large Rashba splitting) and Na_3Bi (which has a symmetry protected three-dimensional Dirac cone). I would then like to thank Dr. Graham Kells at Dublin Institute of Advanced Studies, who has taught me many things about Majorana fermions. Next, I would like to acknowledge Dr. Mirko Cinchetti and other experimentalists at TU Kaiserslautern, with whom I am exploring the effect of organic molecular layers on topological surface states.

It would not have been possible to undertake research such as this without financial support. I am grateful to the Irish Research Council (EMBARK initiative) for providing funding during my studies. Computational resources for this work were provided by Trinity Centre for High Performance Computing (TCHPC) and Irish Centre for High End Computing (ICHEC). I would also like to thank Dr. Alin Elena for useful discussions and support in using the ICHEC clusters.

I would also like to thank Prof. Jairo Sinova and Prof. Mauro Ferreira for taking time off their busy schedules to examine my thesis.

Finally, I would like to deeply thank my parents Rita Narayan and Akhileshwar Narayan. They have always supported me and encouraged my interest in science. This work is dedicated to them.

Contents

List of Figures

To my parents.

Chapter 1

General Introduction

One of the primary goals of condensed matter physics is to discover and classify different phases of matter. The fundamental building blocks of matter can come together to form a myriad of different states, ranging from crystalline solids to magnets and superconductors. All these can be classified on the basis of Landau's principle of spontaneous symmetry breaking [1]. Crystalline solids break translational symmetry, while a magnet breaks rotational symmetry. A superconductor breaks the more mysterious gauge symmetry. The first state of matter which did not fit into this paradigm was the integer quantum Hall phase discovered in 1980 [2]. Von Klitzing *et al.* took a two-dimensional electron gas sample and passed a current across one of the directions, while they applied a perpendicular magnetic field. In the transverse direction a voltage was generated, a consequence of the usual Hall effect. But at sufficiently low temperatures and sufficiently high magnetic fields, they saw plateaus in the transverse conductivity. In this state, the bulk of a two-dimensional sample is an insulator, while a dissipationless current flows only at the edges of the sample. Even more surprising was the fact that the quantization of conductivity was extremely precise, of the order of one part in a billion. Furthermore it was independent of the sample material,

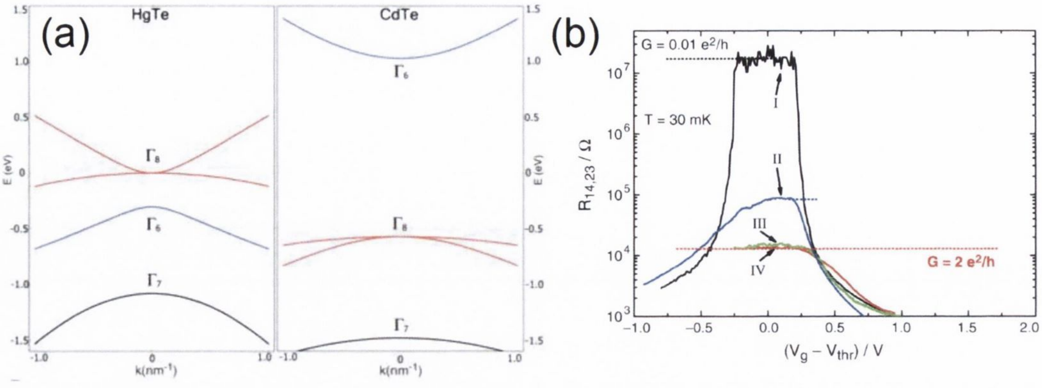

Figure 1.1: (a) Schematic band diagram for HgTe and CdTe near the Γ point showing the inverted band structure for HgTe. (b) Quantized edge state conductance exhibited by CdTe/HgTe/CdTe heterostructure in the inverted regime (curves III and IV). Figure adapted from Refs. [7, 8].

its size and disorder. It was realized that this was a consequence of *topology*.

The last decade has seen the growth of a new field in condensed matter physics, based on the realization that such topological phases can be obtained without the application of an external magnetic field [3, 4, 5]. In these so-called topological insulators, the role of magnetic field is taken by the spin-orbit interaction. Like ordinary insulators, the topological insulators have a bulk energy gap separating the highest occupied energy band (valence band) and the lowest empty band (conduction band). But unlike ordinary insulators, the surface or edge of these materials have gapless metallic states, which are symmetry protected. In this sense, they are intimately related to the quantum Hall state. The class of topological insulators, which preserve time reversal symmetry have a $\mathbb{Z}_2$ classification. In particular, it is this class, which has caused a large excitement in the past few years, primarily because more than half a dozen materials have been experimentally confirmed to exhibit such a phase. Very recently, time reversal symmetry broken topological insulators (also termed Chern insulators since they have an integer classification based on the Chern number) have been experimentally realized, although at the extremely low temperatures of a few milliKelvin [6].

A time reversal invariant topological insulating phase was predicted theoretically by Bernevig, Hughes and Zhang (BHZ) in CdTe/HgTe/CdTe quantum wells [7]. Both CdTe and HgTe exist in zincblende-type lattice structure and for both the materials the relevant bands near Fermi level are at the Γ point in the Brillouin zone, as shown in Fig. 1.1(a). They are an s-type band (Γ_6), and a p-type band split by spin-orbit coupling into a $J = 3/2$ band (Γ_8) and a $J = 1/2$ band (Γ_7). CdTe has an ordering of bands similar to conventional semiconductors, for instance GaAs, where the s-type conduction band (Γ_6) is well separated from the p-type valence bands (Γ_8, Γ_7) by a large energy gap, of the order of 1 eV. However, in HgTe, the usual band order is reversed, because of the large spin-orbit coupling carried by the heavy element mercury. In this case, the Γ_8 band, which usually forms the valence band, is now higher in energy than the Γ_6 band. The light hole Γ_8 band forms the conduction band, while the heavy hole Γ_8 band forms the first valence band. The s-type band (Γ_6) is pushed down in energy and forms the second valence band. The degeneracy at the Γ point between the heavy and the light-hole bands makes HgTe a zero-gap semiconductor.

BHZ proposed that by growing CdTe/HgTe/CdTe heterostuctures it is possible to tune the above mentioned electronic structure and that there is a quantum phase transition as a function of the thickness d_{QW} of the quantum well. The heterostructure is a conventional insulator for $d_{QW} < d_c$ and a time reversal symmetric topological or quantum spin Hall (QSH) insulator for $d_{QW} > d_c$, where d_c is a critical thickness. This QSH insulator state, has a charge excitation bulk gap, but has topologically protected gapless *helical* edge states, that lie in the bulk gap. The term *helicity* refers to the perfect correlation between the spin and momentum of these edge states. Soon after the theoretical proposal, devices were fabricated and transport measurements were performed, showing the first signature of the QSH insulator [8]. In these experiments the electrical conductance due to the edge states was measured. An analysis using the Landauer-Büttiker scheme, yields a quantized conductance of e^2/h for each pair of edge states. Fig. 1.1(b) shows the resistance measurements for a number of samples as a function of gate voltage which allows the Fermi energy to be traversed across the bulk gap. Sample I has a narrow width and a large resistance in the gap. Samples III and IV, on the other hand are quantum wells having thickness greater than the critical thickness, d_c. These show a quantized conductance of $2e^2/h$ associated with the two edge states. Samples III and IV have the same length and different widths, while both show the same conductance, indicating that the transport is at the edge.

Apart from quantum well heterostructures, there have also been recent proposals for silicene and its germanium analog to host a quantum spin Hall phase, with spin-orbit-driven bandgaps of 2.9 meV and 23.9 meV, respectively [9]. Two-dimensional Sn films have also been predicted to have a spin-orbit gap of 300 meV, which is comparable to that of the three-dimensional topological insulators currently known [10]. These materials exhibit a low energy physics, which is well described by the Kane-Mele model, which will be discussed in detail in Chapter 2. In light of these promising developments, we will present our study of Andreev reflection in two-dimensional topological insulator-superconductor junctions in Chapter 4. In Chapter 5, we will also examine the possibility to manipulate impurity spins using the quantum spin Hall current.

Angle resolved photoemission spectroscopy (ARPES) has played an important role in the quest for finding new topological insulator materials. By illuminating a material with photons and measuring the energy-momentum

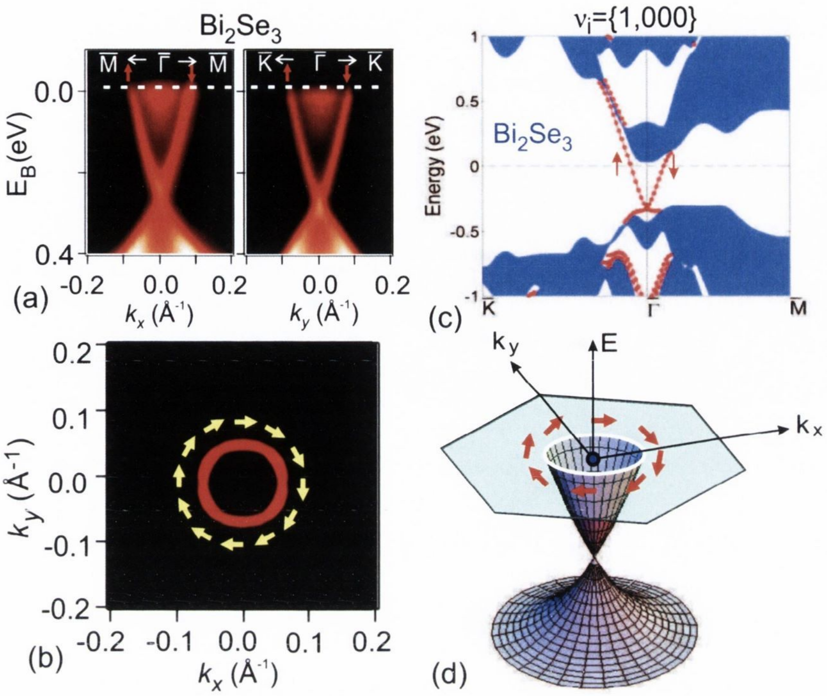

Figure 1.2: (a) Surface band structure for Bi_2Se_3 (111) from ARPES showing a single Dirac cone. (b) The fermi surface reveals the spin polarization of the bands (c) The band structure obtained from *ab-initio* calculations where the red dots indicate the surface states. (d) Schematic picture of the single spin-momentum locked Dirac cone on Bi_2Se_3 surface. The arrows indicate the direction of electron spin. Figure from Ref. [3].

distribution of the photoemitted electrons, one is able to extract the band structure of the material. Since this is a surface sensitive technique, it is particularly suited to study of protected states on surface of three-dimensional topological insulators. Furthermore, spin resolved ARPES makes it possible to determine the spin polarization of these states and measure their spin texture in the momentum space. In fact, Bi-Sb alloy was the first three-dimensional topological insulator to be discovered experimentally [11], by employing ARPES experiments, after an earlier theoretical prediction by Fu and Kane [12]. However, the alloy has a complicated band structure having five surface bands, with a tiny bulk band gap and since the material is not stoichiometric, it makes preparation of pure samples more difficult.

In 2009, concurrent theoretical [14] and experimental [15] works revealed a new material exhibiting non-trivial topological insulator phase, namely

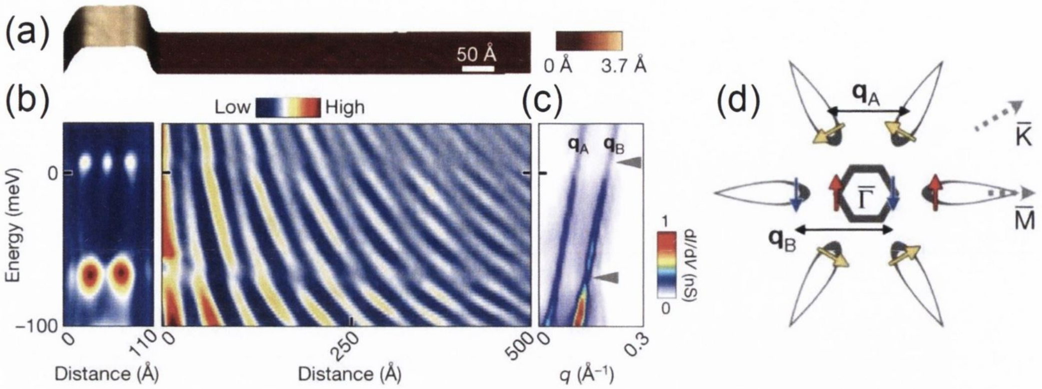

Figure 1.3: (a) Topographic image of a one bilayer terrace on Sb(111) surface. (b) Spatially resolved dI/dV plots in the terrace and adjacent flat region as a function of energy. (c) Fourier transform of the oscillations showing two prominent scattering vectors. (d) A schematic of the contour of surface states at Fermi energy with the arrows denoting the spin of the state. The allowed scattering wave vectors q_A and q_B are marked. Figure adapted from Ref. [17].

Bi_2Se_3. *Ab initio* calculations also predicted a similar phase in Bi_2Te_3 and Sb_2Te_3. The surface state of Bi_2Se_3 measured by ARPES and predicted by first-principles theoretical calculations is shown in Fig. 1.2. It has an ideal single Dirac cone and a relatively larger band gap of ~ 0.3 eV, making Bi_2Se_3 a prototypical topological insulator. The helical nature of surface states, which is an essential feature of topological insulators, has been shown using spin resolved ARPES, along with a Berry phase of π as one goes around the Dirac node. In Chapter 6, using this canonical topological insulator we will study the effect of barriers on the scattering properties of surface states. We will also demonstrate a single atom anisotropic magnetoresistance effect on the surface of Bi_2Se_3 (Chapter 7).

Scanning tunneling microscopy (STM) is another key experimental technique, which has enhanced the understanding of topological surface states and has also provided a direct visualization of signatures of these states when they interact with impurities and defects on the surface of the material. In STM measurements a sharp tip is positioned within quantum tunneling distance from a surface. The tunneling conductance (dI/dV) is directly proportional to the density of states (DOS) of the sample, which allows probing the energy distribution of these states with a high resolution over large spatial regions. Furthermore, Fourier transform of the DOS allows extracting information about the scattering processes. The helical nature of topological states, with opposite spin electrons moving in opposite directions, forbids exact backscattering as long as time reversal symmetry is preserved. This crucial property has been demonstrated for Bi-Sb alloy with a random distribution of defects by analyzing quasiparticle interference patterns imaged using the STM [16]. Another important property of symmetry-protected surface states is an enhanced transmission across strong surface disorder. This has also been shown in a topological semimetal Sb by using STM data to map onto a potential barrier model [17]. Transmission across a barrier, in the form of surface steps on the Sb(111) surface, was inferred by analysing the interference pattern of the surface states (Fig. 1.3). It was found that the surface states are likely to be transmitted even in the presence of strong surface disorder. Fourier transform of the DOS gave the allowed scattering vectors, which were consistent with prohibited spin-flip backscattering. In Chapter 6 we will study this system and its scattering properties using first-principles transport calculations and will compare our findings with the experiments reported in Reference [17].

1.1 Dissertation layout

Apart from the work presented in this thesis, other stand-alone investigations were also undertaken during the period of these studies. These include a theoretical anlaysis of multiple-probe quantum spin Hall bars, the inplementation of phenomenology of Andreev reflection in a first-principles transport code, and a study of giant magnetoresistance in spin-valves with prototypical two-dimensional layered material MoS_2 as a spacer. In an ongoing study, in collaboration with experimentalists, we are investigating the effect of organic molecular layers on topological surface states. The references to these works is provided in the list of publications in Appendix F.

Following a general introduction in this chapter, the layout for the rest of the thesis is as follows.

In Chapter 2 we discuss the basic notions of topology within the paradigm of band theory. A brief introduction to Berry phase, electric and time reversal polarization is provided. This sets the stage to define a $\mathbb{Z}_2$ invariant for time reversal symmetric topological insulators. We also introduce the Kane-Mele model, which is the prototypical model for two-dimensional topological insulators. Finally we discuss the extension to three dimensions.

In Chapter 3 we outline the two main methods used in this thesis: density functional theory, which provides a solution to the electronic structure many-body problem, and the Green's function method, which allows tackling quantum transport problems. A discussion of relativistic effects in solids, which are essential to correctly describe the electronic states in topological insulators, is provided.

Chapter 4 presents our results for Andreev reflection in two-dimensional topological insulators (with either conserved or broken time reversal symmetry) when they form an interface with a superconductor. We find a perfect Andreev reflection for both the cases, which is robust to disorder. For the time reversal symmetric case we show that implanting one of the edges with magnetic impurities suppresses one of the channels for Andreev reflection, while no such suppression is seen for symmetry broken situation.

In Chapter 5 we investigate spin-flip inelastic electron tunneling spectroscopy for magnetic adatoms deposited at the edge of two-dimensional topological insulators. We demonstrate that the magnetic impurity can be manipulated using the helical edge states. We also propose a four terminal device, which is designed to manipulate the spin of the adatom by all electrical means.

From model Hamiltonian investigations, we move on to material specific density functional theory based studies. Chapter 6 presents our first-principles transport calculations for scattering of topological surface states. Motivated by the experimental study of Ref. [17], we consider transmission across surface steps on Sb(111). We find a good agreement with scanning tunneling microscopy experiment, in particular for lifetimes of quantum well states and allowed scattering wave vectors. Large scale *ab initio* calculations on analogous steps on $Bi_2Se_3(111)$ surface reveal that backscattering is completely suppressed for normal incidence, while backscattering is allowed at all other incidence angles. We also construct a potential barrier model based on the often used Dirac Hamiltonian. A comparison with first-principles results reveals the shortcomings of such a model.

In Chapter 7 we demonstrate a single magnetic atom anisotropic magnetoresistance on topological insulator surfaces, arising from the interplay between helical spin-momentum-locked surface electronic structure and the hybridization of the magnetic adatom states. Our *ab initio* calculations for Mn adatom on Bi_2Se_3 elucidate the underlying mechanism and also reveal the real space spin texture around the magnetic impurity. We complement our findings with a two-dimensional model valid for both single adatoms and magnetic clusters, which leads to a proposed device setup for experimental realization.

Next, we turn our attention to Dirac semimetal systems in two as well as three-dimensional systems. In Chapter 8 we present our proposal to engineer a backscattering-free hybrid state in graphene by proximity with a three-dimensional topological insulator. This hybrid state at the interface has a Dirac-cone-like dispersion and a well-defined helical spin texture. Using transport calculations, we further confirm the robustness of this state to disorder. We investigate the interplay of bulk and surface Dirac states in the three-dimensional Dirac semimetal Na_3Bi. By employing density functional theory in conjunction with coherent potential approximation, we also reveal a topological phase transition in alloy $Na_3Bi_{1-x}Sb_x$.

Finally, in Chapter 9 we provide a summary of the work presented in this thesis, and we highlight some possible directions, which can be addressed in future investigations.

Chapter 2

Basic notions of topology in band theory

In this chapter we summarize the basic concepts of topology in the band theoretical picture. We begin with an introduction to band theory and the concept of Berry phase, potential and curvature. We then discuss the conductivity of an insulator using the Kubo formula and relate it to the Chern number and the quantized Hall response. The Su-Schrieffer-Heeger model, which provides an illustrative example of topological effects in a one-dimensional solid, is subsequently introduced. We then formulate the concept of electric polarization as a Berry phase and introduce the notion of a time reversal polarization. This is used to define a $\mathbb{Z}_2$ invariant for time reversal symmetric topological insulators. We then discuss the Kane-Mele model, which is a prototypical model for $\mathbb{Z}_2$ topological insulators in two dimensions and is one of the models used in this work. Finally we end with a generalization to three-dimensional topological insulators. This brief overview is based on the review by Hasan and Kane [3] and the books by Bernevig and Hughes [18] and by Shen [19].

2.1 Band theory

Consider a system of non-interacting electrons moving in the periodic potential produced by ions in a crystal. The Hamiltonian reads

$$H = \frac{\mathbf{p}^2}{2m} + V(\mathbf{r}), \tag{2.1}$$

where $V(\mathbf{r} + \mathbf{R}) = V(\mathbf{r})$ and $\mathbf{R}$ is a Bravais lattice vector. From Bloch's theorem it follows that the solution of the problem is given by

$$H|\psi_n(\mathbf{r}, \mathbf{k})\rangle = E_n(\mathbf{k})|\psi_n(\mathbf{r}, \mathbf{k})\rangle, \tag{2.2}$$

$$|\psi_n(\mathbf{r}, \mathbf{k})\rangle = e^{i\mathbf{k}.\mathbf{r}}|u_n(\mathbf{r}, \mathbf{k})\rangle, \tag{2.3}$$

where $|u_n(\mathbf{r}, \mathbf{k})\rangle$ is the Bloch state and $\mathbf{k}$ is the crystal momentum restricted to the first Brillouin zone (BZ). The subscript n denotes the band index. Translational symmetry yields

$$|u_n(\mathbf{r}, \mathbf{k})\rangle = |u_n(\mathbf{r} + \mathbf{R}, \mathbf{k})\rangle, \quad E_n(\mathbf{k}) = E_n(\mathbf{k} + \mathbf{G}). \tag{2.4}$$

Here $\mathbf{G}$ is the set of reciprocal lattice vectors such that $\mathbf{G} \cdot \mathbf{R} = 2m\pi$ ($m \in \mathbb{Z}$). Since $\mathbf{k}$ and $\mathbf{k} + \mathbf{G}$ are equivalent, the space of crystal momentum is a d-dimensional torus in a crystal extending in d spatial dimensions.

2.2 Berry phase, potential and curvature

Let us consider a system with a Hamiltonian which depends on a parameter $\mathbf{R}(t)$, which is a function of time. In the adiabatic approximation, where $\mathbf{R}(t)$ varies slowly in time compared to the smallest energy scale of the system, the instantaneous eigenvalues and eigenfunctions satisfy the Schrödinger equation

$$H(\mathbf{R}(t)) = |n(\mathbf{R}(t))\rangle = E_n(\mathbf{R}(t))|n(\mathbf{R}(t))\rangle, \tag{2.5}$$

From adiabaticity we have that the eigenstate $|n(\mathbf{R}(0))\rangle$ remains the instantaneous eigenstate of $H(\mathbf{R}(t))$ up to a phase θ, as $\mathbf{R}(t)$ is varied along some path $\mathcal{C}$.

$$|\psi(0)\rangle = |n(\mathbf{R}(0))\rangle, \quad |\psi(t)\rangle = e^{i\theta(t)}|n(\mathbf{R}(t))\rangle. \tag{2.6}$$

$$H(\mathbf{R}(t))|\psi(t)\rangle = i\hbar\frac{d}{dt}|\psi(t)\rangle. \tag{2.7}$$

Using the above two equations and the state normalization ($\langle n(\mathbf{R}(t))|n(\mathbf{R}(t))\rangle = 1$), we obtain

$$E_n(\mathbf{R}(t)) - i\hbar\langle n(\mathbf{R}(t))|\frac{d}{dt}|n(\mathbf{R}(t))\rangle = \hbar\frac{d\theta}{dt}, \tag{2.8}$$

which yields

$$\theta(t) = \frac{1}{\hbar}\int_0^t E_n(\mathbf{R}(t'))dt' - i\int_0^t \langle n(\mathbf{R}(t'))|\frac{d}{dt'}|n(\mathbf{R}(t'))\rangle dt'. \tag{2.9}$$

Here the first term is the usual dynamical phase arising from the Hamiltonian evolution, while the second term is called Berry phase [20],

$$\begin{aligned}\gamma_n &= i\int_0^t \langle n(\mathbf{R}(t'))|\frac{d}{dt'}|n(\mathbf{R}(t'))\rangle dt' \\ &= i\int_0^t \langle n(\mathbf{R})|\frac{d}{d\mathbf{R}}|n(\mathbf{R})\rangle d\mathbf{R}. \qquad (2.10)\end{aligned}$$

One can then define a vector potential or Berry connection as

$$\mathbf{A}_n(\mathbf{R}) = i\langle n(\mathbf{R})|\frac{d}{d\mathbf{R}}|n(\mathbf{R})\rangle, \qquad (2.11)$$

such that

$$\gamma_n = \int_{\mathcal{C}} \mathbf{A}_n(\mathbf{R})\cdot d\mathbf{R}. \qquad (2.12)$$

Under a gauge transformation

$$|n(\mathbf{R})\rangle \rightarrow e^{i\chi(\mathbf{R})}|n(\mathbf{R})\rangle, \quad \mathbf{A}_n(\mathbf{R}) \rightarrow \mathbf{A}_n(\mathbf{R}) - \frac{\partial\chi(\mathbf{R})}{\partial\mathbf{R}}. \qquad (2.13)$$

while the Berry phase transforms as

$$\gamma_n \rightarrow \gamma_n - \int_{\mathcal{C}} \frac{\partial\chi(\mathbf{R})}{\partial\mathbf{R}}\cdot d\mathbf{R} = \gamma_n + \chi(\mathbf{R}(0)) - \chi(\mathbf{R}(T)), \qquad (2.14)$$

where T is the time taken to traverse $\mathcal{C}$. Prior to Berry's work it was believed that with a suitable gauge choice the phase γ_n can be cancelled so that to be physically irrelevant. We consider closed paths $\mathcal{C}$, such that $\mathbf{R}(T) = \mathbf{R}(0)$. From the single-valuedness of the wavefunction

$$|n(\mathbf{R}(T))\rangle = |n(\mathbf{R}=0)\rangle. \qquad (2.15)$$

Any gauge transformation should preserve this single-valuedness

$$e^{i\chi(\mathbf{R}(T))}|n(\mathbf{R}(T))\rangle = e^{i\chi(\mathbf{R}(0))}|n(\mathbf{R}=0)\rangle. \tag{2.16}$$

The above two conditions imply that

$$\chi(\mathbf{R}(T)) - \chi(\mathbf{R}(0)) = 2m\pi, \quad m \in \mathbb{Z}. \tag{2.17}$$

The simple analysis above shows that for a closed path the Berry phase cannot be cancelled in general, unless it is a multiple of 2π. Furthermore, when $\mathcal{C}$ is a closed path the Berry phase is gauge-invariant, namely

$$\gamma_n = \oint_{\mathcal{C}} \mathbf{A}_n(\mathbf{R}) \cdot d\mathbf{R} = \int_S (\nabla_{\mathbf{R}} \times \mathbf{A}_n(\mathbf{R})) \cdot d\mathbf{s} = \int_S \mathcal{F}(\mathbf{R}) \cdot d\mathbf{s}, \tag{2.18}$$

where $\mathcal{F}(\mathbf{R}) = \nabla_{\mathbf{R}} \times \mathbf{A}_n(\mathbf{R})$ is the Berry curvature.

An alternative expression for the Berry phase, which is more convenient for numerical computation reads [18]

$$\gamma_n = -i \sum_{m \neq n} \int_S \frac{\langle n(\mathbf{R})|\frac{\partial H(\mathbf{R})}{\partial \mathbf{R}}|m(\mathbf{R})\rangle \times \langle m(\mathbf{R})|\frac{\partial H(\mathbf{R})}{\partial \mathbf{R}}|n(\mathbf{R})\rangle}{(E_m(\mathbf{R}) - E_n(\mathbf{R}))^2}. \tag{2.19}$$

The Chern number is defined as

$$C = \frac{1}{2\pi} \int_{\text{closed}} \mathcal{F}_n(\mathbf{R}) \cdot d\mathbf{s}. \tag{2.20}$$

This is always an integer for a closed surface, i.e. a surface that has no boundaries, for example the surface of a sphere or of a torus. A proof is provided in Appendix A. Note that the crucial point here is that the surface is closed, i.e. it has no boundaries.

The above concepts can be transferred to an electron in a crystal by identifying the crystal momentum $\mathbf{k}$ as the parameter $\mathbf{R}$. Analogously, it is possible to define a vector potential

$$\mathbf{A}_n(\mathbf{k}) = i\langle u_{n\mathbf{k}}|\frac{\partial}{\partial \mathbf{k}}|u_{n\mathbf{k}}\rangle, \tag{2.21}$$

which is the Berry connection in a periodic solid and the Berry curvature and phase read

$$\mathcal{F}_n(\mathbf{k}) = \nabla_{\mathbf{k}} \times \mathbf{A}_n(\mathbf{k}), \quad \gamma_n = \int_{BZ} \mathcal{F}_n(\mathbf{k}) \cdot d\mathbf{k}, \tag{2.22}$$

in a crystal.

2.2.1 Conductivity of an insulator

The Kubo formula for the linear response electrical conductivity of a two-dimensional sample reads

$$\sigma_{\alpha\beta} = \frac{ie^2\hbar}{A} \sum_{nm,n\neq m} \sum_{\mathbf{k}} \frac{\langle n\mathbf{k}|v_\alpha|m\mathbf{k}\rangle\langle m\mathbf{k}|v_\beta|n\mathbf{k}\rangle}{(E_{n\mathbf{k}} - E_{\mathbf{k}})^2}(f_{n\mathbf{k}} - f_{m\mathbf{k}}), \tag{2.23}$$

where A is the area of the sample, v_α is the velocity operator along direction α, $f_{n\mathbf{k}} = \frac{1}{e^{(E_{n\mathbf{k}}-E_F)/k_BT}+1}$ is the Fermi-Dirac function and $\alpha, \beta \in x, y$. The current density flowing in linear response to an electric field, E_β, is then expressed as

$$j_\alpha = \sum_\beta \sigma_{\alpha\beta} E_\beta. \tag{2.24}$$

If the energy gap of the insulating sample is much larger than the temperature scale, then the Kubo formula can be further simplified to yield

$$\sigma_{\alpha\beta} = -\frac{2e^2\hbar}{A} \sum_{\mathbf{k}} \sum_{n\in occ} \sum_{n\neq m} \frac{\mathrm{Im}(\langle n\mathbf{k}|v_\alpha|m\mathbf{k}\rangle\langle m\mathbf{k}|v_\beta|n\mathbf{k}\rangle)}{(E_{n\mathbf{k}} - E_{\mathbf{k}})^2}, \tag{2.25}$$

where the second summation is now over only the occupied bands. From the above expression it is clear that the longitudinal conductivity $\sigma_{xx} = 0$, since the quantity $\langle n\mathbf{k}|v_x|m\mathbf{k}\rangle\langle m\mathbf{k}|v_x|n\mathbf{k}\rangle = |\langle n\mathbf{k}|v_x|m\mathbf{k}\rangle|^2$ is real. Now the velocity operator is defined as

$$\hat{\mathbf{v}} = \frac{1}{\hbar}\frac{\partial H}{\partial \mathbf{k}}. \tag{2.26}$$

The Hall conductivity σ_{xy} is

$$\sigma_{xy} = \frac{e^2}{A\hbar} \sum_{\mathbf{k}} \sum_{n\in occ} \left(i \sum_{n\neq m} \frac{\langle n\mathbf{k}|\frac{\partial H}{\partial \mathbf{k}}|m\mathbf{k}\rangle \times \langle m\mathbf{k}|\frac{\partial H}{\partial \mathbf{k}}|n\mathbf{k}\rangle}{(E_{n\mathbf{k}} - E_{m\mathbf{k}})^2} \right). \tag{2.27}$$

By identifying the quantity in the parentheses as the Berry curvature and by replacing the summation over $\mathbf{k}$ points with an integral $\sum_{\mathbf{k}} \to A \int_{BZ} \frac{dk_x dk_y}{(2\pi)^2}$ we obtain

$$\sigma_{xy} = \frac{e^2}{h} \sum_{n\in occ} \left(\frac{1}{2\pi} \int_{BZ} \mathcal{F}_n \cdot d\mathbf{s} \right), \tag{2.28}$$

where the quantity in the parentheses is the Chern number and is guaranteed to be an integer for a closed surface, which in this particular case is the Brillouin zone. Thus, the Hall conductivity of an insulator is quantized to be an integer multiple of quantum of conductance $\frac{e^2}{h}$. This integer is the sum of the Chern numbers of all the occupied bands. For a quantum Hall insulator this corresponds to the number of filled Landau levels.

2.3 Topology in one-dimensional solid: Su-Schrieffer-Heeger model

Consider a one-dimensional chain of dimerized atoms described by the Hamiltonian [21]

$$H = \sum_i (t + \delta t) c^\dagger_{A,i} c_{B,i} + \sum_i (t - \delta t) c^\dagger_{A,i+1} c_{B,i} + h.c. \tag{2.29}$$

Here $c^\dagger_{A,i}(c_{A,i})$ creates (destroys) an electron at the site A of the i-th unit cell. The underlying physical reason for this dimerization (Peierls distortion) is a lowering of the electron kinetic energy at half-filling. The above Hamiltonian was proposed as a model for polyacetylene, and in general is applied, with modifications due to the details of the band filling, to augmented one-dimensional systems. Fourier transformation to the momentum space yields

$$H = \sum_k \sum_{\alpha\beta} c_{\alpha k} h_{\alpha\beta}(k) c_{\beta k}, \tag{2.30}$$

where $h(k) = \mathbf{d}(k) \cdot \boldsymbol{\sigma}$ with

$$d_x(k) = (t+\delta t)+(t-\delta t)\cos ka, \quad d_y(k) = (t-\delta t)\sin ka, \quad d_z(k) = 0, \tag{2.31}$$

and $\boldsymbol{\sigma} = \{\sigma_x, \sigma_y, \sigma_z\}$ is the triad of Pauli matrices. The eigenvalues are then

$$E_{\pm}(k) = \pm|\mathbf{d}| = \pm\sqrt{2(t^2+(\delta t)^2)+2(t^2-(\delta t)^2)\cos ka}, \tag{2.32}$$

where a is the lattice constant. The spectrum at half-filling is that of an insulator at finite δt, while for $\delta t = 0$ the system is a semi-metal. At the edge of the BZ, the low energy excitations are Dirac fermions and not usual Schrödinger fermions. By expanding around the edge of BZ, $k = \frac{\pi}{a} - q$ $(qa \ll 1)$

$$E_{\pm}\left(k = \frac{\pi}{a} - q\right) \approx \pm 2\sqrt{(tqa)^2 + (\delta t)^2}. \tag{2.33}$$

This is a linear dispersion of a Dirac fermion with velocity ta and mass δt. For $\delta t = 0$ we recover a massless Dirac fermion with linear gapless bands. The eigenstates of the full Hamiltonian are given by

$$|k+\rangle = \begin{pmatrix} \cos\theta/2 \\ e^{i\phi}\sin\theta/2 \end{pmatrix}, \quad |k-\rangle = \begin{pmatrix} -\sin\theta/2 \\ e^{i\phi}\cos\theta/2 \end{pmatrix}, \tag{2.34}$$

where $\theta = \cos^{-1}\frac{d_z}{|\mathbf{d}}$ and $\phi = \tan^{-1}\frac{d_y}{d_x}$. The Berry phase of the occupied band is [18, 19]

$$\gamma_- = \int_{-\pi/a}^{\pi/a} \langle k - |\frac{\partial}{\partial k}|k-\rangle dk = \int_S d\mathbf{s}\cdot\frac{1}{2}\frac{\mathbf{d}}{d^3} = \frac{1}{2}\Omega, \tag{2.35}$$

where S is the surface enclosed by the path $\mathcal{C}$ covered by vector $\mathbf{d}(\mathbf{k})$ as k goes from $-\frac{\pi}{a}$ to $\frac{\pi}{a}$. $\mathcal{C}$ is a closed loop since $\mathbf{d}(k = -\pi/a) = \mathbf{d}(k = \pi/a)$. Ω is the solid angle that the path $\mathcal{C}$ subtends at the origin $\mathbf{d} = 0$. Since $d_z = 0$, we only need to consider contours in the $d_x - d_y$ plane, as shown in Fig. 2.1. This gives us

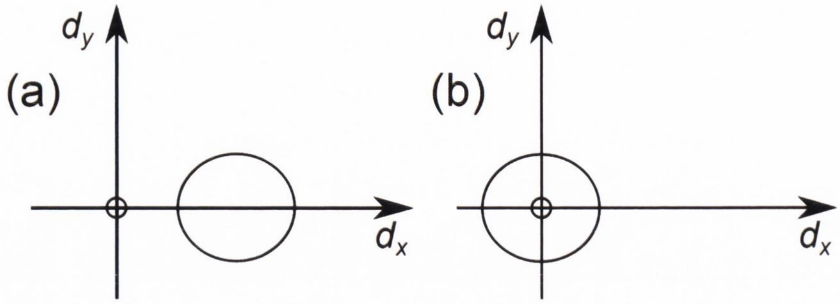

Figure 2.1: The contour in $\mathbf{d}$ space ($d_z = 0$) for the two cases (a) when it does not enclose the monopole at origin ($\delta t > 0$) and (b) when the monopole is within the contour ($\delta t < 0$).

$$\begin{aligned} \gamma_- &= 0, \quad \delta t > 0 \\ &= \pi, \quad \delta t < 0. \end{aligned} \tag{2.36}$$

At $\delta t = 0$ the system is gapless and serves as the point of a *topological phase transition*. The topological distinction between $\delta t < 0$ and $\delta t > 0$ is crucially hinged on $d_z = 0$. Consider

$$\{h(k), \sigma^z\} = d_x\{\sigma^x, \sigma^z\} + d_y\{\sigma^y, \sigma^z\} + d_z\{\sigma^z, \sigma^z\} = 2d_z = 0. \tag{2.37}$$

In the above expression we have used $\{\sigma^a, \sigma^b\} = 2\delta^{ab}$. The condition $\{h(k), \sigma^z\} = 0$, implies an associated symmetry called the *Chiral* symmetry. This is a recurring feature in topological band theory, where the existence of a symmetry leads to a classification based on a topological quantity.

From the low energy expansion around $k = \frac{\pi}{a}$ it follows that

$$d_x \approx 2\delta t = m, \quad d_y \approx atq = vq. \tag{2.38}$$

The low energy Hamiltonian then reads

$$h_{eff}(q) = m\sigma^x + vq\sigma^y. \tag{2.39}$$

Now consider a domain wall between regions of $\delta t > 0$ and $\delta t < 0$, i.e., between regions of opposite Dirac mass m. Since, we lose translational symmetry we make the replacement $q \rightarrow -i\frac{\partial}{\partial x}$. The zero energy solution satisfies

$$\begin{pmatrix} 0 & m - v\frac{\partial}{\partial x} \\ m + v\frac{\partial}{\partial x} & 0 \end{pmatrix} \begin{pmatrix} \psi_1 \\ \psi_2 \end{pmatrix} = 0, \tag{2.40}$$

which yields

$$(m - v\frac{\partial}{\partial x})\psi_2 = 0, \quad \psi_2 \sim e^{\frac{1}{v}\int_0^x m(x')dx'}. \tag{2.41}$$

$$(m + v\frac{\partial}{\partial x})\psi_1 = 0, \quad \psi_1 \sim e^{-\frac{1}{v}\int_0^x m(x')dx'}. \tag{2.42}$$

For $m(x \rightarrow -\infty) > 0$ and $m(x \rightarrow \infty) < 0$ the physical (non-diverging) solution is

$$\psi(x) = \begin{pmatrix} 0 \\ 1 \end{pmatrix} e^{\frac{1}{v}\int_0^x m(x')dx'}. \tag{2.43}$$

This localized zero-energy state at the domain wall is the Jackiw-Rebbi zero mode [22]. It is protected by chiral symmetry and is robust against deformations of the Hamiltonian. This is the zero-dimensional analog to the one-dimensional edge states and the two-dimensional surface states in topological insulators.

2.4 Electric and time reversal polarization

The electric polarization **P** is defined as the electric dipole moment per unit volume

$$\mathbf{P} = \frac{1}{V}\sum_i \mathbf{p}_i, \tag{2.44}$$

where the sum is carried out over all dipole moments $\mathbf{p}_i$ and V is the volume of the material. Note that **P** is an ambiguously defined quantity depending on the choice of unit cell (individual dipole). In the pioneering work by Vanderbilt and Resta it was shown that the electric polarization is related to the Berry phase [23, 24]

$$\mathbf{P} = \frac{e}{2\pi}\sum_{n\in occ}\int_{BZ} \mathbf{A}_n(\mathbf{k})\cdot d\mathbf{k}. \tag{2.45}$$

The ambiguity of **P** carries over in this formulation since the Berry phase is also defined only modulo 2π.

2.4.1 Time reversal symmetry and $\mathbb{Z}_2$ invariant

For a periodic system with time reversal symmetry (TRS)

$$H(-\mathbf{k}) = \Theta H(\mathbf{k})\Theta^{-1}, \tag{2.46}$$

where $\Theta = i\sigma_y\mathcal{K}$ is the time reversal operator and $\mathcal{K}$ performs complex conjugation. The points, Γ_i, in the Brillouin zone which satisfy

$$-\Gamma_i = \Gamma_i + n_i\mathbf{G}, \quad n_i \in \mathbb{Z}, \tag{2.47}$$

are called the time reversal invariant momenta (TRIM). At these points the

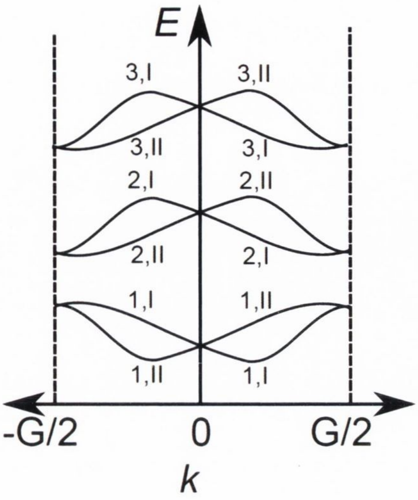

Figure 2.2: A schematic of generic band structure for a one-dimensional system with only time reversal symmetry.

Hamiltonian is always doubly degenerate due to Kramers' theorem,

$$H(\Gamma_i) = \Theta H(\Gamma_i)\Theta^{-1}. \tag{2.48}$$

For a one-dimensional system with TRS and no other symmetry (and hence no other degeneracy) the band structure is shown schematically in Fig. 2.2. Notice that all bands are non-degenerate except at the TRIM $k = 0, G/2$. It is possible to identify each of the Kramers pairs by labels I and II. These are degenerate at the TRIM ($k = 0, \pi$). Away from these TRIM we have $E_{n,\mathrm{I}}(k) = E_{n,\mathrm{II}}(-k)$, but not necessarily $E_{n,\mathrm{I}}(k) = E_{n,\mathrm{II}}(k)$. The Kramers pair eigenstates satisfy

$$|u_n^{\mathrm{I}}(-k)\rangle = -e^{i\chi_{kn}}\Theta|u_n^{\mathrm{II}}(k)\rangle, \quad n = 1, 2, ..., N. \tag{2.49}$$

Here $\chi_{k,n}$ is the $U(1)$ gauge freedom of the eigenstate.

$$\Theta|u_n^{\mathrm{I}}(-k)\rangle = -\Theta e^{i\chi_{kn}}\Theta|u_n^{\mathrm{II}}(k)\rangle = e^{-i\chi_{kn}}|u_n^{\mathrm{II}}(k)\rangle, \tag{2.50}$$

which gives

$$|u_n^{\mathrm{II}}(-k)\rangle = e^{i\chi_{-k,n}}\Theta|u_n^{\mathrm{I}}(k)\rangle. \tag{2.51}$$

Now we define a *partial polarization* following the Berry phase expression for the polarization [25]

$$P^s = \frac{1}{2\pi}\int_{BZ} A_k^s dk, \quad A_k^s = i\sum_{n\in occ}\langle u_n^s(k)|\frac{\partial}{\partial k}|u_n^s(k)\rangle, \quad s = \mathrm{I}, \mathrm{II}. \tag{2.52}$$

Here $A_k^s = i\sum_{n\in occ}\langle u_n^s(k)|\frac{\partial}{\partial k}|u_n^s(k)\rangle$. Using the anti-unitarity of Θ and the normalization of $|u_n^{\mathrm{II}}\rangle$ it can be shown that [25]

$$A_{-k}^{\mathrm{I}} = A_k^{\mathrm{II}} + \sum_{n\in occ}\frac{\partial\chi_{kn}}{\partial k}. \tag{2.53}$$

This yields for the partial polarization

$$\begin{aligned} P^{\mathrm{I}} &= \frac{1}{2\pi}\left(\int_0^\pi (A_k^{\mathrm{I}} + A_k^{\mathrm{II}})dk + \sum_{n\in occ}\int_0^\pi \frac{\partial\chi_{kn}}{\partial k}dk\right) \\ &= \frac{1}{2\pi}\left(\int_0^\pi A_k dk + \sum_{n\in occ}(\chi_{\pi n} - \chi_{0n})\right). \end{aligned} \tag{2.54}$$

Define a $U(2N)$ matrix at each k

$$w_{mn}(k) = \langle u_m(-k)|\Theta|u_n(k)\rangle. \tag{2.55}$$

This matrix is block-diagonal such that

$$w(k) = \mathrm{diag}(w_1(k), w_2(k), ..., w_N(k)), \quad w_\alpha(k) = \begin{pmatrix} 0 & -e^{i\chi_{k\alpha}} \\ e^{i\chi_{-k\alpha}} & 0 \end{pmatrix}. \tag{2.56}$$

The time reversal operator Θ connects only the Kramers partners and does not mix the labels $1, ..., N$. Now, at the TRIM w is an anti-symmetric matrix, i.e. $w^T = -w$. We use the Pfaffian of w (a discussion on Pfaffians and their properties follows in Appendix B)

$$\mathrm{Pf}[w(0)] = (-1)^N e^{-i\sum_n \chi_{0n}}, \quad \mathrm{Pf}[w(\pi)] = (-1)^N e^{-i\sum_n \chi_{\pi n}}. \tag{2.57}$$

This gives

$$e^{-i\sum_n \chi_{\pi n} - \chi_{0n}} = \frac{\mathrm{Pf}[w(\pi)]}{\mathrm{Pf}[w(0)]}, \tag{2.58}$$

$$\sum_n (\chi_{\pi n} - \chi_{0n}) = i \ln \left(\frac{\mathrm{Pf}[w(\pi)]}{\mathrm{Pf}[w(0)]} \right). \tag{2.59}$$

The above equations along with the expression for P^{I} yields

$$P^{\mathrm{I}} = \frac{1}{2\pi} \left[\int_0^{\pi} A_k dk + i \ln \left(\frac{\mathrm{Pf}[w(\pi)]}{\mathrm{Pf}[w(0)]} \right) \right], \tag{2.60}$$

and analogously

$$P^{\mathrm{II}} = \frac{1}{2\pi} \left[\int_{-\pi}^{0} A_k dk - i \ln \left(\frac{\mathrm{Pf}[w(\pi)]}{\mathrm{Pf}[w(0)]} \right) \right]. \tag{2.61}$$

Next we define a *time reversal polarization* P_θ

$$\begin{aligned} P_\theta &= P^{\mathrm{I}} - P^{\mathrm{II}} \\ &= \frac{1}{2\pi} \left[\int_0^{\pi} A_k dk - \int_{-\pi}^{0} A_k dk + 2i \ln \left(\frac{\mathrm{Pf}[w(\pi)]}{\mathrm{Pf}[w(0)]} \right) \right] \\ &= \frac{1}{2\pi i} \left[\int_0^{\pi} \mathrm{Tr}[w^\dagger \nabla_k w] - 2 \ln \left(\frac{\mathrm{Pf}[w(\pi)]}{\mathrm{Pf}[w(0)]} \right) \right]. \end{aligned} \tag{2.62}$$

In the last step above we have used the off-diagonal structure of w

$$\mathrm{Tr}[w^\dagger \nabla_k w] = \mathrm{Tr}\left[\begin{pmatrix} 0 & e^{-i\chi_{-kn}} \\ -e^{i\chi_{kn}} & 0 \end{pmatrix} \nabla_k \begin{pmatrix} 0 & -e^{-i\chi_{kn}} \\ e^{i\chi_{-kn}} & 0 \end{pmatrix}\right] = i(\nabla_k \chi_{-kn} - \nabla_k \chi_{kn}). \tag{2.63}$$

Using the identity $\mathrm{Tr}[\ln w] = \ln[\det(w)]$ the time reversal polarization can be rewritten as

$$\begin{aligned} P_\theta &= \frac{1}{2\pi i}\left(\ln\frac{\det[w(\pi)]}{\det[w(0)]} - 2\ln\frac{\mathrm{Pf}[w(\pi)]}{\mathrm{Pf}[w(0)]}\right) \\ &= \frac{1}{\pi i}\ln\left(\frac{\sqrt{\det[w(\pi)]}}{\mathrm{Pf}[w(\pi)]}\frac{\mathrm{Pf}[w(0)]}{\sqrt{\det[w(0)]}}\right). \end{aligned} \tag{2.64}$$

Since w is a unitary matrix ($w^\dagger w = 1$), $\mathrm{Pf}(w)$ and $\det(w)$ are unitary complex numbers

$$\det(w) = e^{i\alpha}, \quad \mathrm{Pf}(w) = e^{i\alpha/2}e^{in\pi}, \quad n \in \mathbb{Z}. \tag{2.65}$$

Using the above expressions

$$P_\theta = \frac{1}{\pi i}\ln[e^{-in\pi}e^{im\pi}] = m - n. \tag{2.66}$$

Hence P_θ is an integer. Moreover since the logarithm is defined only modulo $2\pi i$, the time reversal polarization is defined only modulo 2. This reveals P_θ to be a $\mathbb{Z}_2$ index. The above expression may be rewritten as

$$(-1)^{P_\theta} = \frac{\sqrt{\det[w(0)]}}{\mathrm{Pf}[w(0)]}\frac{\sqrt{\det[w(\pi)]}}{\mathrm{Pf}[w(\pi)]}. \tag{2.67}$$

Each of the factors in the above expression $\frac{\sqrt{\det[w(0)]}}{\mathrm{Pf}[w(0)]} = \pm 1$ and $\frac{\sqrt{\det[w(\pi)]}}{\mathrm{Pf}[w(\pi)]} =$

± 1. So, $P_\theta = 1$ if the term $\frac{\sqrt{\det[w]}}{\mathrm{Pf}[w]}$ changes sign between $k = 0$ and $k = \pi$. This indicates a topological phase, while $P_\theta = 0$ corresponds to a topologically trivial phase. In two dimensions we have

$$(-1)^\nu = \prod_{i=1}^{4} \delta_i, \quad \delta_i = \frac{\sqrt{\det[w(\Gamma_i)]}}{\mathrm{Pf}[w(\Gamma_i)]}, \tag{2.68}$$

where Γ_i represent the four TRIM $\{(0,0), (0,\pi/a), (\pi/a,0), (\pi/a,\pi/a)\}$ in two dimensions.

To summarize, the $\mathbb{Z}_2$ invariant ν for two-dimensional TRS obeying insulators is given by

$$(-1)^\nu = \prod_{i\in\mathrm{TRIM}} \delta_i, \quad \delta_i = \frac{\sqrt{\det[w(\Gamma_i)]}}{\mathrm{Pf}[w(\Gamma_i)]}, \qquad w_{mn} = \langle u_{-km}|\Theta|u_{kn}\rangle. \tag{2.69}$$

Here w is a $2N \times 2N$ unitary matrix and $2N$ is the number of occupied bulk bands. It appears as if the invariant depends only on the Bloch eigenstates at the TRIM, while in the derivation one needs to integrate over all momenta. However, to calculate the square root consistently one needs to choose a smooth gauge for $|u_{kn}\rangle$ over the entire BZ and hence the apparent simplification is lost in general. In the special case of insulators, which obey inversion symmetry, a simplified invariant can be constructed. Consider an inversion symmetric system with the Bloch Hamiltonian satisfying

$$h(\mathbf{k}) = \Pi h(-\mathbf{k})\Pi^{-1}, \tag{2.70}$$

where Π is the inversion operator, which is unitary ($\Pi\Pi^\dagger = 1$). Since a crystal comes back to itself on inverting twice we also have $\Pi^2 = 1$ and the eigenvalues of Π are ± 1. At a TRIM $h(\mathbf{k}) = h(-\mathbf{k})$ so $[h(\mathbf{k}), \Pi] = 0$ and as a consequence $h(\Gamma_i)$ and Π can be diagonalized simultaneously

$$\Pi |u_n(\Gamma_i)\rangle = \xi_n(\Gamma_i) |u_n(\Gamma_i)\rangle, \quad \xi_n = \pm 1. \tag{2.71}$$

Fu and Kane have shown that for insulators with both time reversal and inversion symmetries the topological invariant is given by [26]

$$(-1)^{\nu} = \prod_{i \in \mathrm{TRIM}} \delta_i, \quad \delta_i = \prod_{m=1}^{N} \xi_{2m}(\Gamma_i), \tag{2.72}$$

were $\xi_{2m}(\Gamma_i)$ is the parity eigenvalue of the $2m$-th occupied band at the TRIM Γ_i. So in presence of inversion symmetry the topological invariant can be determined by evaluating the parity eigenvalues at the TRIM for the occupied bulk bands. This is a great simplification and specially useful for first-principles approaches where the parity of the eigenvalues is easily accessible.

2.5 Kane-Mele model

A model for a two-dimensional time reversal invariant topological insulator was introduced by Kane and Mele [27, 28]. The Hamiltonian defined on a honeycomb lattice reads

$$H_{KM} = t \sum_{\langle ij \rangle} c_i^{\dagger} c_j + \lambda_v \sum_i \xi_i c_i^{\dagger} c_i + i\lambda_{SO} \sum_{\langle\langle ij \rangle\rangle} \nu_{ij} c_i^{\dagger} s^z c_j. \tag{2.73}$$

Here the operator $c_i^{\dagger}$ (c_i) creates (destroys) an electron at site i. The first term is a nearest neighbour hopping with strength t, the second term is a staggered sublattice potential such that $\xi_i = +1$ for A type sublattice and

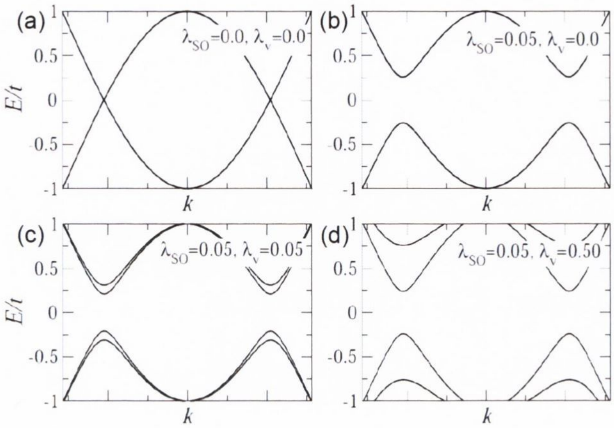

Figure 2.3: The bulk band structure of the Kane-Mele model for different values of λ_{SO} and λ_v showing different phases (a) pristine graphene, (b) topological insulator with inversion symmetry, (c) topological insulator with broken inversion symmetry, and (d) trivial insulator with broken inversion symmetry.

$\xi_i = -1$ for B sublattice, while the last term is a complex next-nearest neighbour hopping with strength λ_{SO}. The factor ν_{ij} is $+1$ if the hopping is counterclockwise, while it is -1 for clockwise hopping. Here $s^z = \pm 1$ corresponds to the electron spin. The third term in the Hamiltonian couples the spin and orbital motion of the electron, thereby mimicking a spin-orbit coupling. This Hamiltonian is gapped for non-zero λ_v and λ_{SO}. It represents a two-dimensional topological insulator (or quantum spin Hall state) for values of $\lambda_v < 3\sqrt{3}\lambda_{SO}$. Furthermore it can be shown that the state is preserved even in presence of terms in the Hamiltonian, which do not conserve the z component of the electron spin. The model has a non-trivial $\mathbb{Z}_2$ invariant, as a consequence of which its interface with an insulator of distinct topology should host topological states. We show the former by calculating the topological invariant directly, while the latter is shown by numerically diagonalizing the Hamiltonian in a ribbon geometry, i.e an interface with topologically trivial vacuum.

Now we turn to calculation of the $\mathbb{Z}_2$ invariant and for simplicity we

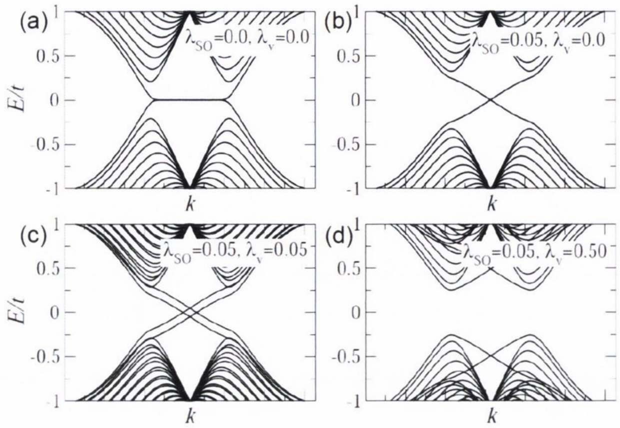

Figure 2.4: The band structure of the Kane-Mele model for 42 sites wide ribbon geometry for different values of λ_{SO} and λ_v illustrating (a) pristine graphene, (b) topological insulator with inversion symmetry, (c) topological insulator with broken inversion symmetry, and (d) trivial insulator with broken inversion symmetry.

consider a case, which does not break inversion symmetry so that one can use the parity criterion instead of the full Pfaffian construction. Consider a general unit cell with four degrees of freedom; two for sublattice (denoted by σ^z) and two for spin (denoted by s^z). The parity operator is given by

$$\Pi = \sigma^x \otimes I, \tag{2.74}$$

where I is the identity matrix for the spin indices since they do not change under inversion. The time reversal operator reads

$$\Theta = iI \otimes s^y \mathcal{K}, \tag{2.75}$$

where $\mathcal{K}$ is the complex conjugation operator and this time the identity matrix acts on the sublattice index. Any 4×4 matrix can be represented by using the identity I, five Dirac matrices Γ^a and their ten commutators $\Gamma^{ab} = [\Gamma^a, \Gamma^b]/2i$. One choice for the Dirac matrices (for them to be even under $\Pi\Theta$) is

$$\Gamma^{(1,2,3,4,5)} = (\sigma^x \otimes I, \sigma^y \otimes I, \sigma^z \otimes s^x, \sigma^z \otimes s^y, \sigma^z \otimes s^z). \tag{2.76}$$

Notice that $\Gamma^1 = \Pi$. This choice gives

$$\begin{aligned} \Theta\Gamma^a\Theta^{-1} = \Pi\Gamma^a\Pi^{-1} &= +\Gamma^a, \quad a = 1 \\ &= -\Gamma^a, \quad a \neq 1. \end{aligned} \tag{2.77}$$

In contrast the ten commutators are odd under combined time reversal and parity $(\Pi\Theta)\Gamma^{ab}(\Pi\Theta)^{-1} = -\Gamma^{ab}$. From time reversal and inversion symmetries $[H(\mathbf{k}), \Pi\Theta] = 0$, and the most general Hamiltonian can be written as

$$H(\mathbf{k}) = d_0(\mathbf{k})I + \sum_{a=1}^{5} d_a(\mathbf{k})\Gamma^a. \tag{2.78}$$

The energy eigenvalues are then

$$E(\mathbf{k}) = d_0(\mathbf{k}) \pm \sqrt{\sum_a d_a(\mathbf{k})^2}. \tag{2.79}$$

At the TRIM only Γ^1 is even under time reversal and parity and hence the other terms drop out and the parity eigenvalues for the states at the TRIM are eigenvalues of Π,

$$\delta_i = -\mathrm{sign}\left[d_1(\mathbf{k} = \Gamma_i)\right]. \tag{2.80}$$

For the Kane-Mele model we have

$$\begin{aligned} d_1 &= t(1+\cos x_1+\cos x_2), \\ d_2 &= t(\sin x_1+\sin x_2), \\ d_5 &= 2\lambda_{SO}[\sin x_1-\sin x_2-\sin(x_1-x_2)], \end{aligned} \tag{2.81}$$

while all the other d's are zero and $x_i = \mathbf{k}\cdot\mathbf{a}_i$. The TRIM occur at $x_i = \mathbf{k}\cdot\mathbf{a}_i = n_i\pi$ with $n_i = 0, 1$. This gives us

$$\delta_{i=(00)} = \delta_{i=(10)} = \delta_{i=(01)} = -1, \quad \delta_{i=(00)} = +1. \tag{2.82}$$

Using the above equation we obtain $\nu = 1$ and the fact that the model describes a quantum spin Hall insulator as long as the bulk energy gap remains finite. The role of the λ_{SO} term is to keep the energy gap finite over the entire BZ.

The bulk band structure for the Kane-Mele model is shown in Fig. 2.3. For $\lambda_{SO} = \lambda_v = 0$ (graphene), the system is a zero-gap semiconductor. Finite λ_{SO}, with vanishing λ_v opens an energy gap in the spectrum, with the bands being doubly degenerate owing to inversion symmetry. Introducing a finite λ_v breaks this degeneracy. We have diagonalized the Hamiltonian in a ribbon geometry with zigzag edges and the resulting eigenvalues are shown in Fig. 2.4. The two pair of edge states (one pair for each edge) now span the bulk band gap in Fig. 2.4(b) and (c). These metallic states are also spin polarized with opposite spins counter-propagating at a given edge. These are the so-called helical edge states. When $\lambda_v > 3\sqrt{3}\lambda_{SO}$, the edge states disappear and system reverts back to a trivial insulator phase [Fig. 2.4(d)].

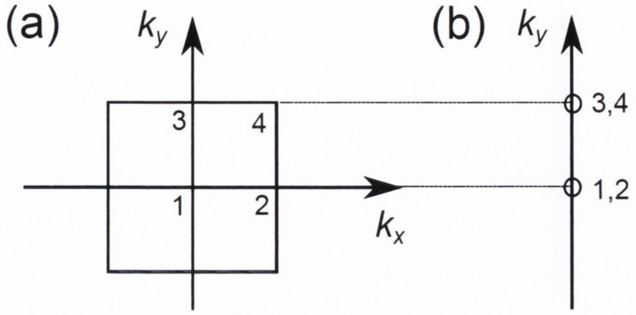

Figure 2.5: The bulk Brillouin zone for a two-dimensional system. The time reversal invariant momenta are marked. The right panel shows the projection to the edge Brillouin zone.

2.6 Generalization to three dimensions

Consider the projection of the bulk BZ of a two-dimensional topological insulator to its edge BZ. For the bulk we have

$$(-1)^{\nu} = \prod_{i=1}^{4} \delta_i. \tag{2.83}$$

The edge is along the y direction as shown in Fig. 2.5. If the product $\delta_1\delta_2$ and $\delta_3\delta_4$ have the same sign then the insulator is trivial and will have zero (or an even number) of edge states crossing the Fermi level. On the other hand, if $\delta_1\delta_2$ and $\delta_3\delta_4$ have opposite signs, then there would exist at least one (or in general an odd number) surface state crossing the Fermi energy, as long as it is in the bulk gap. The two situations are sketched schematically in Fig. 2.6.

Now one can generalize the same to a three-dimensional system. In this case there exist eight TRIM as shown in Fig. 2.7 for a BZ with cubic symmetry. Generically these can be represented by

$$\Gamma_i = \frac{1}{2}(n_1\mathbf{b}_1 + n_2\mathbf{b}_2 + n_3\mathbf{b}_3), \quad n_1, n_2, n_3 \in \mathbb{Z}. \tag{2.84}$$

Analogously to the two-dimensional situation, projections can be performed

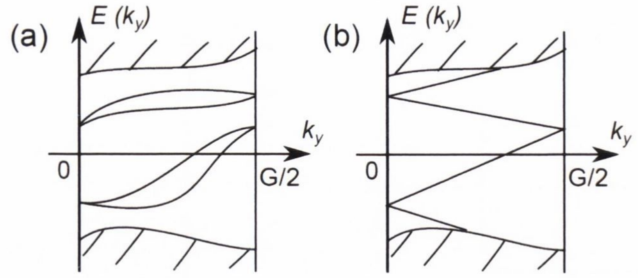

Figure 2.6: Schematic edge band structure for a two-dimensional (a) trivial and (b) topological insulator. The shaded regions represent the bulk bands. There exist an even number of edge bands crossing the Fermi level for the trivial case, while for a topological insulator an odd number of symmetry protected edge bands connect the bulk valence and conduction bands. The bands are necessarily degenerate at TRIM owing to Kramers theorem.

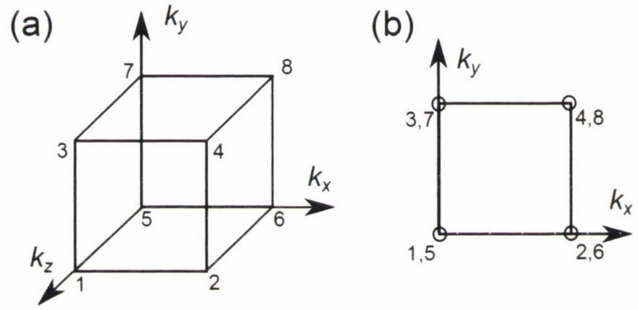

Figure 2.7: The bulk Brillouin zone for a three-dimensional cubic system. The eight time reversal invariant momenta are marked. The right panel shows the projection to one of the surface Brillouin zones.

onto different surfaces, which now contain four TRIM. One can then define four $\mathbb{Z}_2$ invariants as [29]

$$\begin{aligned}(-1)^{\nu_0} &= \prod_{n_1,n_2,n_3=0,1} \delta_{n_1n_2n_3}, \\ (-1)^{\nu_1} &= \prod_{n_2,n_3=0,1} \delta_{n_2n_3}, \\ (-1)^{\nu_2} &= \prod_{n_1,n_3=0,1} \delta_{n_1n_3}, \\ (-1)^{\nu_3} &= \prod_{n_1,n_2=0,1} \delta_{n_1n_2}. \end{aligned} \tag{2.85}$$

The first invariant ν_0 is the strong topological invariant, while the other three are invariants corresponding to a particular two-dimensional plane and are

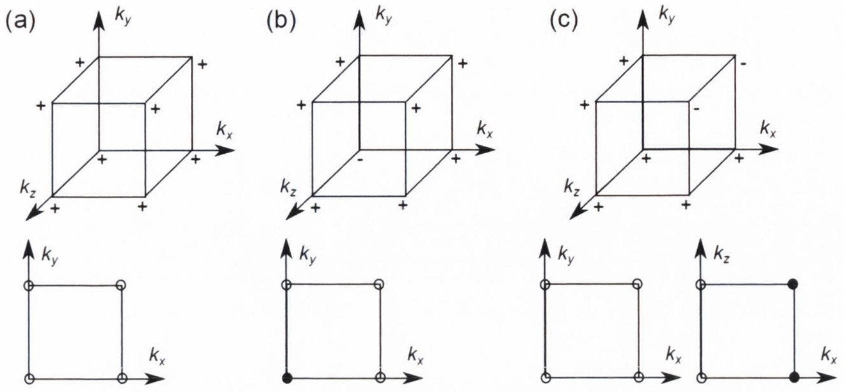

Figure 2.8: A comparison between (a) trivial insulator, (b) strong topological insulator, and (c) weak topological insulator. The panels below show the projection onto a two-dimensional surface Brillouin zone where the filled circles indicate a surface state that crosses the Fermi energy.

not true three-dimensional invariants. The quadruplet of $(\nu_0; \nu_1\nu_2\nu_3)$ completely describes the topological classification of a three-dimensional topological insulator. In contrast to the two-dimensional system, where there are only two classes of insulators, there exists a richer classification in three dimensions. Some examples are shown in Fig. 2.8. When $\nu_0 = 1$, the system is said to be a strong topological insulator. A slab made of such an insulator will host an odd number of metallic surface states. It is possible to have two of δ_i's to be -1, which renders the principal topological invariant ν_0 to be zero. However, such a system would display an even number of surface states only along certain planes and not along others as exemplified in Fig. 2.8(c). These are called weak topological insulators. The conventional (trivial) insulators have $\nu_0 = 0$ and the δ_i's at all TRIM have the same sign.

Chapter 3

Density functional theory and Green's functions for transport

In this chapter we briefly outline the two main methods used in this thesis, density functional theory for electronic structure and Green's functions method for quantum transport. In the section on density functional theory we begin by introducing the many body problem for a set of interacting electrons and ions, then we move on to the theorems of Hohenberg and Kohn. Next we discuss the Kohn-Sham formulation and different approximations to the exchange-correlation functional. The idea of pseudopotentials is then introduced and we discuss the Trullier-Martins norm-conserving scheme. Finally we end the section with a discussion of relativistic effects in solids and summarize the implementation of spin-orbit interaction in the SIESTA code.

In the section on Green's functions, we introduce definitions for the Green's functions and self-energies. We then summarize the expressions for current and transmission in the particular case of a two-terminal setup. The section on density functional theory is based on References [30, 31, 32]. The subsequent section on Green's function methods is based on References [34, 35].

3.1 Density functional theory

The Hamiltonian for a set of interacting electrons and ions is given by

$$H = -\frac{\hbar^2}{2m_e}\sum_i \nabla_i^2 - \frac{\hbar^2}{2M_I}\sum_I \nabla_I^2 + \frac{1}{2}\sum_{i\neq j}\frac{e^2}{|\mathbf{r}_i - \mathbf{r}_j|} - \sum_{i,I}\frac{Z_I e^2}{|\mathbf{r}_i - \mathbf{R}_I|} + \frac{1}{2}\sum_{I\neq J}\frac{Z_I Z_J e^2}{|\mathbf{R}_I - \mathbf{R}_J|}, \tag{3.1}$$

where m_e is the electron mass, M_I is mass of the I-th ion, Z_I is the charge of the I-th ion, e is the electron charge and $\hbar = h/2\pi$ is the reduced Planck's constant. Here $\mathbf{r}_i$ and $\mathbf{R}_J$ denote the position of i-th electron and J-th ion, respectively. Since, $M_I \gg m_e$ one may treat the ions as static and drop out the ionic kinetic energy. The Hamiltonian can be rewritten as

$$H = -\frac{\hbar^2}{2m_e}\sum_i \nabla_i^2 + \sum_i V_{\text{ext}}(\mathbf{r}_i) + \frac{1}{2}\sum_{i\neq j}\frac{e^2}{|\mathbf{r}_i - \mathbf{r}_j|} + E_{\text{ion}}, \tag{3.2}$$

where $V_{\text{ext}}(\mathbf{r}) = -\sum_{i,I}\frac{Z_I e^2}{|\mathbf{r}_i - \mathbf{R}_I|}$ is the *external* potential energy due to the ions and $E_{\text{ion}} = \frac{1}{2}\sum_{I\neq J}\frac{Z_I Z_J e^2}{|\mathbf{R}_I - \mathbf{R}_J|}$ is the potential energy due to the ion-ion interaction. The above Hamiltonian is still not solvable directly and one needs to resort to approximations. Density functional theory, in principle exact, provides the route to one such approximation to solve the many-body problem. It is based on the Hohenberg-Kohn theorems:

Theorem 1: The external potential $V_{\text{ext}}(\mathbf{r})$ is a unique functional of the ground state electron density $n(\mathbf{r})$.

Proof: Consider two potentials $V_{\text{ext}}^{(1)}(\mathbf{r})$ and $V_{\text{ext}}^{(2)}(\mathbf{r})$, which differ by more than a constant and give the same ground state density $n(\mathbf{r})$. Since they belong to distinct Hamiltonians $H_{\text{ext}}^{(1)}$ and $H_{\text{ext}}^{(2)}$, they yield different ground state wavefunctions $\psi^{(1)}$ and $\psi^{(2)}$, respectively. From the variational principle we have

$$E^{(1)} = \langle \psi^{(1)} | H_{\text{ext}}^{(1)} | \psi^{(1)} \rangle < \langle \psi^{(2)} | H_{\text{ext}}^{(1)} | \psi^{(2)} \rangle. \tag{3.3}$$

We have assumed that there is no ground state degeneracy, which means that the inequality strictly holds.

$$\langle \psi^{(2)} | H_{\text{ext}}^{(1)} | \psi^{(2)} \rangle = \langle \psi^{(2)} | H_{\text{ext}}^{(2)} | \psi^{(2)} \rangle + \langle \psi^{(2)} | V_{\text{ext}}^{(1)} - V_{\text{ext}}^{(2)} | \psi^{(2)} \rangle, \tag{3.4}$$

which gives,

$$E^{(1)} < E^{(2)} + \langle \psi^{(2)} | V_{\text{ext}}^{(1)} - V_{\text{ext}}^{(2)} | \psi^{(2)} \rangle. \tag{3.5}$$

Since the ground state densities for the two potentials are the same, the above can be rewritten as

$$E^{(1)} < E^{(2)} + \int [V_{\text{ext}}^{(1)}(\mathbf{r}) - V_{\text{ext}}^{(2)}(\mathbf{r})] n(\mathbf{r}) d\mathbf{r}. \tag{3.6}$$

If we had started with the variational principle for $\psi^{(2)}$ instead of $\psi^{(1)}$, we would have obtained

$$E^{(2)} < E^{(1)} + \int [V_{\text{ext}}^{(2)}(\mathbf{r}) - V_{\text{ext}}^{(1)}(\mathbf{r})] n(\mathbf{r}) d\mathbf{r}. \tag{3.7}$$

From the two inequalities we arrive at a contradiction, $E^{(1)} + E^{(2)} < E^{(1)} + E^{(2)}$. Thus, our assumption that two external potentials can give the same ground state density was wrong.

Theorem 2: A universal energy functional of the electron density, $E[n(\mathbf{r})]$, exists. The density that minimizes this functional is the exact ground state density.

Proof: Define a functional $F[n(\mathbf{r})]$ as the expectation value of the kinetic energy and electron-electron interaction energy for a wavefunction $\psi[n]$

$$F[n] = -\frac{\hbar^2}{2m_e}\sum_i \langle \psi[n]|\nabla_i^2|\psi[n]\rangle + \frac{e^2}{2}\sum_{i\neq j}\langle \psi[n]|\frac{1}{|\mathbf{r}_i - \mathbf{r}_j|}|\psi[n]\rangle. \tag{3.8}$$

The ground state energy is

$$E[n] = F[n] + \int V_{\text{ext}}(\mathbf{r})n(\mathbf{r})d\mathbf{r} + E_{\text{ion}}. \tag{3.9}$$

This functional is minimized by the exact ground state density, as can be seen from the variational principle.

Since such a universal functional, $F[n]$, is unknown Kohn and Sham reformulated the variational problem in a form suitable to construct approximations. Consider an auxilliary non-interacting system with the Hamiltonian

$$H_{\text{aux}} = -\frac{\hbar^2}{2m_e}\nabla^2 + V_{KS}(\mathbf{r}). \tag{3.10}$$

The single-particle solutions of the Hamiltonian satisfy a Schrödinger-like equation

$$\left[-\frac{\hbar^2}{2m_e}\nabla^2 + V_{KS}(\mathbf{r})\right]\phi_i(\mathbf{r}) = \epsilon_i\phi_i(\mathbf{r}), \tag{3.11}$$

where $\phi_i(\mathbf{r})$ are the single-particle eigenstates. Then the ground state electron density is given by

$$n(\mathbf{r}) = \sum_i |\phi_i(\mathbf{r})|^2. \tag{3.12}$$

The exact ground state density can be expressed in terms of the solutions of an auxilliary non-interacting problem. This is the crucial idea of the Kohn-Sham formulation. This reformulation allows constructing approximations to the universal functional $F[n]$. One can then minimize the energy functional in terms of ϕ_i's.

For the auxilliary system, define

$$T_{KS}[n] = -\frac{\hbar^2}{2m_e}\sum_i \langle\phi_i[n]|\nabla^2|\phi_i[n]\rangle, \quad E_H[n] = \frac{e^2}{2}\int \frac{n(\mathbf{r})n(\mathbf{r}')}{|\mathbf{r}-\mathbf{r}'|}d\mathbf{r}d\mathbf{r}', \tag{3.13}$$

where T_{KS} and E_H are the kinetic and Hartree energies of the Kohn-Sham auxilliary system, respectively. Now the universal energy functional may be rewritten as

$$\begin{aligned} E[n] &= (T_{KS}[n] - T_{KS}[n] + E_H[n] - E_H[n]) + F[n] + \int V_{\text{ext}}(\mathbf{r})n(\mathbf{r})d\mathbf{r} + E_{\text{ion}} \\ &= T_{KS}[n] + E_H[n] + \int V_{\text{ext}}(\mathbf{r})n(\mathbf{r})d\mathbf{r} + E_{\text{ion}} + E_{xc}[n], \qquad (3.14) \end{aligned}$$

where $E_{xc}[n]$ is the exchange-correlation functional. It is defined as the difference between the sum of expectation values of the kinetic and Hartree energies of the actual interacting system and the auxilliary non-interacting system,

$$E_{xc}[n] = F[n] - T_{KS}[n] - E_H[n]. \tag{3.15}$$

Approximate expressions for the functional $E_{xc}[n]$ are easier to find as compared to approximate forms for $F[n]$. The density may be expressed in terms of the orbitals and the minimization may be performed over them, by imposing

$$\frac{\delta E}{\delta \phi_i(\mathbf{r})} = 0, \tag{3.16}$$

along with the constraint $\langle \phi_i | \phi_j \rangle = \delta_{ij}$. This yields the expression for the Kohn-Sham potential,

$$V_{KS}(\mathbf{r}) = V_{\text{ext}}(\mathbf{r}) + V_H(\mathbf{r}) + V_{xc}(\mathbf{r}), \tag{3.17}$$

where

$$V_H(\mathbf{r}) = e^2 \int \frac{n(\mathbf{r}')}{|\mathbf{r} - \mathbf{r}'|} d\mathbf{r}', \quad V_{xc}(\mathbf{r}) = \frac{\delta E_{xc}}{\delta n(\mathbf{r})}. \tag{3.18}$$

Thus, in the Kohn-Sham reformulation one needs to find the N lowest energy solutions of the Kohn-Sham equation,

$$H_{KS}\phi_i(\mathbf{r}) = \left[-\frac{\hbar^2}{2m_e}\nabla^2 + V_{\text{ext}}(\mathbf{r}) + e^2 \int \frac{n(\mathbf{r}')}{|\mathbf{r} - \mathbf{r}'|} d\mathbf{r}' + V_{xc}(\mathbf{r}) \right] \phi_i(\mathbf{r}) = \epsilon_i \phi_i(\mathbf{r}). \tag{3.19}$$

The corresponding density is the exact ground state density of the original many-body problem and $E[n]$ is its exact ground state energy.

The caveat of DFT is that the exchange-correlation functional is unknown. So, in practice, one needs to make approximations to V_{xc}. Also, one needs to be careful as the Kohn-Sham eigenvalues and eigenvectors are not the real energy and wavefunctions of the physical system. In practice, however, they are routinely interpreted as a first approximation to the energy and eigenstates of the system. In this work we take this "liberal" point of view.

The earliest and still one of the most widely used approximation to the exchange correlation functional is the so-called local density approximation (LDA). One assumes that,

$$E_{xc}[n] = \int n(\mathbf{r})\epsilon_{xc}^{\text{hom}}[n(\mathbf{r})]d\mathbf{r}, \tag{3.20}$$

where $\epsilon_{xc}^{\text{hom}}$ is the exchange-correlation energy density of homogeneous electron gas. The expression for exchange energy for the homogeneous electron gas is known analytically, while various parameterizations for the correlation term have been tabulated based on accurate Monte-Carlo computations [33].

The Kohn-Sham reformulation can also be performed in terms of densities of up and down spin electrons, $n_\uparrow(\mathbf{r})$ and $n_\downarrow(\mathbf{r})$. The Kohn-Sham equation can then be written down for both spins

$$\left[-\frac{\hbar^2}{2m_e}\nabla^2 + V_{\text{ext}}(\mathbf{r}) + e^2\int \frac{n(\mathbf{r}')}{|\mathbf{r}-\mathbf{r}'|}d\mathbf{r}' + V_{xc}^{\sigma}(\mathbf{r})\right]\phi_{i\sigma}(\mathbf{r}) = \epsilon_{i\sigma}\phi_{i\sigma}(\mathbf{r}), \tag{3.21}$$

where $\sigma = (\uparrow, \downarrow)$ is the spin index and the exchange-correlation potential, $V_{xc}^{\sigma}(\mathbf{r}) = \frac{\delta E}{\delta n^{\sigma}(\mathbf{r})}$, becomes spin dependent. Similar to the LDA one can make a local spin density approximation (LSDA) to the exchange-correlation functional

$$E_{xc}[n_\uparrow, n_\downarrow] = \int n(\mathbf{r})\epsilon_{xc}^{\text{hom}}[n_\uparrow(\mathbf{r}), n_\downarrow(\mathbf{r})]d\mathbf{r}, \tag{3.22}$$

where $\epsilon_{xc}^{\text{hom}}[n_\uparrow(\mathbf{r}), n_\downarrow(\mathbf{r})]$ is the energy density of the uniform electron gas with constant spin up and down densities. Instead of $n_\uparrow$ and $n_\downarrow$, one may also formulate the Kohn-Sham equations in terms of electron density, $n(\mathbf{r}) = n_\uparrow(\mathbf{r})+n_\downarrow(\mathbf{r})$, and spin magnetization, $m(\mathbf{r}) = \mu_e[n_\uparrow(\mathbf{r})-n_\downarrow(\mathbf{r})]$. Here μ_e is the magnetic moment of electron (Bohr magneton). One can define an average exchange-correlation potential $\bar{V}_{xc}(\mathbf{r}) = \frac{\delta E_{xc}}{\delta n(\mathbf{r})}$ and a local effective magnetic field $B_{xc}(\mathbf{r}) = -\frac{\delta E_{xc}}{\delta m(\mathbf{r})}$. The Kohn-Sham equations can then be rewritten as

$$\begin{gathered}\left[-\frac{\hbar^2}{2m_e}\nabla^2 + V_{\text{ext}}(\mathbf{r}) + e^2\int\frac{n(\mathbf{r}')}{|\mathbf{r}-\mathbf{r}'|}d\mathbf{r}' + \bar{V}_{xc}^{\sigma}(\mathbf{r}) - \mu_e B_{xc}(\mathbf{r})\right]\phi_{i\uparrow}(\mathbf{r}) = \epsilon_{i\uparrow}\phi_{i\uparrow}(\mathbf{r}),\\ \left[-\frac{\hbar^2}{2m_e}\nabla^2 + V_{\text{ext}}(\mathbf{r}) + e^2\int\frac{n(\mathbf{r}')}{|\mathbf{r}-\mathbf{r}'|}d\mathbf{r}' + \bar{V}_{xc}^{\sigma}(\mathbf{r}) + \mu_e B_{xc}(\mathbf{r})\right]\phi_{i\downarrow}(\mathbf{r}) = \epsilon_{i\downarrow}\phi_{i\downarrow}(\mathbf{r})\end{gathered} \tag{3.23}$$

It is also possible to generalize the Kohn-Sham formulation to the case of non-collinear spins. One then works with the full spin density matrix, $n_{\sigma\sigma'}(\mathbf{r})$ and the Kohn-Sham equation reads

$$\left[\left\{-\frac{\hbar^2}{2m_e}\nabla^2 + V_{\text{ext}}(\mathbf{r}) + e^2\int\frac{n(\mathbf{r}')}{|\mathbf{r}-\mathbf{r}'|}d\mathbf{r}'\right\}\delta_{\sigma\sigma'} + V_{xc}^{\sigma\sigma'}(\mathbf{r})\right]\phi_{i\sigma'}(\mathbf{r}) = \epsilon_{i\sigma}\phi_{i\sigma}(\mathbf{r}). \tag{3.24}$$

In the above equation, the exchange-correlation functional, $V_{xc}^{\sigma\sigma'}(\mathbf{r}) = \frac{\delta E_{xc}}{\delta n^{\sigma\sigma'}(\mathbf{r})}$, in general has non-zero off-diagonal terms. This is usually obtained by diagonalizing the spin density matrix at each point $\mathbf{r}$ and then one uses the $\epsilon_{xc}^{\text{hom}}[n_\uparrow(\mathbf{r}), n_\downarrow(\mathbf{r})]$ energy density as in the collinear case. As for the collinear problem, the non-collinear case can be reformulated in terms of

$$n(\mathbf{r}) = \text{Tr}[n^{\sigma\sigma'}(\mathbf{r})], \quad \mathbf{m}(\mathbf{r}) = \mu_e\sum_{\sigma_1\sigma_2}\boldsymbol{\sigma}_{\sigma_1\sigma_2}n^{\sigma_1\sigma_2}(\mathbf{r}), \tag{3.25}$$

where $\boldsymbol{\sigma} = (\sigma_x, \sigma_y, \sigma_z)$ is the triad of Pauli matrices. The Kohn-Sham equation now takes the form

$$\left[\left\{\frac{\hbar^2}{2m_e}\nabla^2+V_{\text{ext}}(\mathbf{r})+e^2\int\frac{n(\mathbf{r}')}{|\mathbf{r}-\mathbf{r}'|}d\mathbf{r}'+\bar{V}_{xc}(\mathbf{r})\right\}\delta_{\sigma\sigma'}-\mu_e\mathbf{B}_{xc}(\mathbf{r})\boldsymbol{\sigma}_{\sigma\sigma'}\right]\phi_{i\sigma'}(\mathbf{r})=\epsilon_{i\sigma}\phi_{i\sigma}(\mathbf{r}), \tag{3.26}$$

where $\bar{V}_{xc}(\mathbf{r})=\frac{\delta E_{xc}}{\delta n(\mathbf{r})}$ and $\mathbf{B}_{xc}(\mathbf{r})=-\frac{\delta E_{xc}}{\delta \mathbf{m}(\mathbf{r})}$.

Another frequently used approximation to the exchange-correlation energy is the generalized gradient approximation (GGA), in which, as the name suggests, the exchange-correlation energy depends on the gradient of the density $\epsilon_{xc}^{\text{hom}}[n(\mathbf{r}),\nabla n(\mathbf{r})]$. In most of the problems studied in this work, we employ either the LDA or the GGA for the exchange-correlation energy.

3.1.1 Pseudopotentials

The electronic states of an atom can be divided into core and valence states. The core states refer to the fully occupied inner shells. The valence states are the outer shells, which take part in the chemical bonding. Since the properties of the core states are not affected much by the chemical environment, it is possible to consider only the valence electrons in the calculation. Core states and the nucleus are replaced by a pseudopotential, V^{PS}, which avoids the singularity at the nucleus but reproduces the real potential at sufficiently far distances. This greatly reduces the computational cost of a typical calculation.

Consider an isolated atom with spherical symmetry. The radial part of the Schrödinger equation for a spherically symmetric potential $V(r)$, in atomic units ($m_e=e=\hbar=4\pi\epsilon_0=1$), reads

$$\left[-\frac{1}{2}\frac{d^2}{dr^2}+\frac{l(l+1)}{2r^2}+V(r)\right]\phi_l(r)=\epsilon\phi_l(r), \tag{3.27}$$

where $\phi_l(r)$ is the radial part of the full wavefunction $\psi(\mathbf{r}) = (1/r)\phi_l(r)Y_{lm}(\theta,\phi)$ and Y_{lm} are the spherical harmonics. One of the possible pseudopotentials choice is given by the Trullier-Martins norm-conserving scheme. In this scheme the pseudopotentials are chosen to satisfy the following conditions:

1. For a given atomic configuration the valence eigenvalues of the real (all-electron) potential and pseudopotential are the same.
2. Beyond a core radius, r_c, the valence eigenstates of the real potential and pseudopotential are equal.
3. Inside the core radius, the total charges of both the all-electron and pseudopotential eigenstates are equal.
4. The logarithmic derivative and the energy derivative of the logarithmic derivative of the real and pseudopotential eigenstates are same for $r > r_c$.

The first condition ensures that the real potential and the pseudopotential give the same eigenenergies, for a given atomic configuration. The second condition ensures that the all-electron and pseudopotential eigenfunctions match beyond the core region. The third condition ensures that the electrostatic potential of the real and pseudo wavefunction are identical. The fourth condition ensures that the scattering from the real potential and pseudopotential matches not only at the eigenenergies, but also at energies nearby the eigenvalues. The procedure to construct the pseudopotential is as follows. One solves the Kohn-Sham equation for the potential of one ion. The Kohn-equation for each l-component $\phi_l(r)$ reads

$$\left[-\frac{1}{2}\frac{d^2}{dr^2}+\frac{l(l+1)}{2r^2}-\frac{Ze}{r}+V_H(\mathbf{r})+V_{xc}(r)\right]\phi_l(r)=\epsilon_l\phi_l(r). \tag{3.28}$$

One then divides the set ϕ_l into core and valence wavefunctions. The next step is to construct an operator V^{PS}, such that the pseudo wavefunctions ϕ_l^{PS}, apart from satisfying the above criteria, also satisfy

$$\left[-\frac{1}{2}\frac{d^2}{dr^2}+\frac{l(l+1)}{2r^2}+V^{PS}+V_H^{PS}(\mathbf{r})+V_{xc}^{PS}(r)\right]\phi_l^{PS}(r)=\epsilon_l\phi_l^{PS}(r), \tag{3.29}$$

where V_H^{PS} and V_{xc}^{PS} are usual Hartree and exchange-correlation potentials, but evaluated at the pseudo wavefunction density. The form of the pseudopotential operator reads

$$V^{PS}=V_{\text{local}}(r)+\sum_{lm}B_l|\chi_{lm}\rangle\langle\chi_{lm}|. \tag{3.30}$$

One of the ways to choose coefficients B_l and states χ_{lm} is to construct the solutions $\phi_l^{PS}(r)$ and $V_{\text{local}}(r)$, which satisfy the above mentioned four properties. Then, one can obtain χ_{lm} from

$$\chi_{lm}(\mathbf{r})=\left[\epsilon_l-\left\{-\frac{1}{2}\nabla^2+V_{\text{local}}(r)+V_H^{PS}(r)+V_{xc}^{PS}(r)\right\}\right]\psi_{lm}^{PS}(\mathbf{r}), \tag{3.31}$$

and

$$B_l=\frac{1}{\langle\chi_{lm}|\psi_{lm}^{PS}\rangle}. \tag{3.32}$$

3.1.2 Relativistic effects in solids

Spin-orbit interaction is a relativistic effect, which becomes particularly important for elements with a large atomic number. In particular, it is essential to include spin-orbit effects to correctly describe electronic states in topological insulators, which are the focus of this thesis. In this subsection, we begin with a derivation of the Pauli equation from the Dirac equation. All-electron Dirac or Pauli equation for a single atom serves as the starting point for relativistic pseudopotential generation. Using this we derive the expression for the corrections to the Schrödinger equation, which make various relativistic contributions transparent. Finally we outline the scheme used in the SIESTA code for including spin-orbit terms.

Dirac to Pauli equation

We begin with the Dirac equation in the presence of an external electromagnetic field [36],

$$i\hbar\frac{\partial}{\partial t}\Psi = \left[c\boldsymbol{\alpha}\cdot(\mathbf{p}+e\mathbf{A}) + \beta mc^2 - e\Phi\right]\Psi. \tag{3.33}$$

Here $\mathbf{A}$ and Φ are the vector and scalar potentials, respectively, while $\boldsymbol{\alpha}$ and β are 4×4 matrices, which satisfy the following commutation relations,

$$\alpha_i\alpha_j + \alpha_j\alpha_i = 2\delta_{ij}, \tag{3.34}$$

$$\alpha_i\beta + \beta\alpha_i = 0. \tag{3.35}$$

Furthermore, $\alpha_i^2 = \beta^2 = I_{4\times 4}$. Next, we can write the wavefunction as

$$\Psi = \begin{pmatrix} \phi \\ \chi \end{pmatrix}, \tag{3.36}$$

where ϕ and χ are two-component spinors. The Dirac equation can then be rewritten as a set of two equations,

$$\left(i\hbar \frac{\partial}{\partial t} + e\Phi \right) \phi = c\boldsymbol{\sigma} \cdot (\mathbf{p} + e\mathbf{A})\chi, \tag{3.37}$$

$$\left(i\hbar \frac{\partial}{\partial t} + e\Phi + 2mc^2 \right) \chi = c\boldsymbol{\sigma} \cdot (\mathbf{p} + e\mathbf{A})\phi. \tag{3.38}$$

Here we have used the representation, $\boldsymbol{\alpha} = \begin{pmatrix} 0 & \boldsymbol{\sigma} \\ \boldsymbol{\sigma} & 0 \end{pmatrix}$ and $\boldsymbol{\beta} = \begin{pmatrix} I_{2\times 2} & 0 \\ 0 & -I_{2\times 2} \end{pmatrix}$. In the non-relativistic limit the term $2mc^2$ is much larger than the other two terms. If we retain only such a term then we obtain,

$$\chi \approx \frac{1}{2mc} \boldsymbol{\sigma} \cdot (\mathbf{p} + e\mathbf{A})\phi. \tag{3.39}$$

Substituting this back into the other equation yields,

$$\left(i\hbar \frac{\partial}{\partial t} + e\Psi \right) \phi = \frac{1}{2m} [\boldsymbol{\sigma} \cdot (\mathbf{p} + e\mathbf{A})]^2 \phi. \tag{3.40}$$

Now, if we use the identity,

$$(\boldsymbol{\sigma} \cdot \mathbf{a})(\boldsymbol{\sigma} \cdot \mathbf{b}) = \mathbf{a} \cdot \mathbf{b} + i\boldsymbol{\sigma} \cdot (\mathbf{a} \times \mathbf{b}), \tag{3.41}$$

and the definition of magnetic field $\mathbf{B} = \nabla \times \mathbf{A}$, the equation reduces to,

$$i\hbar \frac{\partial}{\partial t} \phi = \left[\frac{1}{2m} (\mathbf{p} + e\mathbf{A})^2 - e\Phi + \frac{e\hbar}{2m} \boldsymbol{\sigma} \cdot \mathbf{B} \right] \phi. \tag{3.42}$$

This is the Pauli equation.

Spin-orbit interaction in a spherically symmetric potential

In order to derive the spin-orbit energy in a radial potential we follow Schiff [36]. Consider $\mathbf{A}(\mathbf{r},t) = 0$ and $\Phi(\mathbf{r},t) = \Phi(r)$, then the Dirac equation can be written as

$$i\hbar\frac{\partial}{\partial t}\Psi = [c\boldsymbol{\alpha}\cdot\mathbf{p} + \beta mc^2 + V]\Psi, \tag{3.43}$$

where we define $V = -e\Phi$. The orbital angular momentum $\mathbf{L} = \mathbf{r}\times\mathbf{p}$ is not a constant of motion, since it does not commute with the Hamiltonian and its time rate of change is given by

$$i\hbar\frac{d}{dt}L_x = [L_x, H] = -i\hbar c(\alpha_z p_y - \alpha_y p_z). \tag{3.44}$$

Here we have used the fact that $\mathbf{L}$ commutes with any spherically symmetric function. Consider another operator $\mathbf{\Sigma} = \begin{pmatrix} \boldsymbol{\sigma} & 0 \\ 0 & \boldsymbol{\sigma} \end{pmatrix}$. Its time rate of change is obtained as,

$$i\hbar\frac{d}{dt}\Sigma_x = [\Sigma_x, H] = 2ic(\alpha_z p_y - \alpha_y p_z). \tag{3.45}$$

From the above two results it is clear that the operator $\mathbf{J} = \mathbf{L} + \frac{1}{2}\hbar\mathbf{\Sigma}$ commutes with the Hamiltonian and it is a constant of motion. Furthermore, $\mathbf{S} = \frac{1}{2}\hbar\mathbf{\Sigma}$ is the spin angular momentum of the electron. The time-independent version of the Dirac equation written in terms of two component spinors $\Psi = \begin{pmatrix} \phi \\ \chi \end{pmatrix}$ for a spherically symmetric potential is,

$$(\epsilon - V)\phi = c\boldsymbol{\sigma}\cdot\mathbf{p}\chi, \tag{3.46}$$

$$(\epsilon - V + 2mc^2)\chi = c\boldsymbol{\sigma}\cdot\mathbf{p}\phi. \tag{3.47}$$

By using the derivation in going from the Dirac to the Pauli equation shown in the previous subsection, we derive an equation for ϕ alone

$$\epsilon\phi = \frac{1}{2m}\boldsymbol{\sigma}\cdot\mathbf{p}\left(1+\frac{\epsilon - V}{2mc^2}\right)^{-1}\boldsymbol{\sigma}\cdot\mathbf{p}\phi + V\phi. \tag{3.48}$$

If we retain only the lowest order terms in $(\epsilon - V)/2mc^2$, then $(1+\frac{\epsilon-V}{2mc^2})^{-1} \approx 1 - \frac{\epsilon-V}{2mc^2}$. Furthermore, we have $\mathbf{p}V = V\mathbf{p} - i\hbar\nabla V$ and $(\boldsymbol{\sigma}\cdot\nabla V)(\boldsymbol{\sigma}\cdot\mathbf{p}) = (\nabla V)\cdot\mathbf{p} + i\boldsymbol{\sigma}\cdot((\nabla V)\times\mathbf{p})$. Using these properties the above equation becomes,

$$\epsilon\phi = \left[\left(1-\frac{\epsilon - V}{2mc^2}\right)\frac{\mathbf{p}^2}{2m} + V\right]\phi - \frac{\hbar^2}{4m^2c^2}(\nabla V)\cdot(\nabla\phi) + \frac{\hbar^2}{4m^2c^2}\boldsymbol{\sigma}\cdot[(\nabla V)\times\mathbf{p}]\phi. \tag{3.49}$$

In addition, for spherically symmetric V, we have the relations $(\nabla V)\cdot\nabla = \frac{dV}{dr}\frac{\partial}{\partial r}$ and $\nabla V = \frac{1}{r}\frac{dV}{dr}\mathbf{r}$. We can then write,

$$\epsilon\phi = \left[\frac{\mathbf{p}^2}{2m} - \frac{\mathbf{p}^4}{8m^3c^2} + V - \frac{\hbar^2}{4m^2c^2}\frac{dV}{dr}\frac{\partial}{\partial r} + \frac{1}{2m^2c^2}\frac{1}{r}\frac{dV}{dr}\mathbf{L}\cdot\mathbf{S}\right]\phi. \tag{3.50}$$

The first and third term on the right hand side yield the Schrödinger equation. The second term is a relativistic mass correction which can be obtained by a second order expansion of the square root in $(\mathbf{p}^2c^2 + m^2c^4)^{1/2} - mc^2 \approx \frac{\mathbf{p}^2}{2m} - \frac{\mathbf{p}^4}{8m^3c^2}$. The fourth term is the relativistic correction to the potential energy, the so-called scalar relativistic term. The last term proportional to $\mathbf{L}\cdot\mathbf{S}$ couples the spin and orbital degrees of the electron and is the spin-orbit energy.

Spin-orbit coupling in the SIESTA code

Here we summarize the basic scheme of how spin-orbit coupling terms are calculated in the linear combination of atomic orbitals based SIESTA and SMEAGOL codes. We follow Ref. [38]. The prescription for including the relativistic effects in the pseudopotential generation was given by Kleinman [39]. One begins by solving self-consistently either the all-electron Dirac equation or its approximation, the Pauli equation, for a single atom and extracts the pseudopotential V_j, where $j = l \pm 1/2$ is now the total angular momentum. This can be rewritten in terms of projectors as,

$$\hat{V} = \sum_{j,m_j} |j, m_j\rangle \, V_j \, \langle j, m_j|. \tag{3.51}$$

Furthermore, this can be recast in a non-relativistic form by expressing $|j, m_j\rangle$ as a tensor product between the angular momentum states $|l, m\rangle$ and the eigenstates of the z component of the Pauli matrix [40],

$$\begin{aligned} |j = l + \frac{1}{2}, m_j\rangle &= \begin{pmatrix} \sqrt{\frac{l+m_j+\frac{1}{2}}{2l+1}} \; |l, m_j - \frac{1}{2}\rangle \\ \sqrt{\frac{l-m_j+\frac{1}{2}}{2l+1}} \; |l, m_j + \frac{1}{2}\rangle \end{pmatrix}, \\ |j = l - \frac{1}{2}, m_j\rangle &= \begin{pmatrix} \sqrt{\frac{l-m_j+\frac{1}{2}}{2l+1}} \; |l, m_j - \frac{1}{2}\rangle \\ -\sqrt{\frac{l+m_j+\frac{1}{2}}{2l+1}} \; |l, m_j + \frac{1}{2}\rangle \end{pmatrix}. \end{aligned} \tag{3.52}$$

Then equation 3.51 can be rewritten as

$$\begin{aligned} \hat{\mathbf{V}} &= \hat{\mathbf{V}}^{sc} + \hat{\mathbf{V}}^{SO} = \\ &= \sum_{l,m} [\, \bar{V}_l \, I_\sigma + \bar{V}_l^{SO} \mathbf{L} \cdot \mathbf{S} \,] \; |l, m\rangle\langle l, m|, \end{aligned} \tag{3.53}$$

where bold letters indicate 2×2 matrices and I_σ is the identity matrix in spin space,

$$\mathbf{L} \cdot \mathbf{S} = \frac{1}{2} \begin{pmatrix} \hat{L}_z & \hat{L}_- \\ \hat{L}_+ & -\hat{L}_z \end{pmatrix}, \tag{3.54}$$

and,

$$\begin{aligned} \bar{V}_l &= \frac{1}{2l+1}[(l+1)V_{l+\frac{1}{2}} + lV_{l-\frac{1}{2}}], \\ \bar{V}_l^{SO} &= \frac{2}{2l+1}[V_{l+\frac{1}{2}} - V_{l-\frac{1}{2}}]. \end{aligned} \tag{3.55}$$

Now, the $\hat{\mathbf{V}}^{SO}$ part of the pseudopotential also includes the scalar relativistic term discussed in the previous section. Using the above, the Kohn-Sham Hamiltonian now reads,

$$\hat{\mathbf{H}} = \hat{\mathbf{T}} + \hat{\mathbf{V}}^{sc} + \hat{\mathbf{V}}^{SO} + \hat{\mathbf{V}}^{H} + \hat{\mathbf{V}}^{xc} \,. \tag{3.56}$$

where $\hat{\mathbf{T}}$ is the kinetic energy, $\hat{\mathbf{V}}^{sc}$ is the scalar relativistic term and $\hat{\mathbf{V}}^{SO}$ is the spin-orbit potential. $\hat{\mathbf{V}}^{H}$ and $\hat{\mathbf{V}}^{xc}$ are the Hartree and exchange-correlation potentials, respectively. This Hamiltonian is a 2×2 matrix,

$$\hat{\mathbf{H}} = \begin{bmatrix} \hat{H}^{\uparrow\uparrow} & \hat{H}^{\uparrow\downarrow} \\ \hat{H}^{\downarrow\uparrow} & \hat{H}^{\downarrow\downarrow} \end{bmatrix}, \tag{3.57}$$

where the off-diagonal spin mixing blocks may arise from the exchange and correlation potentials if the system is spin non-collinear and also from the spin-orbit potential.

In linear combination of atomic orbital methods the Kohn-Sham Hamiltonian eigenstates $|\psi_n\rangle$ are expanded over a set of localized basis orbitals

$|\phi_i\rangle$,

$$|\psi_n\rangle = \sum_i \begin{pmatrix} c_{n,i}^{\uparrow} \\ c_{n,i}^{\downarrow} \end{pmatrix} |\phi_i\rangle. \tag{3.58}$$

The Kohn-Sham equation is then projected onto the basis as,

$$\begin{bmatrix} H_{ij}^{\uparrow\uparrow} - \epsilon_n S_{ij} & H_{ij}^{\uparrow\downarrow} \\ H_{ij}^{\downarrow\uparrow} & H_{ij}^{\downarrow\downarrow} - \epsilon_n S_{ij} \end{bmatrix} \begin{bmatrix} c_{n,j}^{\uparrow} \\ c_{n,j}^{\downarrow} \end{bmatrix} = 0, \tag{3.59}$$

where $H_{ij}^{\sigma\sigma'} = \langle\phi_i|\hat{H}^{\sigma\sigma'}|\phi_j\rangle$ and $S_{ij} = \langle\phi_i|\phi_j\rangle$ are Hamiltonian and overlap matrix elements, respectively. Finally, the spin-orbit term is evaluated as

$$\begin{aligned} \mathbf{V}_{ij}^{SO} &= \langle\phi_i|\hat{\mathbf{V}}^{SO}|\phi_j\rangle = \\ &= \sum_{k,l_k,M_k} \langle\phi_i|\bar{V}_{l_k}^{SO}\mathbf{L}\cdot\mathbf{S}\,|l_k, M_k\rangle\,\langle l_k, M_k|\phi_j\rangle, \end{aligned} \tag{3.60}$$

where k is the atom on which the potential is centered. Also, $\bar{V}_{l_k}^{SO} = \bar{V}_l^{SO}(\mathbf{r} - \mathbf{d}_k)$ and $|l_k, M_k\rangle$ is the spherical harmonic centered at the same atomic position $\mathbf{d}_k$. Evaluating the spin-orbit energy from the above equation involves calculation of a significant number of three-centre integrals, which makes it computationally expensive. However, since the radial part of the spin-orbit potential is short-ranged, considering only the matrix elements where both orbitals and the pseudopotential are on the same atom is a good approximation. This reduces the computational effort since we need to compute only one-center integrals. The approximate matrix elements then reduce to,

$$\begin{aligned}\mathbf{V}_{ij}^{SO} &= \frac{1}{2}\sum_{k,l_k>0,M_k} \langle R_{n_i,l_i}|\bar{V}_{l_k}^{SO}|R_{n_j,l_j}\rangle \langle l_i,M_i| \begin{pmatrix} \hat{L}_z & \hat{L}_- \\ \hat{L}_+ & -\hat{L}_z \end{pmatrix} |l_k,M_k\rangle \langle l_k,M_k|l_j,M_j\rangle \\ &\approx \frac{1}{2}\langle R_{n_i,l_i}|\bar{V}_{l_i}^{SO}|R_{n_j,l_i}\rangle \langle l_i,M_i| \begin{pmatrix} \hat{L}_z & \hat{L}_- \\ \hat{L}_+ & -\hat{L}_z \end{pmatrix} |l_i,M_j\rangle \,\delta_{l_i,l_j}. \qquad (3.61)\end{aligned}$$

The above expression is then used to calculate the spin-orbit energies in the SIESTA and SMEAGOL codes.

3.2 Green's functions for transport

We begin by a reformulation of the electronic structure problem in terms of Green's functions. Consider a system described by the single-particle Hamiltonian H, such that

$$H\psi_n = \epsilon_n S\psi_n, \qquad (3.62)$$

where ψ_n are the single-particle eigenstates with eigenvalues ϵ_n and S is the overlap matrix. The wavefunctions are normalized such that $\psi_m^\dagger S\psi_n = \delta_{mn}$ and the completeness relation now reads: $\psi_n\psi_n^\dagger S = I_N$. The retarded Green's function for the system at energy E is defined to be

$$G(E) = [(E+i\delta)S - H]^{-1}, \qquad (3.63)$$

where $\delta \to 0^+$ is a positive infinitesimal quantity. The advanced Green's function is then obtained as $G^a(E) = G^\dagger(E) = [(E-i\delta)S - H]^{-1}$. The Hamiltonian can also be written in the spectral representation

$$H = \sum_{n=1}^{N} \epsilon_n S \psi_n \psi_n^\dagger S. \tag{3.64}$$

The retarded Green's function can then be rewritten as

$$G(E) = \sum_{n=1}^{N} \frac{1}{(E + i\delta) - \epsilon_n} \psi_n \psi_n^\dagger. \tag{3.65}$$

The spectral function is defined as

$$A(E) = i[G(E) - G^\dagger(E)], \tag{3.66}$$

and it can be related to the density of states as

$$\begin{aligned} A(E) &= i \sum_{n=1}^{N} \frac{1}{(E + i\delta) - \epsilon_n} \psi_n \psi_n^\dagger - \frac{1}{(E - i\delta) - \epsilon_n} \psi_n \psi_n^\dagger \\ &= \sum_{n=1}^{N} \frac{2\delta}{(E - \epsilon_n)^2 + \delta^2} \psi_n \psi_n^\dagger \end{aligned} \tag{3.67}$$

In the limit $\delta \to 0^+$,

$$A(E) = 2\pi \sum_{n=1}^{N} \delta(E - \epsilon_n) \psi_n \psi_n^\dagger. \tag{3.68}$$

Using the definition of density of states (DOS) $\mathcal{N} = \sum_{n=1}^{N} \delta(E - \epsilon_n)$, and normalization of ψ_n,

$$\mathcal{N}(E) = \frac{1}{2\pi} \mathrm{Tr}(A(E)S) \tag{3.69}$$

The total DOS can be split up into the contributions originating from different orbitals as the projected density of states (PDOS),

$$\mathcal{N}(E) = \sum_{\mu=1}^{N} \mathcal{N}_\mu(E), \tag{3.70}$$

where the PDOS, $\mathcal{N}_\mu$, corresponding to orbital μ is

$$\mathcal{N}_\mu(E) = \frac{1}{2\pi} \sum_{\nu=1}^{N} A_{\mu\nu}(E) S_{\mu\nu}. \tag{3.71}$$

The density matrix, which is defined as,

$$\rho = \sum_{n=1}^{N} n_n \psi_n \psi_n^\dagger, \tag{3.72}$$

can also be expressed in terms of the spectral function (here n_n is the occupation of the n-th eigenstate). If we assume that the fermionic system is in a thermal equilibrium with the environment, then $n_n = f(\epsilon_n)$, where $f(\epsilon_n)$ is the Fermi-Dirac distribution evaluated at energy ϵ_n and the density matrix is then

$$\rho = \frac{1}{2\pi} \int dE f(E) A(E), \tag{3.73}$$

where the integral runs over the real energy axis from $-\infty$ to ∞.

Until now we have merely reformulated the electronic problem in the language of Green's functions. Now consider the system shown in Fig. 3.1. This is a typical transport setup, where the system to be studied can be divided into a scattering region and a left-hand side and a right-hand side lead. The scattering region is the central part of the setup which interacts with the two leads, while the leads themselves do not interact directly.

The Hamiltonian for this two-terminal device can be expressed in the form

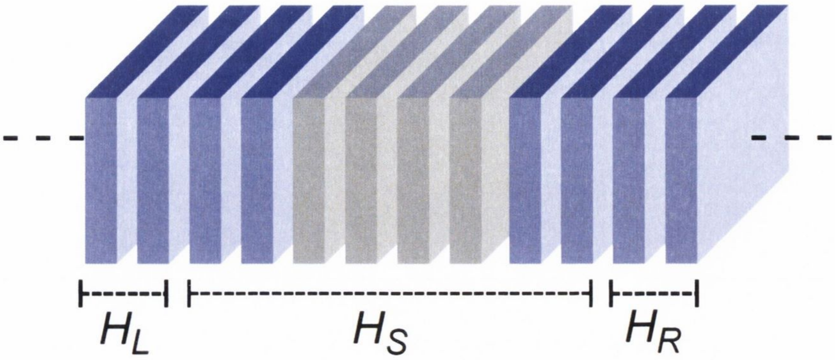

Figure 3.1: Schematic of the two-terminal transport setup with the scattering region and the left and the right leads.

$$H = \begin{pmatrix} H_L & H_{LS} & 0 \\ H_{SL} & H_S & H_{SR} \\ 0 & H_{RS} & H_R \end{pmatrix}, \tag{3.74}$$

where H_L and H_R are the left and right lead Hamiltonians and H_S is the Hamiltonian for the isolated scattering region. The terms H_{LS} and H_{SR} represent the hopping from the left lead to the scattering region and right lead to the scattering region, respectively. Here we have assumed that the scattering region is large enough such that there are no direct hopping elements between the left and the right lead. Define a matrix K such that $K = H - (E + i\delta)S$. In matrix notation

$$K = \begin{pmatrix} K_L & K_{LS} & 0 \\ K_{SL} & K_S & K_{SR} \\ 0 & K_{RS} & K_R \end{pmatrix}. \tag{3.75}$$

The retarded Green's function for the system, $G = [(E+i\delta)S-H]^{-1} = -K^{-1}$ is then obtained as

$$G = \begin{pmatrix} G_L + T_{LS}G_ST_{SL} & T_{LS}G_S & T_{LS}G_ST_{SR} \\ G_ST_{SL} & G_S & G_ST_{SR} \\ T_{RS}G_ST_{SL} & T_{RS}G_S & G_R + T_{RS}G_ST_{SL} \end{pmatrix}, \tag{3.76}$$

where $G_L = -K_L^{-1}$ and $G_R = -K_R^{-1}$ are the Green's functions for the isolated left and right leads, respectively. The transfer matrices are

$$\begin{aligned} T_{LS} &= G_LK_{LS}, \\ T_{SL} &= K_{SL}G_L, \\ T_{RS} &= G_RK_{RS}, \\ T_{SR} &= K_{SR}G_R. \end{aligned} \tag{3.77}$$

The Green's function of the scattering region is given by

$$G_S = (-K_S - \Sigma_L - \Sigma_R)^{-1}, \tag{3.78}$$

where the left and right self-energies are defined as

$$\Sigma_L = K_{SL}G_LK_{LS}, \quad \Sigma_R = K_{SR}G_RK_{RS}. \tag{3.79}$$

The quantities ρ_S and H_S are calculated self-consistently for the given self-energies. In a nutshell, the Green's function scheme allows calculating properties of a system with the boundary conditions set by the self-energies. We then introduce the spectral function for the scattering region

$$A_S = i(G_S - G_S^\dagger). \tag{3.80}$$

The left and right broadening matrices are defined as

$$\Gamma_L = i(\Sigma_L - \Sigma_L^\dagger), \quad \Gamma_R = i(\Sigma_R - \Sigma_R^\dagger). \tag{3.81}$$

We assume that the leads are semi-infinite. This implies that the Fermi energy is set by the leads. This is in contrast to a usual density functional theory calculation, where the number of electrons in the system is fixed, and this determines the Fermi energy. In this case, the Fermi energy in the leads sets the number of electrons in the scattering region. The spectral function for the scattering region can be written as

$$A_S = A_{SL} + A_{SR}, \tag{3.82}$$

where $A_{SL} = G_S \Gamma_L G_S^\dagger$ and $A_{SR} = G_S \Gamma_R G_S^\dagger$ are the parts of spectral function generated from the left and right lead, respectively. Analogously to the spectral function, the density matrix of the scattering region can be broken up into the contributions from the left and the right lead, $\rho_S = \rho_{SL} + \rho_{SR}$. Here,

$$\rho_{SL} = \int dE \sum_{n=1}^{N_L} p_{L,n}(E) \mathcal{N}_{L,n}(E) \psi_{L,n}^S \psi_{L,n}^{S\dagger}, \tag{3.83}$$

$$\rho_{SR} = \int dE \sum_{n=1}^{N_R} p_{R,n}(E) \mathcal{N}_{R,n}(E) \psi_{R,n}^S \psi_{R,n}^{S\dagger}, \tag{3.84}$$

where $\psi_{L/R,n}^S$ is the wavefunction extending over the scattering region and $p_{L/R,n}(E)$ is the occupation of the n-th state. Assuming a thermal equilibrium of the leads, $p_{L/R,n} = f_{L/R}(E)$, where $f_{L/R}(E)$ is the Fermi-Dirac distribution with each lead having a Fermi energy $E_{F,L/R}$. This allows introducing a bias voltage, V_b, between the two leads as $eV_b = E_{F,L} - E_{F,R}$. One possible choice is to use the Fermi level of the system at equilibrium, E_F, as the reference and set $E_{F,L} = E_F + eV_b/2$ and $E_{F,R} = E_F - eV_b/2$. It is then possible to write

$$\rho_{SL} = \frac{1}{2\pi}\int dE f_L(E) A_{SL}, \quad \rho_{SR} = \frac{1}{2\pi}\int dE f_R(E) A_{SR}. \tag{3.85}$$

One can then define the lesser Green's function of the scattering region

$$G_S^< = iG_S(f_L(E)\Gamma_L + f_R(E)\Gamma_R)G_S^\dagger \tag{3.86}$$

Using above machinery, we obtain the canonical equation of non-equilibrium Green's function formalism

$$\rho_S = \frac{1}{2\pi}\int dE G_S^<(E). \tag{3.87}$$

It is possible to decompose the lesser Green's function into an equilibrium and a non-equilibrium part, $G_S^< = G_{S,\mathrm{eq}}^< + G_{S,\mathrm{neq}}^<$, where

$$G_{S,\mathrm{eq}}^< = -\frac{1}{2}\left[f_L(E) + f_R(E)\right](G_S - G_S^\dagger). \tag{3.88}$$

$$G_{S,\mathrm{neq}}^< = \frac{i}{2}\left[f_L(E) - f_R(E)\right]G_S(\Gamma_L - \Gamma_R)G_S. \tag{3.89}$$

This decomposition allows us to write an analytic continuation of $G_{S,\mathrm{eq}}^<$ to complex energies, E. It does not have poles for $\mathrm{Im}(E) > 0$. Thus, one can replace the integral over the real energy axis, to obtain ρ, by one over the positive half of the complex plane. Here $G_{S,\mathrm{eq}}^<$ is smoother requiring less energy points for integration. The non-equilibrium part, $G_{S,\mathrm{neq}}^<$, still needs to be integrated over the real energy axis. However, it is non-zero only in the bias window where $f_L(E) \neq f_R(E)$ and of course does not contribute in the special case of zero bias calculations.

The electronic charge in the scattering region is

$$q_S = \psi^{S\dagger} S_S \psi^S. \tag{3.90}$$

By assuming that the states, ψ^S, satisfy a Schrödinger-like time-dependent equation $H\psi = i\hbar S\frac{\partial\psi}{\partial t}$, the time dependent wavefunction can be written as $\psi(t) = e^{-iEt/\hbar}\psi$. In this case

$$\frac{\partial q_S}{\partial t} = \frac{\partial(\psi^{S\dagger}(t) S_S \psi^S(t))}{\partial t} = 0. \tag{3.91}$$

This is a form of the continuity equation and can be made plausible by noting that the charge inflow from left lead balances the charge outflow from the right lead. The individual contributions to the current can be obtained as follows

$$\begin{aligned}
\frac{\partial q_S}{\partial t} &= \frac{\partial(\psi^{S\dagger}(t) S_S \psi^S(t))}{\partial t} \\
&= \frac{\partial\psi^{S\dagger}(t)}{\partial t} S_S \psi^S(t) + \psi^{S\dagger}(t) S_S \frac{\partial\psi^S(t)}{\partial t} \\
&= \frac{i}{\hbar}(\psi^{L\dagger} K_{LS} \psi^S - \psi^{S\dagger} K_{SL} \psi^L) + \frac{i}{\hbar}(\psi^{R\dagger} K_{RS} \psi^S - \psi^{S\dagger} K_{SR} \psi^R)
\end{aligned} \tag{3.92}$$

From the above, current corresponding to each lead can be identified,

$$I_L = \frac{i}{\hbar}(\psi^{L\dagger} K_{LS} \psi^S - \psi^{S\dagger} K_{SL} \psi^L), \quad I_R = \frac{i}{\hbar}(\psi^{R\dagger} K_{RS} \psi^S - \psi^{S\dagger} K_{SR} \psi^R). \tag{3.93}$$

Notice that $I_L + I_R = 0$. The total current from the left lead is the sum over all states

$$I_L = \int dE \sum_{n=1}^{N_L} f_L(E)\mathcal{N}_{L,n}(E) I^L_{L,n} + \int dE \sum_{n=1}^{N_R} f_R(E)\mathcal{N}_{R,n}(E) I^L_{R,n}, \quad (3.94)$$

where

$$I^L_{L,n} = \frac{i}{\hbar}(\psi^{L\dagger}_{L,n} K_{LS} \psi^S_{L,n} - \psi^{S\dagger}_{L,n} K_{SL} \psi^L_{L,n}) \quad (3.95)$$

is the current due to the n-th state $\psi_{L,n}$ originating in the left lead and

$$I^L_{R,n} = \frac{i}{\hbar}(\psi^{L\dagger}_{R,n} K_{LS} \psi^S_{R,n} - \psi^{S\dagger}_{R,n} K_{SL} \psi^L_{R,n}), \quad (3.96)$$

is the current due to the n-th state $\psi_{R,n}$ originating in the right lead. Using these expressions the total current from the left lead, carried by the states originating in the left lead (I^L_L) and carried by the states originating in the right lead (I^L_R) can be written as

$$I^L_L = \frac{1}{h}\int dE f_L(E)\mathrm{Tr}(\Gamma_L G^\dagger_S \Gamma_R G_S), \quad I^L_R = -\frac{1}{h}\int dE f_R(E)\mathrm{Tr}(\Gamma_L G^\dagger_S \Gamma_R G_S). \quad (3.97)$$

The transmission function from the left to right lead at energy E is obtained as

$$T(E) = \mathrm{Tr}(\Gamma_L G^\dagger_S \Gamma_R G_S). \quad (3.98)$$

The probability current is then given by

$$I^L = \frac{1}{h}\int dE T(E)(f_L(E) - f_R(E)), \quad (3.99)$$

and the resulting charge current is then obtained by multiplying by electron charge e,

$$I = \frac{e}{h} \int dE T(E)(f_L(E) - f_R(E)). \tag{3.100}$$

This is the well-known Landauer-Büttiker formula. The Green's function formalism allows us to write a rigorous description of coherent electronic transport and is used to tackle most of the transport problems studied in this thesis. However, it does not include inelastic effects which can be incorporated by means of additional self-energies. Furthermore, while using this formalism in conjunction with density functional theory, one must exercise caution since there is no variational principle out of equilibrium.

Chapter 4

Andreev reflection in two dimensional topological insulators

A metal/superconductor interface may reflect an incident electron from the metal as a positively charged hole with opposite spin, while a Cooper pair is formed in the superconductor. This electron-hole conversion is known as Andreev reflection [41] and has long served as a useful probe for spin-polarized currents [42]. Given the spin polarized nature of its edge states, Andreev reflection technique appears to be particularly suited to study edge state scattering in topological insulators and its heterostructures [43, 44, 45]. Also intriguing is the possibility of interfacing $\mathbb{Z}_2$ insulators with superconductors (SCs). This interface has been predicted to host Majorana fermions, with possible applications in topological quantum computing [46].

In this chapter we study Andreev reflection processes in two-dimensional topological insulators, with either conserved or broken time reversal symmetry, forming an interface with a superconductor with uniform s-wave pairing. Both classes of topological insulators exhibit perfect Andreev reflection, which is robust against disorder. This is assigned to topologically protected edge states. In the time-reversal symmetric case we show that doping one of the ribbon edges with magnetic impurities suppresses one Andreev channel, while no such suppression is seen in the broken symmetry situation. Based on this observation we suggest a tabletop transport experiment able to distinguish between the two types of topological insulators, which does not involve the direct measurement of the material band structure.

4.1 Andreev reflection at topological insulator superconductor junction

We consider a two-dimensional topological insulator ribbon realized on a honeycomb lattice with zig-zag edge geometry, as shown in Fig. 4.1. The region to the right (SC region) is proximity coupled to a superconducting electrode, while the region on the left (TI region) is the topological insulator. The electron and hole spectra are described at the mean-field level by the Bogoliubov-de Gennes equation [48]

$$\begin{pmatrix} H - E_F & \Delta \\ \Delta^* & E_F - \mathcal{T} H \mathcal{T}^{-1} \end{pmatrix} \begin{pmatrix} u \\ v \end{pmatrix} = \varepsilon \begin{pmatrix} u \\ v \end{pmatrix} , \tag{4.1}$$

where u and v are the wave functions for electrons and holes, respectively. H is the single-particle Hamiltonian for the topological insulators, $\mathcal{T}$ is the time-reversal operator, Δ is the pairing potential and E_{F} is the Fermi level. In the left region (TI) the pairing potential is set to zero, i.e., there is no superconductivity. In the right region (SC) a finite constant pairing potential exists due to the proximity with a superconducting electrode.

4.1.1 Models and Computational Details

We use the Kane-Mele model [27] as single-particle Hamiltonian for the time-reversal symmetric ($\mathbb{Z}_2$) topological insulator. This reads

$$H_{\mathrm{KM}} = t\sum_{\langle ij\rangle} c_i^\dagger c_j + \lambda \sum_i \xi_i c_i^\dagger c_i + it_2 \sum_{\langle\langle ij\rangle\rangle} \nu_{ij} c_i^\dagger \sigma^z c_j \,. \tag{4.2}$$

Here the first term is just the nearest-neighbour hopping with strength t, where the spin indices of the creation, $c_i^\dagger$, and annihilation, c_i, operators have been omitted. The second term represents a staggered sub-lattice potential, i.e., the A type sub-lattice has an on-site energy λ ($\xi = +1$), while the B sub-lattice has on-site energy $-\lambda$ ($\xi = -1$). The last term describes the second nearest-neighbour hopping with strength t_2 and it is purely imaginary (t_2 is real and $i = \sqrt{-1}$). Furthermore, ν_{ij} is equal to $+1$ for anti-clockwise hopping and to -1 for clockwise. Here σ^z is the z-component Pauli matrix describing the electron's spin. The last term can be thought as a mirror-symmetric spin-orbit interaction, since it couples the orbital motion of the electrons to their spins.

For the time-reversal symmetry broken case we use a spinful version of the Haldane model [49], proposed by Chen *et al.* [50] (from now on the spin-Haldane model, SH). The single-particle Hamiltonian reads

$$H_{\mathrm{SH}} = t\sum_{\langle ij\rangle} c_i^\dagger c_j + \gamma \sum_i c_i^\dagger \sigma^z c_i + i\beta(\gamma) \sum_{\langle\langle ij\rangle\rangle} \nu_{ij} c_i^\dagger c_j \,, \tag{4.3}$$

where the second term is the exchange field with strength γ , i.e., it represents Zeeman coupling. In addition to spin, the orbital angular momentum of the electron, ν_{ij}, is also coupled to the exchange field. Following Chen *et*

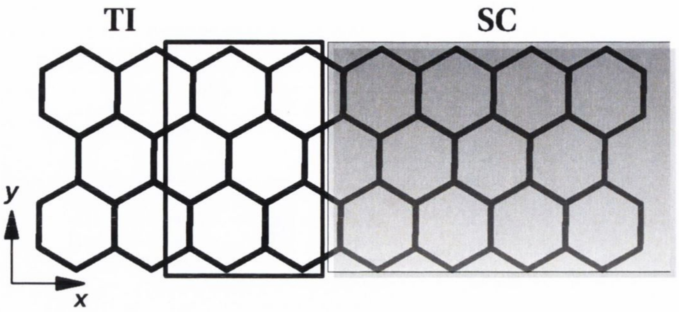

Figure 4.1: Setup for calculating the two-terminal transmission. Region SC is proximity coupled to a superconducting electrode while region TI is the topological insulator described by the two chosen single-particle models. The rectangle marks the region at the TI/SC interface where disorder is introduced.

al. [50] we approximate $\beta(\gamma) \approx \beta\text{sgn}(\gamma)$, and choose β to be negative. This parameter set describes a diamagnetic response to the magnetic field γ. Note that in this case the second nearest-neighbour hopping term has the same sign for both the spins, as opposed to that in H_{KM}.

We then use the ballistic Landauer-Büttiker scheme [51] for calculating the transmission across the system as presented in Chapter 3. The self-energy matrix Σ_{L} (Σ_{R}) for the left-hand side (right-hand side) contact is obtained by using the electrodes' surface Green's function, g_s. This is calculated iteratively from the following equation [52]

$$g_s = [(E + i0^+)I - H_0 - H_1 g_s H_1^\dagger]^{-1}, \tag{4.4}$$

where H_0 is the Hamiltonian describing the electrode unit cell and H_1 is the coupling matrix between cells (note that in our tight-binding formulation the Hamiltonian of the ribbon has a tri-diagonal form). The self-energy matrices are given by $\Sigma_{\text{L,R}} = H_{\text{L,R}} g_s H_{\text{L,R}}^\dagger$, where H_{L} (H_{R}) is the coupling matrix between the scattering region and the left-hand side (right-hand side) contact. Then, the retarded Green's function, G^r, for the scattering region of Hamiltonian H_{SC} is obtained as $G^r = [(E + i0^+)I - H_{\text{SC}} - \Sigma_{\text{L}} - \Sigma_{\text{R}}]^{-1}$.

The scattering region comprises the SC/TI interface and a portion of the electrodes. Finally the total transmission is simply $T(E) = \mathrm{Tr}(\Gamma_\mathrm{L} G^r \Gamma_\mathrm{R} G^{r\dagger})$, where $\Gamma_\mathrm{L,R}$ are the broadening matrices $\Gamma_\mathrm{L,R} = i[\Sigma_\mathrm{L,R} - \Sigma^\dagger_\mathrm{L,R}]$. Furthermore, the normal transmission coefficient from the n-th terminal to the m-th one is obtained as $T_{nm\sigma}(E) = \mathrm{Tr}(\Gamma_{n\sigma} G^r_{\sigma\sigma} \Gamma_{m\sigma} G^{r\dagger}_{\sigma\sigma})$, while the Andreev reflection coefficient is calculated as

$$R^\mathrm{A}_{n\sigma,m\bar{\sigma}}(E) = \mathrm{Tr}(\Gamma_{n\sigma} G^r_{\sigma\bar{\sigma}} \Gamma_{m\bar{\sigma}} G^{r\dagger}_{\bar{\sigma}\sigma}), \tag{4.5}$$

where $\sigma = (\uparrow, \downarrow)$ and $\bar{\sigma} = (\downarrow, \uparrow)$ are the spin indices. Thus, $R^\mathrm{A}_{n\sigma,m\bar{\sigma}}$ describes an incident electron from terminal n being reflected as an opposite spin hole into terminal m. An expanded discussion of Blonder-Tinkham-Klapwijk model for a normal metal-superconductor junction and its application to Andreev reflection is presented in Appendix C.

4.1.2 Results

We begin our analysis by calculating R^A as a function of energy, which is shown in Figs. 4.2(a) and 4.2(b), respectively, for the Kane-Mele and spin-Haldane model. Henceforth, we set the nearest neighbor hopping $t = 1$ and measure all the energies in units of t. Furthermore, we fix the number of sites along the ribbon width to be $n_y = 18$. The insets of Fig. 4.2 show the band structure for the two models calculated in this strip geometry. In the bulk gap there exist gapless edge modes, a single pair on each edge. For the H_KM Hamiltonian, these are opposite spin Kramers' pairs, while for H_SH, there are two left movers (one for each spin) at one edge and two right movers at the other, exactly as the integer quantum Hall states. We find that for both these cases, the edge modes lead to a perfect Andreev reflection for electrons with energy smaller than the superconducting gap. In fact, in both

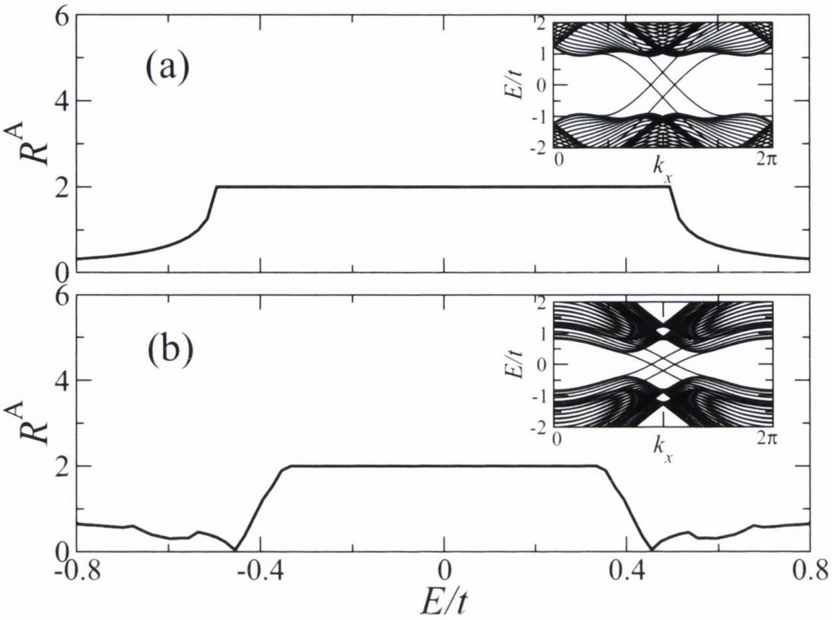

Figure 4.2: Andreev reflection coefficient for (a) $\mathbb{Z}_2$ and (b) Chern insulators showing perfect Andreev reflection for electron energies smaller than the superconducting gap. The insets show the band structure for the two models solved in a ribbon geometry. Here we choose $t_2 = 0.33$, $\lambda/t_2 = 2.0$, $\gamma = 0.20$, $\beta = -0.11$ and $\Delta = 0.50$. The Fermi level E_F is set at zero.

cases the edge modes are perfectly Andreev reflected. Normal reflection, where an incident particle is reflected back without being converted into its antiparticle, is completely suppressed for the edge states as long as the Fermi energy lies in the bulk gap, as we have verified numerically. These findings are consistent with recent theoretical and experimental studies for time-reversal symmetric topological insulators [53, 54]. Note that by using a low-energy effective model for the edge states of a time-reversal symmetric TI, Adroguer *et al.* [43] suggested Andreev reflection as a probe for helical edge states. Here we predict perfect Andreev reflection also for the time-reversal symmetry broken case.

Next, we study whether such perfect Andreev reflection is robust to perturbations of the electronic structure at the SC/TI interface. To this goal we consider the effect of onsite disorder, which is introduced by adding a term of the form $H_{\text{disorder}} = \sum_i w_i c_i^\dagger c_i$ to both H_{KM} and H_{SH}. Hence disorder enters in an exact and rather natural way in our numerical approach, at variance to low-energy edge models, where either a field theory construction or a perturbative treatment needs to be adopted. In particular, here we choose the onsite energy, w_i, to be randomly distributed within the interval $[-W/2, W/2]$. Such disorder is introduced in a $n_x = 15$ site-long region near the SC/TI interface. From Fig. 4.3 it can be clearly seen that the Andreev reflection process is very robust against disorder. Even for moderately large disorder ($W \approx 2.0t$), R^{A} remains perfectly quantized. This is attributed to the presence of the topologically protected edge states, which are highly immune to impurities and disorder, and the situation is identical for both classes of topological insulators. For $W > 2.0t$ fluctuations in R^{A} begin to develop in the energy range where only edge states exist. As a result the Fano factor becomes non-zero. This signals a transition from ballistic to diffusive transport where backscattering is allowed and the edge states are no longer topologically protected [55]. Note that the actual value of the disorder strength critical for the destruction of the edge states depends on the robustness of the topological phase itself, i.e., on the model parameters used. However, as we will argue in what follows, the introduction of magnetic impurities break the topological protection of $\mathbb{Z}_2$ insulators, even at weak disorder strengths, i.e., it is a general feature, which depends little on the model parameters.

This is demonstrated by introducing magnetic impurities at one of the TI ribbon edges. The exchange coupling between the electron spin and the impurities is incorporated into the model as [56]

$$H_{\mathrm{ex}} = \sum_{i,\alpha,\beta} c^{\dagger}_{i\alpha} \left[J_z \sigma_z^{\alpha\beta} S_z^i + J_{\parallel} (\sigma_x^{\alpha\beta} S_x^i + \sigma_y^{\alpha\beta} S_y^i) \right] c_{i\beta} \,, \tag{4.6}$$

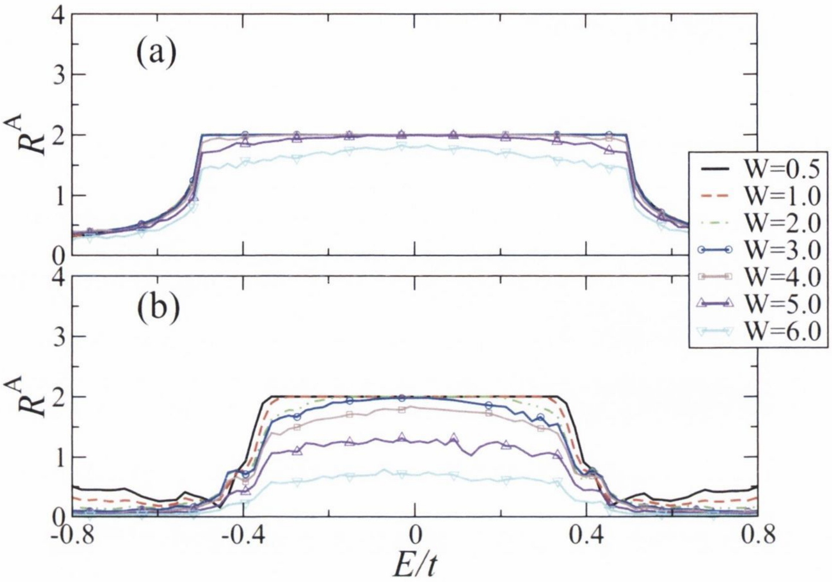

Figure 4.3: Effect of onsite disorder on the Andreev reflection coefficient for (a) $\mathbb{Z}_2$ and (b) Chern insulators. The Andreev process is highly robust against onsite disorder and the crossover to diffusive transport occurs for $W \approx 3.0t$ for the $\mathbb{Z}_2$ insulator and $W \approx 2.0t$ for the Chern insulator. Here again we set $t_2 = 0.33$, $\lambda/t_2 = 2.0$, $\gamma = 0.20$, $\beta = -0.11$ and $\Delta = 0.50$, and the Fermi level E_F is taken at zero. The curves are averaged over 960 random configurations.

where S_n^i is n-th spin component of the magnetic impurity located at the edge site i, and J_z and $J_\parallel$ are, respectively, the longitudinal and transverse exchange coupling. In the notation we have now explicitly re-introduced the spin index so that $c_{i\alpha}^\dagger$ ($c_{i\alpha}$) is the creation (annihilation) operator for an electron at site i with spin α. For simplicity here we have implicitly assumed that the magnetic impurities are not Kondo active. Their electronic structure is then treated at a simple classical level, i.e., they enter the model as classical spins. When one includes only the z component of the exchange coupling in the Kane-Mele model, there is a shift of the up and down spin edge bands, by an amount proportional to the coupling J_z but no band gap opens in the edge state spectrum. For small values of J_z, before the bulk band gap closes, the system is in the time-reversal symmetry broken quantum spin Hall phase predicted by Yang *et al.* [57]. As a consequence, although we have locally broken time-reversal symmetry, perfectly quantized Andreev reflection still occurs. This is because in the energy range within the superconducting gap there is only the counter-propagating opposite spin channel available to normal reflection. In contrast, if we also include the transverse component of the exchange, i.e., we take $J_{\parallel} \neq 0$, then a gap is opened at the edge where the magnetic impurities have been located. The destruction of the helical edge states at one of the two edges leads to a suppression of this channel, which results in the Andreev reflection coefficient dropping from two to one, as shown in Fig. 4.4(a). Such a reduction of R^{A} from 2 to 1 is almost perfect except for some bulk contributions at energies approximately equal to the superconducting gap. The situation for the spin-Haldane model is different and the magnetic impurities produce no effect, regardless of the magnitude of J_z and $J_{\parallel}$. This is expected, since the topological protection of the edge states for a Chern insulator continues to hold even in the absence of time-reversal symmetry. Consequently, no such suppression is observed and the Andreev reflection coefficient remains perfectly quantized to a value of two, as illustrated in Fig. 4.4(b).

Thus, we have shown that Andreev reflection measurements can characterize a topological insulator and distinguish it from a topologically trivial material. Perfect Andreev reflection provides a signature for the existence of topological edge states, although it is not unique to them. One can in fact envisage other systems, which display a similar perfect electron-hole conversion, for instance a pair of ballistic nanowires. What is unique, though, is the tremendous immunity to disorder, which both types of topological insulators display. Furthermore, we also showed that the $\mathbb{Z}_2$ and Chern insulators respond differently to the presence of magnetic impurities.

Based on the above observation we propose a transport experiment to

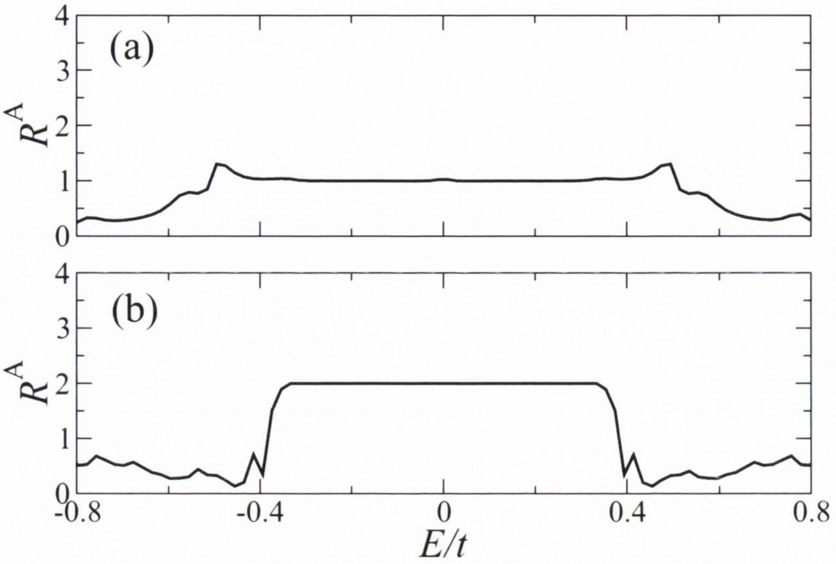

Figure 4.4: Andreev reflection coefficient in presence of magnetic impurities located at the edge of a TI ribbon: (a) $\mathbb{Z}_2$ insulator (b) Chern insulator. The suppression of one of the edge channels in the time-reversal symmetric case R^{A} produces a drop in R^{A} from 2 to 1. Magnetic impurities have no effect on the Andreev reflection for a time-reversal symmetry broken insulator. Here we have chosen $J_z = J_{\|} = 0.50$ and $|S| = 2$. The other parameters are the same as before.

distinguish between the two types of topological insulators. The experiment involves placing magnetic impurities along one of the edges of the two-dimensional sample, for instance, by using the tip of a scanning tunneling microscope. The impurities' spin will, in general, be aligned in arbitrary directions. The illumination with low-frequency polarized infrared light can however induce their alignment. This has been demonstrated, for instance, for Mn impurities in CdTe [58]. The infrared pulse imparts a momentum to align the impurity spins, which subsequently relax back to their random orientations. The Andreev reflection coefficient R^{A} can then be measured as a function of time, and this can be related to the inclination angle θ of the impurity spin S. The dependence of R^{A} on θ is shown in Fig. 4.5. As the spin rotates towards the z direction, R^{A} returns back to the perfectly quantized value of two, the same as that in the absence of impurities. For the Chern insulator the Andreev reflection process is unaffected by magnetic

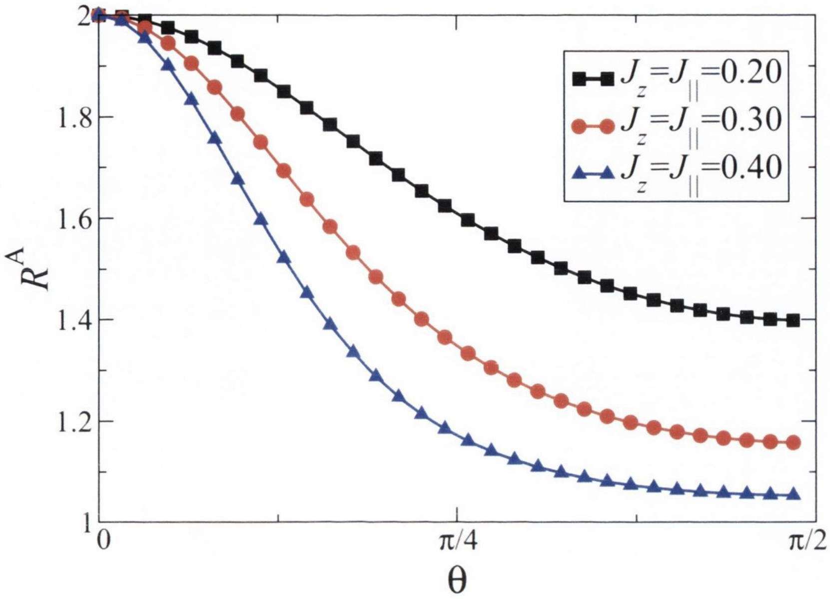

Figure 4.5: Andreev reflection coefficient in the presence of magnetic impurities for the $\mathbb{Z}_2$ insulator as a function of the spin inclination angle θ for various values of the exchange coupling. The relaxation of the spins leads to R^{A} reverting back towards unity.

impurities and thus to the exposure with polarized light.

A second possible route to spin polarize the impurities consists in applying an intense static magnetic field B perpendicular to the plane of the sample, and then to switch it off over a short time scale t_B. The impurity spins will then relax back to their random configuration with a typical spin-relaxation time t_S. During the time window comprised between t_B and t_S, measurements of R^{A} should yield a behavior similar to that shown in Fig. 4.5. Note that these possible approaches were already outlined in Ref. [59] relative to the observation of the Chern insulating phase in Mn doped HgTe quantum wells. The same here are broadened in scope and now become a tool for assigning a given material to one of the two classes of TIs. Such a strategy mitigates the need to perform a direct band-structure measurement, such as spin and angle resolved photoemission spectroscopy, and therefore represents a powerful tabletop characterization method of the topological state of a material.

4.1.3 Summary and Conclusions

In conclusion, we have investigated SC/TI heterojunctions and shown that they display perfect Andreev reflection. The robustness of the topologically protected edge states lends this effect a large immunity against disorder. We have then looked at the effect of magnetic impurities and shown that in the case of transverse exchange coupling the Andreev reflection coefficient of $\mathbb{Z}_2$ topological insulators drops from two to one. This observation allowed us to propose a transport experiment that is able to distinguish between the two types of topological insulators. This consists in following the time evolution of the Andreev reflection coefficient of a device dusted with magnetic impurities, which have been previously polarized.

Chapter 5

Spin-pumping at a quantum spin Hall edge

Given the peculiar spin structure of the quantum spin Hall (QSH) edge states it becomes natural to ask ourselves whether this can be used to manipulate magnetic objects [60]. In particular the question we address in this chapter is whether spin-pumping at the single spin level can be achieved without using spin-polarized electrodes or an external magnetic field. In a nutshell we wish to propose an analog to the numerous recent investigations concerning spin-flip inelastic electron tunneling spectroscopy (SF-IETS) for magnetic adatoms on insulating surfaces [61], either in equilibrium or in spin-pumping conditions [62].

In this chapter we demonstrate that a magnetic impurity deposited at the edge of a $\mathbb{Z}_2$ topological insulator (TI) and presenting a uniaxial magnetic anisotropy, which makes it non-Kondo-active [63], can be manipulated by the QSH current. Furthermore we show that the topological nature of the QSH state has profound consequences on the SF-IETS conductance spectrum. At low current intensity there is a complete suppression of the conductance steps appearing at the critical biases characteristic of the activation of an inelastic spin-scattering channel [61]. In contrast, for currents large enough to produce spin-pumping the spin of the magnetic impurity is driven away from the anisotropy axis. This breaks the topological protection of the helical edge states and the conductance steps reappear. Intriguingly, in this situation there is a strong dependence of the SF-IETS conductance spectrum on the bias polarity. In the final section of this chapter we extend our investigation to propose a four-terminal device designed to manipulate by all electrical means the spin of a magnetic adatom positioned at the edge of a QSH insulator. We show that an electrical gate, able to tune the interface resistance between the QSH insulator and the source and drain electrodes, can switch the device between two regimes: one where the system exhibits spin pumping and the other where the adatom remains in its ground state. Our calculations are conducted by using the non-equilibrium Green's function method for transport, in a tight-binding scheme, combined with a perturbative approach to spin-scattering from magnetic impurities [64, 65, 66].

5.1 Spin-pumping and inelastic electron tunneling spectroscopy

The device that we have in mind is schematically presented in Fig. 5.1 and consists of two semi-infinite current/voltage electrodes sandwiching a $\mathbb{Z}_2$ TI ribbon in which a magnetic impurity is absorbed at one of the two edges. Our working hypothesis is that one can construct such a device with either a strong or a weak electronic coupling between the electrodes and the ribbon, i.e., the interface resistance can be engineered. In the next section we show

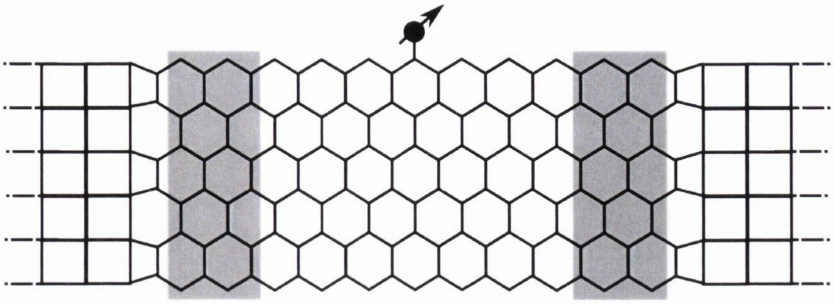

Figure 5.1: Schematic representation of the device considered comprising a TI with honeycomb lattice structure and a magnetic impurity adsorbed at one of the two edges. The shaded area corresponds to the interface region where a gate voltage is introduced.

how this can be achieved in practice by means of a gate voltage. The entire system is described at the tight binding level and for the electrodes we use a simple square lattice with hopping parameter, t_η, ($\eta = \mathrm{L}, \mathrm{R}$).

5.1.1 Model and Computational Details

The TI ribbon has a honeycomb lattice structure with zig-zag edge geometry and it is described by the two-dimensional Kane-Mele (KM) Hamiltonian, H_{KM}, which reads

$$H_{\mathrm{KM}} = \varepsilon_0 \sum_{i\alpha} \xi_i c^\dagger_{i\alpha} c_{i\alpha} + t_1 \sum_{\langle ij \rangle,\, \alpha} c^\dagger_{i\alpha} c_{j\alpha} + it_2 \sum_{\langle\langle ij \rangle\rangle,\, \alpha\beta} \nu_{ij} c^\dagger_{i\alpha} [\sigma^z]_{\alpha\beta} c_{j\alpha} \,. \tag{5.1}$$

We remind here that the first term describes a staggered sublattice potential with on-site energy ε_0 and ξ_i being $\xi_i = +1$ for the A sublattice and $\xi_i = -1$ for the B one. Here $c^\dagger_{i\alpha}$ ($c_{i\alpha}$) creates (annihilates) an electron at site i with spin α. The second term is the nearest neighbour hopping with strength t_1 (t_1 sets the energy scale of the problem). Finally the third term, which drives the topological phase, is a second nearest neighbour hopping with strength t_2 ($i = \sqrt{-1}$). This describes the coupling of the electrons orbital motion to their spins via the z-component of the Pauli matrices (σ^z). The parameter

ν_{ij} is $+1$ for counter-clockwise hopping and -1 for clockwise.

If we now attach an impurity at site I, the total electronic Hamiltonian will become

$$H_{\mathrm{el}} = H_{\mathrm{KM}} + \varepsilon_I \sum_{\alpha} c^{\dagger}_{I\alpha} c_{I\alpha} + t_I \sum_{\langle Ii \rangle,\, \alpha} c^{\dagger}_{I\alpha} c_{i\alpha}\,, \tag{5.2}$$

where in addition to H_{KM} one has the on-site potential of the impurity, ε_I, and the hopping between the impurity site I and its neighbor i on the honeycomb lattice (with strength t_I). Finally there are two other terms related to the magnetic impurity spin, $\mathbf{S}$

$$H_{\mathrm{sp}} = D S_z^2\,; \qquad H_{\mathrm{el-sp}} = J_{\mathrm{sd}} \sum_{\alpha\beta} c^{\dagger}_{I\alpha} [\boldsymbol{\sigma}]_{\alpha\beta} c_{I\beta} \cdot \mathbf{S}\,. \tag{5.3}$$

The first, H_{sp}, describes the uniaxial anisotropy (along z, which is perpendicular to the plane of the ribbon) with D being the zero-field splitting parameter. The second, $H_{\mathrm{el-sp}}$, couples the current-carrying electrons to the local impurity spin with interaction strength J_{sd} ($\boldsymbol{\sigma}$ is a vector of Pauli matrices). This is usually known as the *s*-*d* model for magnetism [68].

Electron transport is investigated within the Landauer-Büttiker approach [69] implemented by the non-equilibrium Green's function (NEGF) method. The central quantity to evaluate is the retarded electronic Green's function for the scattering region (the TI ribbon) in presence of the electrodes, $G^r = [(E + i0^+)I - H_{\mathrm{el}} - \Sigma_{\mathrm{L}} - \Sigma_{\mathrm{R}}]^{-1}$, where Σ_η ($\eta = $ L, R) are the electrodes self-energy, which can be computed with standard techniques. These depend on the hopping parameter between the ribbon and the electrodes, $t_{\eta\mathrm{SC}}$, whose magnitude sets the intensity of the current.

When the conducting electrons couple to the impurity spin ($J_{\mathrm{sd}} \neq 0$), the problem becomes intrinsically many-body in nature. This is made treat-able by constructing a perturbation theory in the electron-spin Hamiltonian, which allows us to incorporate the effect of the electron-spin interaction in an additional self-energy, $\Sigma_{\rm int}$. A derivation of this self-energy is provided in Appendix D. In this work we truncate the perturbation expansion to the second order [64, 66] in both the electron and the impurity spin propagator. The latter contains information about the state of the magnetic impurity spins, through the population, P_n, of the eigenvectors of the spin-Hamiltonian, $H_{\rm sp}$. In particular it is possible to show that the P_n's satisfy a master-equation of the form

$$\frac{dP_n}{dt} = \sum_l \Big[P_n(1-P_l)W_{ln} - P_l(1-P_n)W_{nl}\Big] + (P_n^0 - P_n)/\beta\,, \qquad (5.4)$$

where the detailed expression for the transition rates, W_{ln}, can be found in Appendix D, and $\beta = k_{\rm B}T$ with $k_{\rm B}$ being the Boltzmann constant and T the temperature. In Eq. [5.4] the populations P_n^0 are those of the ground state. With this at hand we can compute the current, I, and hence by numerical derivative the conductance, $G = {\rm d}I/{\rm d}V$.

5.1.2 Results

We start our discussion by first looking at the transport properties of the ribbon in absence of the magnetic impurity. The relevant quantity here is the spin-resolved total transmission coefficient along a particular edge [70], which is given by

$$T^s_{\alpha\alpha'}(\varepsilon_{\rm F}) = {\rm Tr}_{n_x}[\Gamma_{\rm L}G^r\Gamma_{\rm R}G^a]^s_{\alpha\alpha'}\,, \qquad (5.5)$$

where α is the spin index ($\alpha =\uparrow,\downarrow$), s labels the edges (s = top, bottom) and

G^a is the advanced Green's function. The trace is over the number of atoms, n_x, along the given edge and the transmission coefficient is evaluated at the Fermi energy, ε_{F}. As a matter of notation a (n_x, n_y) ribbon contains n_x atoms in the direction of transport and n_y along the transverse one. When the Fermi level is fixed at the half-filling point the ribbon is insulating in the bulk, but presents edge topological protected states (here $t_\eta = t_1 = 1$, and $t_2 = t_1/3$, which ensures that the KM Hamiltonian describes a QSH state). In this situation we find for a (11, 6) ribbon, $T^{\mathrm{top}}_{\uparrow\uparrow} = 0.9$, $T^{\mathrm{top}}_{\downarrow\downarrow} = 0.1$, $T^{\mathrm{bottom}}_{\uparrow\uparrow} = 0.1$ and $T^{\mathrm{bottom}}_{\downarrow\downarrow} = 0.9$. Such values demonstrate that the current along the QSH edges is spin-polarized, although not completely because of the finite size of the ribbon. Calculations for a (7, 4) ribbon give us $T^{\mathrm{top}}_{\uparrow\uparrow} = 0.85$, $T^{\mathrm{top}}_{\downarrow\downarrow} = 0.15$, $T^{\mathrm{bottom}}_{\uparrow\uparrow} = 0.15$ and $T^{\mathrm{bottom}}_{\downarrow\downarrow} = 0.85$.

We now switch on the magnetic interaction between a $S = 1$ local spin and a (11, 6) ribbon. In general we place the impurity at the centre of the edge and choose a coupling parameter, t_I, and an onsite energy, ε_I, to ensure that the density of states localized at the impurity site, $\rho_I(E)$, is approximately constant for energies, E, around the Fermi level (this ensures the convergence of the perturbation scheme [64]). The exchange coupling, J_{sd}, is chosen so that the perturbation parameter, $\rho_I J_{\mathrm{sd}}$, is approximately 0.1. These conditions are satisfied for: $\varepsilon_I = J_{\mathrm{sd}} = t_1/2$ and $t_I = t_1/4$. The spin degeneracy is lifted by an axial anisotropy $D = -10^{-3}\, t_1$, which corresponds to $D = -2.0$ meV, if the nearest neighbour hopping in the ribbon is fixed at a reasonable value of $t_1 = 2$ eV ($k_{\mathrm{B}}T = 0.05$). The uniaxial anisotropy gives us a degenerate ground state with the two spin states $|-1\rangle$ and $|+1\rangle$ separated from the first excited state $|0\rangle$ by $|D|$. As a result we do not expect a Kondo-like behaviour since no allowed transition between the degenerate ground state may occur (allowed transitions occur for $\Delta m = \pm 1$). The second order perturbation expansion is then well justified. The values $t_\eta = 4t_{\eta\mathrm{SC}} = t_1$ ensure that the spin system remains in equilibrium, i.e., in its ground state, throughout the spin-scattering process.

Figure 5.2 shows the calculated conductance spectra, $G(V)$, normalised to the $V = 0$ conductance, G_{el}, for three values of the parameter governing the QSH state, t_2. For $t_2 = 0$ there are no topologically protected edges and we observe the characteristic inelastic conductance step at a voltage $V = D/e$, when the transition from the ground state to $|0\rangle$ becomes possible (e is the electron charge). However, as t_2 is increased and we enter into the topological phase, we reveal a suppression of the inelastic contribution to the conductance, with an almost full suppression at the maximum value of $t_2 = t_1/3$. This can be understood as follows: at a positive bias, the right-going current is up spin-polarized. This means that the $|-1\rangle \to |0\rangle$ transition scatters out spin-down electrons. These cannot propagate towards the right electrode since there is no right-moving spin-down state in the upper edge and, as a consequence, they are completely reflected. Hence, as spin-flip events can only lead to backscattered electrons, the inelastic channel does not contribute to the current. Note that the residual conductance increase in Fig. 5.2 for $t_2 = t_1/3$ is simply due to the finite size of the ribbon.

We now investigate the possibility of manipulating the impurity spin direction using the QSH current. This is achieved by increasing the overall conductance, i.e., by increasing the average current density. When one works with a scanning tunneling microscopy setup bringing the tip closer to the impurity [62] does the job, while here our control parameter is the electronic coupling between the leads and the ribbon, $t_{\eta\mathrm{SC}}$. As such all the calculations that follow have been performed with $t_{\eta\mathrm{SC}} = t_1$.

The calculated populations of the various spin states are plotted as a

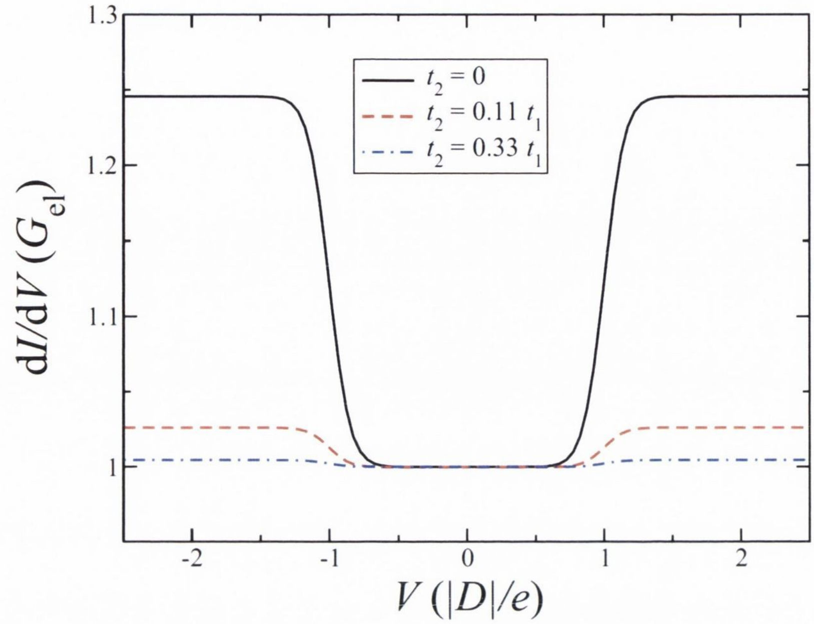

Figure 5.2: Spin-polarized IETS conductance spectrum for a TI (11, 6) ribbon with a $S = 1$ magnetic impurity attached at the upper edge. Note that the conductance step at the voltage characteristic of the inelastic excitation gets suppressed as the t_2 parameter is increased, i.e., as the ribbon is brought well inside the topological region of the phase diagram.

function of bias in Fig. 5.3(a) for both a (11, 6) and a (7, 4) ribbon. A $S = 1$ spin in a uniaxial anisotropy field and in thermal equilibrium with an electron bath presents an equal probability to occupy the $|+1\rangle$ and the $|-1\rangle$ states, i.e., for $V = 0$ one has $P_{+1} = P_{-1} = 1/2$. As soon as the bias is increased at and above $|D|/e$, excitations to the $|0\rangle$ state become possible due to spin-flip back-scattering. In this case however the current is intense, so that in between two scattering events the impurity spin does not have the time to relax back to the degenerate ground state. This means that now a spin-up electron (the majority specie in the upper edge right-going channel) can also induce the transition $|0\rangle \to |+1\rangle$. The consequence is that the electronic current flowing at the upper edge, in virtue of its spin polarization and its intensity, produces a net flow of population between the two degenerate ground state, i.e., for $V > +|D|/e$ one has $P_{+1} > P_{-1}$. In

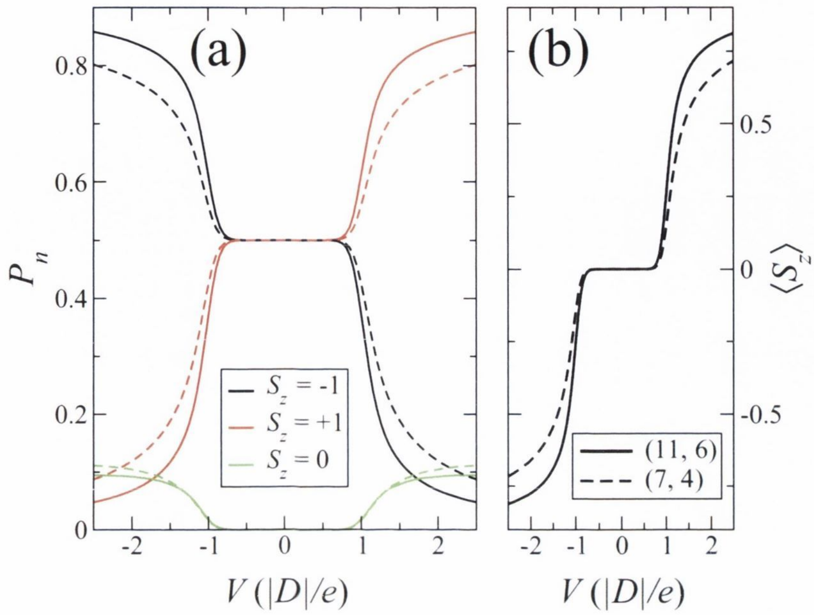

Figure 5.3: (a) Non-equilibrium population as a function of bias of the $S = 1$ impurity spin states for a (7, 4) (dashed lines) and a (11, 6) ribbon (solid lines). In panel (b) we show the average magnetization of the impurity for the same ribbons.

other words the impurity spin is driven by the current away from its uniaxial anisotropy axis. This can be fully appreciated by looking at Fig 5.3(b), where we show the average magnetization $\langle S^z \rangle = \sum_m P_m S^z_m$ as a function of bias. Such spin-pumping is essentially identical to what happens for spin-polarized tips [71] except that now one does not need either a magnetic electrode or an external magnetic field. Note that at a negative bias the effect is reversed, i.e., for $V < -|D|/e$ one has $P_{-1} > P_{+1}$, and that placing the impurity on the lower edge is equivalent to reversing the bias polarity.

The effects of the spin-pumping on the shape of the conductance spectrum are finally presented in Fig. 5.4. This time the $G(V)$ trace presents a step at the voltage corresponding to the $|\pm 1\rangle \rightarrow |0\rangle$ transition, i.e., the electron transport becomes sensitive to spin-flipping events. Such an appearance of the conductance step signals the suppression of the topological helical states induced by the transverse magnetization of the spin impurity [72]. Intrigu-

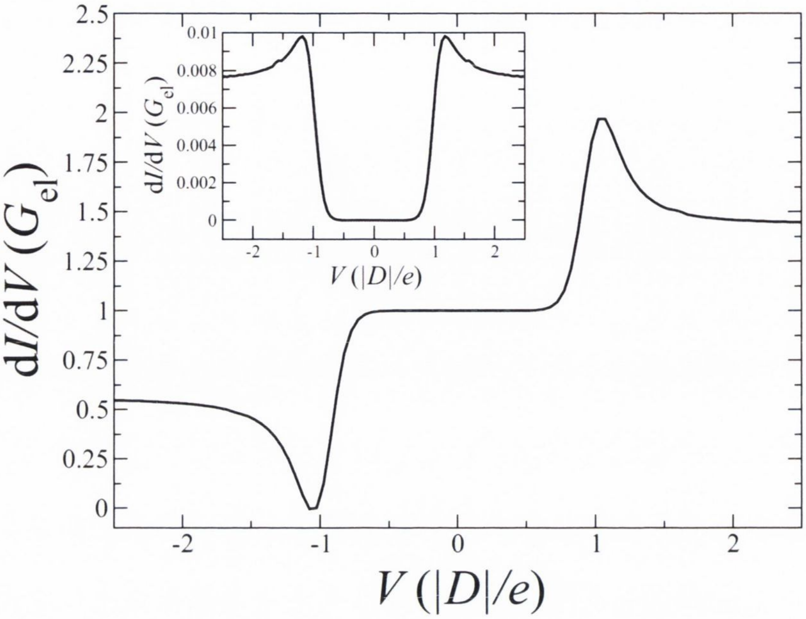

Figure 5.4: Spin-polarized IETS conductance spectrum for a TI (11, 6) ribbon with a $S = 1$ magnetic impurity attached at the upper edge. In this case the current is intense and drives the impurity spin away from the uniaxial anisotropy axis. Notably now there is a step in the differential conductance at the voltage corresponding to the inelastic transition $|\pm 1\rangle \to |0\rangle$. The magnitude and sign of such step depends on the bias polarity. In the inset the inelastic contribution to the conductance.

ingly, the magnitude and sign of the conductance step depends on the bias polarity. In particular we note that there is an inelastic contribution, which is symmetric with respect to the sign of V, and always contributes to enhance the conductivity. In contrast the elastic contribution is anti-symmetric with respect to the bias polarity, i.e., the elastic current increases for $V > |D|/e$ and decreases for $V < -|D|/e$. Placing the impurity on the opposite edge yields a mirror symmetric situation. This time the magnetization is driven toward $\langle S_z \rangle = -1$ ($\langle S_z \rangle = +1$) and the conductance decreases (increases) for a positive (negative) bias voltage. Overall we can summarize our results by noting that the sign of the change in the conductance trace at the onset voltage $|V| = |D|/e$ is proportional to $(\mathbf{v} \times \sigma) \cdot \langle \mathbf{S} \rangle$, where $\mathbf{v}$ is the group velocity of the edge state. In other words the anti-symmetry of the conductance is related to the helicity of the edge state, $\mathbf{v} \times \sigma$.

When one looks at the perturbative expansion of the conductance it can be realized that the term giving rise to the bias asymmetry is the magnetoresistive elastic term of the s-d Hamiltonian. Its contribution to the self-energy reads

$$[\Sigma^{\gtrless}_{\mathrm{mag-elas}}(E)]^{(2)} \propto -J_{sd}^2 \sum_{mn} G_0^{\gtrless}(E \pm \Omega_{mn})\delta_{mn} P_n S^z_{mn}, \tag{5.6}$$

where $G_0^{\gtrless}$ is the electronic Green's function, Ω_{mn} the energy difference between the two spin states $|n\rangle$ and $|m\rangle$ and $S_{mn} = \langle m|S_z|n\rangle$ is the spin transition matrix element. Since the terms includes δ_{mn} there is only an elastic contribution ($\Omega_{nn} = 0$), which involves no spin-flip events [66]. Such a term is proportional to S^z_{nn} and thus reverts its sign as the direction of impurity spin is reversed.

Note that the elastic and inelastic contributions to the conductance are calculated by partitioning the current into two parts, obtained respectively from the elastic and inelastic energy-dependent self-energies. These, however, are evaluated from the same self-consistent electronic Green's function, meaning that the elastic and inelastic contributions are not completely disentangled. As such, it should not be surprising that the on-set of inelastic scattering is evident also in the elastic contribution to the conductance.

Finally we investigate how the conductance profile changes as we increase the value of the total spin S of the magnetic impurity. This is done by rescaling the anisotropy parameter D and the electron-spin coupling strength J_{sd}, respectively, to $D/|S|$ and $J_{\mathrm{sd}}/|S|$, so that the effective interaction strength and the total spin anisotropy do not change in the comparison. Our results are plotted in Fig. 5.5. The figure reveals that, as the total spin increases, the height of the differential conductance steps gets larger. In the figure we also plot the average magnetization as a function of bias, which indicates that the

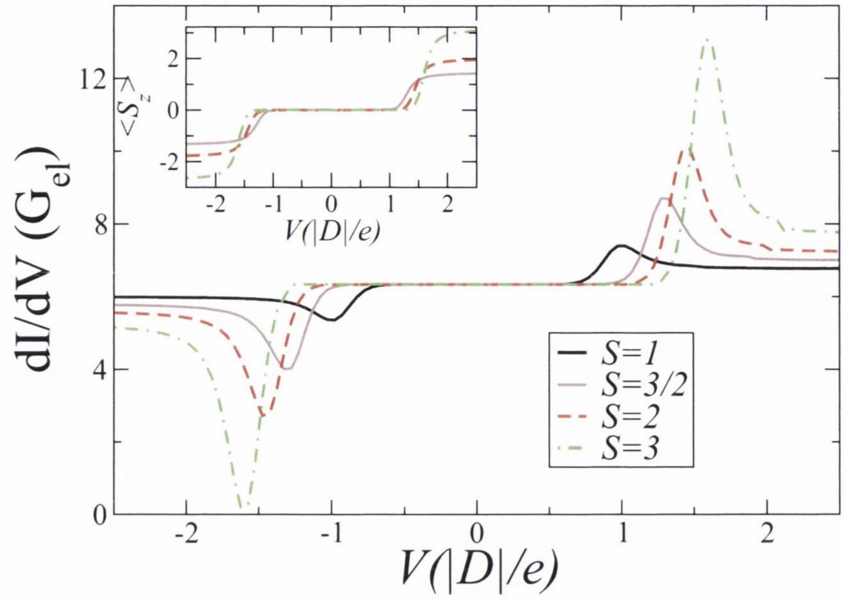

Figure 5.5: Spin-polarized IETS conductance spectrum for a TI (11, 6) ribbon incorporating a magnetic impurity with various spin ($S = 1, 3/2, 2, 3$) attached at the upper edge, in the intense current regime. The step in the differential conductance increases in magnitude with increasing the spin value of the adatom. Note that the spectra have been aligned vertically for clarity in comparison. The inset shows the average magnetization of the impurity for different values of S. Note that spin pumping persists for the larger values of the impurity spin.

spin pumping is present for larger values of S and that for voltages exceeding the energy of the inelastic transition the average value of S_z approaches its maximum value.

5.1.3 Gate controlled spin pumping

In this section we extend the concept discussed previously and propose a device where the transition between the two regimes is also achieved electrically, by gating the region at the boundary between the QSH insulator and the source/drain electrodes. As such we will show that the QSH state can be coupled with SF-IETS to probe and manipulate single magnetic atoms without the need of a magnetic field or a spin-polarized scanning tunneling microscope tip.

In the presence of a gate electrode the electronic Hamiltonian takes the

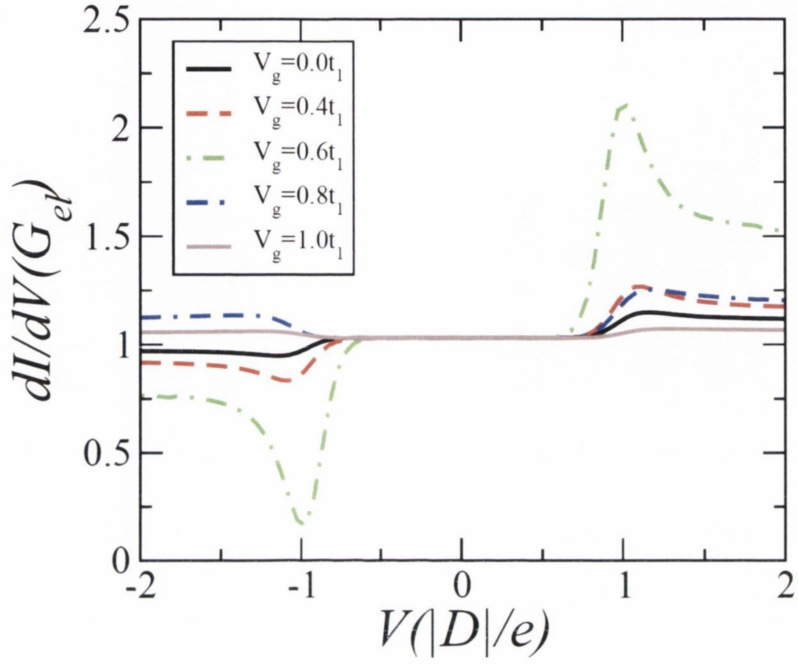

Figure 5.6: Normalized conductance trace as a function of the source/drain voltage at different values of the applied gate voltage for a $S = 1$ impurity spin. Note that increasing the gate voltage beyond $V_g = 0.6t_1$ allows us to crossover to a regime where the current is reduced to a point at which the conductance steps are suppressed. The curves have been aligned vertically for ease of comparison.

form

$$H_{\text{el}} = H_{\text{KM}} + V_g \sum_{i \in \text{ gate},\, \alpha} c^\dagger_{i\alpha} c_{i\alpha} + \varepsilon_I \sum_{\alpha} c^\dagger_{I\alpha} c_{I\alpha} + t_I \sum_{\langle Ii \rangle,\, \alpha} c^\dagger_{I\alpha} c_{i\alpha}\,, \tag{5.7}$$

where in addition to the Kane-Mele Hamiltonian, H_{KM}, we have the gate potential V_g, which is included via an additional on-site energy for the atoms in the gate region at the two ends of the ribbon as shown in Fig. 5.1.

We plot the conductance spectra (normalized to its $V = 0$ value, G_{el}) at different values of the gate voltage, V_g, in Fig. 5.6. For the calculations we set $t_\eta = t_{\eta\,\text{SC}} = t_1$ and $t_2 = 0.1t_1$ (t_η is the hopping parameter in the electrodes and $t_{\eta\,\text{SC}}$ is the coupling between the electrodes and the scattering region). These parameters keep the ribbon in the topological phase and

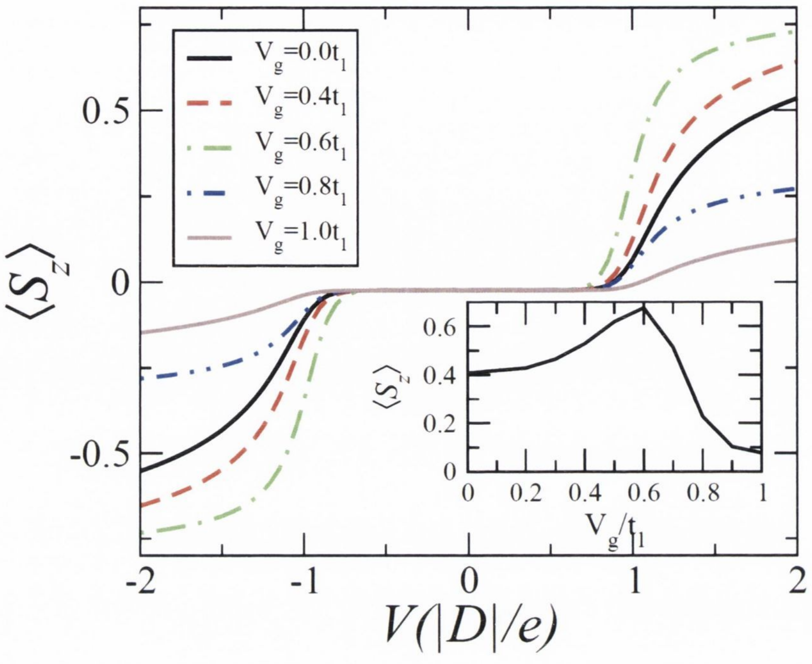

Figure 5.7: Average magnetization, along the direction perpendicular to the ribbon plane, as a function of bias voltage. Curves at different voltages are plotted showing gate control over the magnetization of the impurity spin. In the inset we report the magnetization as a function of gate voltage for a source/drain voltage of $V = 1.5\ |D|/e$.

the coupling between the leads and the scattering region is fixed to a large value. The choice of parameters, $\varepsilon_I = J_{\mathrm{sd}} = t_1/2$ and $t_I = t_1/4$, guarantees that perturbation theory can be used for the spin $S = 1$, as we discussed in the previous section. The spin degeneracy is lifted by introducing an axial anisotropy $D = -10^{-3}t_1$. This is equivalent to a temperature of around 12 K (assuming a realistic value of $t_1 = 1$ eV). In general, devices based on single atom anisotropies are low temperature devices expected to work around few tens of kelvin [61, 62].

At $V_g = 0$, i.e., when no gate voltage is applied, there is a conductance step seen at the energy corresponding to the first spin excitation of the system. This is the $|+1\rangle \rightarrow |0\rangle$ ($|-1\rangle \rightarrow |0\rangle$) spin transition for positive (negative) source/drain voltage, where $|S_z\rangle$ is the adatom spin's third component, familiar to us from the analysis in the previous section. Such transition is detectable because the electrode-ribbon coupling strength is large and the current is intense. As we increase the gate voltage we observe an enhancement in the intensity of the conductance step. This continues until V_g reaches a value of $0.6t_1$. Beyond such critical gate voltage there is a drop in the conductance step at $V_g = 0.8t_1$ and the inelastic conductance becomes suppressed. This suppression continues for higher values of the gate voltage.

These observations can be readily understood in terms of the changing interface resistance between the ribbon and the electrodes. At low values of V_g, there is a large current flowing from the leads to the ribbon and thus interacting with the magnetic adatom. For $V = 0$ the spin on the adatom is in an equal superposition of $|+1\rangle$ and $|-1\rangle$ states. As the bias reaches $|D|/e$ the excitation to the $|0\rangle$ state is possible by spin-flip of the incoming electron. Since the current is large the impurity spin S is not allowed to relax back to the ground state and thus the incident electrons can also induce transitions from $|0\rangle$ to $|+1\rangle$ and so be transmitted without getting backscattered. In the case of high interface resistance as engineered by increasing the gate voltage, there is a strong suppression of the conductance steps. In this scenario since the current density is small, the impurity spin can relax back to the ground state after the spin-flip event. This means that the incident right-going electrons, which are up spin polarized at the upper edge, will always encounter the impurity spin in either the $|+1\rangle$ or the $|-1\rangle$ state. A spin-flip event will reverse the electron's spin and since there are no down spin channels going right at the upper edge, the electron will be backscattered. Thus, the helicity of the QSH edge states leads to a suppression of the inelastic conductance steps at low currents [72].

Finally in Fig. 5.7 we plot the average magnetization of the device at different gate voltages. If no gate voltage is applied, then a change from zero to a finite magnetization occurs at $V = \pm|D|/e$, corresponding to the allowed spin excitation. Note that the direction of magnetization is opposite for opposite bias directions. As we now increase the gate voltage, the net magnetization increases, tending towards unity. This continues until $V_g = 0.6t_1$ beyond which it drops rapidly. For higher values of V_g the system remains closer to zero magnetization indicating the absence of spin pumping. The inset of Fig. 5.7 traces the magnetization at $V = 1.5\ |D|/e$ as a function of the gate voltage. Note that the magnetization is always less than ±1, due to finite size of the QSH ribbon.

5.1.4 Summary and Conclusions

In conclusion, we have demonstrated that a QSH current flowing at the edge of a $\mathbb{Z}_2$ TI can be used to manipulate the spin of a magnetic impurity. This does not require either an external magnetic field or magnetic electrodes, i.e., it allows one to implement spintronics without magnetism. Importantly the fingerprint of the manipulation can be found in the conductance profile themselves, making SF-IETS a tool for preparing, manipulating and reading a quantum spin in the solid state. We have also proposed a four-terminal device, which is designed to manipulate, by all electrical means, the spin of a magnetic adatom positioned at the quantum spin Hall edge.

Chapter 6

First principles transport study of topological suface states scattering

The first three-dimensional topological insulator to be experimentally realized was a Bi-Sb alloy [11], following a theoretical prediction by Fu and Kane [12]. The topological nature of the alloy is inherited from the parent element antimony, which has a non-trivial principal topological invariant ν_0, whereas bismuth has a trivial $\mathbb{Z}_2$ invariant [13]. Although Sb itself is a semimetal, its (111) surface hosts two spin-polarized bands, which extend around the Fermi energy. These form a single distorted Dirac cone where the lower bands are lifted upwards. The first section of this chapter is devoted to the study of these surface states employing density functional theory based transport methods. In particular we study the transmission of these states across surface barriers and compare to recent angle-resolved photoemission spectroscopy (ARPES) and scanning tunneling microscopy (STM) experiments.

In 2009, concurrent theoretical [14] and experimental [15] works revealed the topological insulator phase in Bi_2Se_3. Due to a simple single Dirac cone surface band structure and a relatively large bulk band gap of 0.3 eV, Bi_2Se_3 has emerged as the prototypical topological insulator material. Since many fundamental properties of topological states have been demonstrated in this material, it has been called the hydrogen atom of topological insulators [74, 3]. In the second section of this chapter we study the effect of barriers on the scattering properties of $Bi_2Se_3(111)$ surface states by means of large scale *ab initio* transport simulations.

6.1 Topological surface states scattering in Antimony

In a recent experiment, Seo *et al.* demonstrated that the topological surface states are extraordinarily insensitive to the presence of surface barriers [17]. They probed the extended nature of Sb(111) surface states by using a scanning tunneling microscope and found that these transmit across surface atomic steps with a high probability. Their analysis of the standing-wave states on surface terraces revealed the novel chiral spin texture of the two surface states, consistent with earlier ARPES measurements [75]. In this section we seek to theoretically recreate the above mentioned experiment by using *ab initio* transport theory, and show that we can reproduce the formation of quantum well states and their life-times, as well as the wave lengths and phase shifts of the scattering states. Thereby we demonstrate that one can describe the correct scattering properties of such topologically protected surface states by first-principles calculations. In addition of comparing our results favorably to experiments, we predict the scattering properties of these states in presence of a surface perturbation along a direction orthogonal to the one probed experimentally.

6.1.1 Computational Details

Our first-principles electronic structure calculations are performed with density functional theory (DFT) using the local density approximation (LDA) to the exchange-correlation functional. We employed the SIESTA package, which implements a linear combination of atomic orbitals basis set [76]. Spin orbit interaction, essential to describe the surface states, has been included via the on-site approximation [38] as discussed in Chapter 3. We include Sb $5s$ and $5p$ as the valence electrons. In the slab geometry, there is a 10 Å thick vacuum region in the supercell, to avoid interaction between periodic images. The transport properties are then calculated by using SMEAGOL, which combines the non-equilibrium Green's function (NEGF) method with DFT [77, 78, 79]. In SMEAGOL the scattering region is attached to one or more semi-infinite electrodes via self-energies. The charge density is calculated by integrating the non-equilibrium Green's function, along a contour in the complex energy plane. For this we use, 16 energy points on the complex semicircle, 16 points along the line parallel to the real axis and 16 poles. Periodic boundary conditions are employed in the direction orthogonal to the transport direction, while using open boundary conditions along the transport direction allows us to simulate single scatterers [80]. We use an equivalent temperature of 300 K for broadening the Fermi distribution. Our order-N implementation of SMEAGOL allows us to treat large systems [80]. We use a double-ζ polarized (DZP) basis set, with a cutoff energy of 300 Ry for the real space mesh. We have carefully checked convergence of our results with respect to all the parameters used.

Sb crystallizes in a rhombohedral structure with two atoms per unit cell. An alternate way to represent its structure is in a hexagonal setting with the unit cell comprising six atoms. This representation is particularly useful to construct two-dimensional slabs, which are made of Sb bilayers, as shown in Fig. 6.1(a). The inter-bilayer coupling is weak and it is possible to create surface steps, which are a single bilayer high [17, 86]. The bulk structure was relaxed using the Vienna Ab initio Simulation Package (VASP) [81], until the forces were less than 0.01 eV/Å.

6.1.2 Results

We begin by calculating the surface band structure of six and twelve bilayers thick slabs of Sb [Figs. 6.1(b) and (c)], by using a 10 × 10 in-plane k-point grid. The distorted Dirac cone at $\bar{\Gamma}$ is gapless indicating minimal interaction between the top and bottom surfaces of the slab. The surface band structure matches well previous *ab initio* calculations [82, 83, 84, 85]. We find the Dirac point at an energy of about 210 meV below E_F for six and twelve bilayer slabs. In order to simulate the ARPES spectrum of an infinitely thick slab we perform a SMEAGOL calculation for the 6 bilayer slab, where we attach semi-infinite Sb electrodes at the bottom layer via self-energies. The ARPES spectrum is then obtained by calculating the projected density of states on the surface atoms, and the result is shown in Fig. 6.1(d). The spin-resolved ARPES [Fig. 6.1(e) and (f)] shows that the two surface bands carry opposite spin and exhibit the characteristic spin texture associated with topologically non-trivial materials. Furthermore, it can be seen that the surface states are more pronounced close to the $\bar{\Gamma}$ point. Once the two bands turn downwards from their maximum point, they are less localized on the surface due to their hybridization with the bulk bands. This matches with ARPES experiments, where at $\bar{M}$, no surface states are found [75]. Thus, in both scattering and ARPES experiments, one would expect the dominant contributions to come from an area around the center of the BZ, with a radius of about one third of the length of BZ along $\bar{\Gamma} - \bar{M}$ direction. We note that the good agreement with the ARPES experiments shows that the LDA exchange-correlation functional is appropriate for this system.

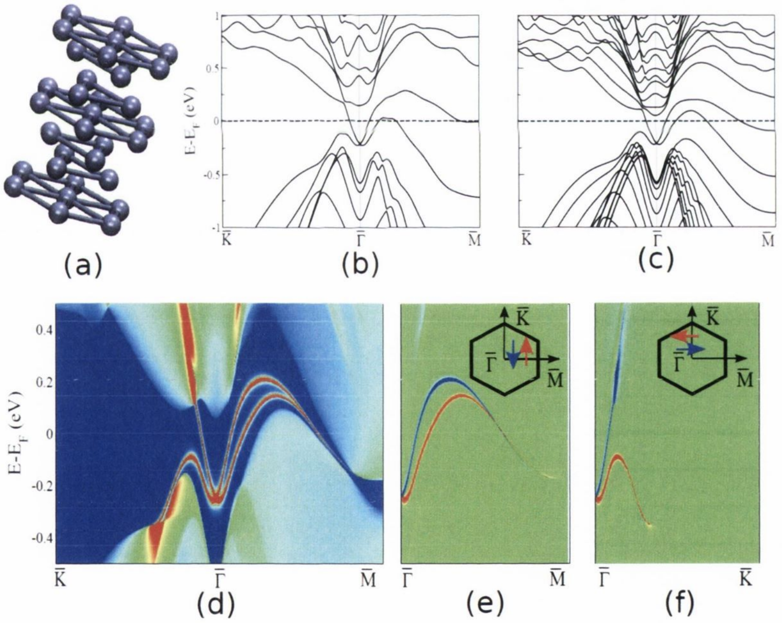

Figure 6.1: (a) Structure of antimony in the hexagonal setting. The atoms form a bilayer structure with the intralayer distance as 1.51 Å and the interlayer distance as 2.25 Å. Band structure for (b) six bilayers and (c) twelve bilayers thick slabs along $\bar{K} - \bar{\Gamma} - \bar{M}$ directions. (d) Simulated ARPES from a semi-infinite slab. Here and henceforth warmer colors represent higher PDOS (red represents largest values, blue lowest ones, with the color scale in between being linear). Spin-resolved ARPES along (e) $\bar{\Gamma} - \bar{M}$ and (f) $\bar{\Gamma} - \bar{K}$ directions showing the opposite spins of the two surface bands along the directions indicated by arrows in the inset of the figures. In this case, red and blue colors indicate up and down spins, respectively.

Next we simulate a step perturbation on the surface for two different directions: In the first case the step runs along the $\bar{\Gamma}-\bar{M}$, which is the same as in the experiment in Ref. [17]; and as a second orientation we choose the orthogonal direction ($\bar{\Gamma}-\bar{K}$ direction), to evaluate the effect of the orientation on the scattering. We have relaxed the step geometry for a smaller scattering region, but the atomic displacements were only minor, and henceforth we use the unrelaxed step configuration. A single bilayer high step is created over a length of 120 Å. The adjacent flat region extends over 270 Å. The setup consists of a 13 bilayer-thick region with a short 12 bilayer-thick region on the left and a longer one on the right. We attach semi-infinite leads on left-hand and right-hand sides of the scattering region, by means of the self-energies calculated by SMEAGOL. The total projected density of states (PDOS) $\mathcal{N}_{\text{total}}$ is obtained by integrating over all $k_\perp$-points perpendicular to the transport direction

$$\mathcal{N}_{\text{total}}(E) = \int_{k_\perp} \mathcal{N}_{k_\perp}(E)\, dk_\perp. \tag{6.1}$$

Analogously the total transmission is given by

$$T_{\text{total}}(E) = \int_{k_\perp} T_{k_\perp}(E) dk_\perp. \tag{6.2}$$

We note that in the first orientation of the step $k_\perp$ runs along the $\bar{\Gamma}-\bar{K}$ direction and the transport direction is parallel to $\bar{\Gamma}-\bar{M}$ in reciprocal space, whereas in the second orientation $k_\perp$ runs along $\bar{\Gamma}-\bar{M}$ and the transport direction is parallel to $\bar{\Gamma}-\bar{K}$. While we find that 3 $k_\perp$-points are sufficient for obtaining a converged self-consistent potential, we need many more $k_\perp$-points for accurately integrating $\mathcal{N}_{\text{total}}$ for a given potential, where we therefore use 200 $k_\perp$-points. The $\mathcal{N}_{k_\perp}$ of the atoms on the top surface for $k_\perp = 0$ is shown in Fig. 6.2(a). The quantum well states formed by quantization of the energy levels in the step region are clearly visible, and extend over the energy window in which the two topological surface bands exist. The PDOS on the adjacent flat region shows oscillatory behavior typical of one-dimensional scattering barriers [80], and it has phase shifts at energies corresponding to the allowed energy states in the step region. At those energies we also find resonant transmission across quantum well states, visible as peaks in the transmission curve in Fig 6.2(b). This matches the experimental observation of resonant tunneling through the surface barrier at those energies. It indicates a remarkably long phase coherence length of hundreds of angstroms, which is due to the extended nature of topological surface states [17]. Further, the change of phase when the states are reflected from the barrier is nearly zero. Over the entire energy range there is clearly a rather large amount of scattering caused by the step and the transmission drops significantly below the value in absence of step. We have verified that the single bilayer step at the top surface perturbs the bottom layer minimally and there is only small coupling between the two surfaces even in the presence of the surface step.

The integrated $\mathcal{N}_{\text{total}}$ is shown in Fig. 6.2(c). The main features corresponding to the quantized energy levels can still be identified at almost the same energies found for $k_\perp = 0$, but are broadened and less pronounced. The broadening of energy levels for $k_\perp = 0$ is 8-12 meV, while for the total it increases by a factor of about three. In experiment, these were found to lie between 20-45 meV [17]. Hence, the states lifetimes, which are inversely proportional to their broadening, agree quantitatively with those found experimentally. This shows that the scattering properties of the step are well-reproduced in our calculations. We note that quantitatively the results for a 12 bilayer slab differ somewhat from the ones one would obtain for a semi-infinite surface due to the different surface band structures [Fig.6.1(c) vs. 6.1(d)]. Firstly, the linear dispersion region of the surface states around Γ is more extended in energy for the semi-infinite surface, and this results in quantum well states spacing remaining constant, whereas for the 12 bilayer slab the spacing reduces with increasing energy. Moreover for 12 bilayers we find band edges at -185 meV and -108 meV, which are absent in the semi-infinite system, and which give strong contributions to the 12 bilayer PDOS. Due to the enhanced PDOS at these band edges the phase shifts corresponding to resonant tunneling are not as clearly pronounced for $\mathcal{N}_{\text{total}}$ as for $k_\perp = 0$. Finally, whereas for the semi-infinite slab there are only two discrete surface bands around E_F, and all the other bands are diffuse, for the 12 bilayer slab clearly the number of distinct bands is larger, which as we will show leads to many more features in the scattering. These lead to discrete short-wavelength scattering processes which would be absent for a semi-infinite slab.

In order to analyze the scattering mechanism and probe the spin texture of the surface bands, we evaluate the Fourier transform (FT) of $\mathcal{N}_{\text{total}}$ along the flat region on the right side of the step, and the result is shown in Fig. 6.2(d). For a given energy and $k_\perp$ ($k_\perp$ is conserved during scattering) there are standing waves with a wave vector q for every pair of scattering states in the Sb electrodes with opposite group velocities. For each such pair of states with indices i and j we get the norm of scattering vector $q_{ij} = |k_i - k_j|$, at which, therefore, the FT has enhanced amplitude. In Fig. 6.2(d) we find a rather large amount of noise at low q, partly due to the fact that we integrate $\mathcal{N}_{\text{total}}$ over a finite number of $k_\perp$-points, nevertheless we can identify two prominent features that are preserved for increasing q. The first is an enhanced amplitude starting at about -210 meV and then increasing linearly with q

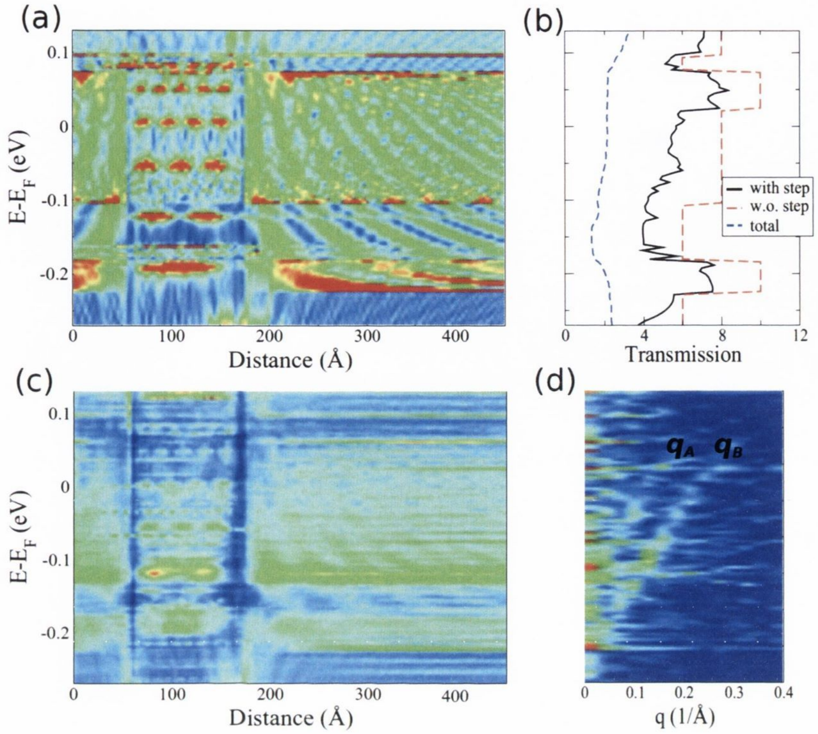

Figure 6.2: (a) PDOS for surface atoms with a single step adjacent to a flat region for the first setup at $k_\perp = 0$. (b) Transmission at $k_\perp = 0$ with and without the step indicating finite scattering due to the step. Average of transmission over all $k_\perp$-points is also shown. (c) PDOS for surface atoms averaged over all $k_\perp$. (d) Fourier transform of PDOS data in (c) over the flat region reveals the different allowed scattering wave vectors. The most prominent features, q_A and q_B, are nearly linear with slopes equal to 1.1 eVÅ.

with a slope of 1.1 eVÅ, and the second is an equivalent enhancement with the similar slope starting at -110 meV. These two prominent scattering wave-vectors are also found in the experiments of Seo *et al.*, where they are labeled q_B and q_A, respectively. q_B is attributed to scattering between the surface states close to $\bar{\Gamma}$ having the same spin, but opposite momentum direction. In this case the scattering state momenta are not equal, unlike in conventional scattering, because of the unique spin texture of the surface states resulting in an asymmetric band structure for a given spin. The other scattering wave-vector (q_A) is attributed to scattering between neighboring hole pockets away from $\bar{\Gamma}$. The calculated slopes of q_A and q_B are remarkably close to the value of 1.2 eVÅ found experimentally [17]. We note that to explain the origin of

both q_A and q_B, one needs to go beyond the one-dimensional model invoked by Seo *et al.* and a full two-dimensional treatment is required.
An STM experiment measures the total scattering in all the reciprocal space directions. In order to establish which $k_\perp$-points give rise to the q_A and q_B features in the average, we decompose the allowed scattering processes along different $k_\perp$ directions. To illustrate the general scattering mechanism, in Fig. 6.3(c) we show the Fourier transform for an arbitrary $k_\perp$-point, and the bands of the Sb electrodes along the transport direction for the same $k_\perp$. As an example, we consider the energy at -150 meV, where in the band structure we find 2 bands crossing for positive k, at k_1 and k_2. In the Fourier transform we find 3 scattering vectors: $q_1 = k_2 - k_1$, $q_2 = 2k_1$ (obtained by k_1 scattering to $-k_1$), and similarly $q_3 = 2k_2$. The amplitude is highest towards the band edge, where the PDOS is maximal. Analyzing the FT for all $k_\perp$-points, we find that most such features found for a single $k_\perp$ disappear when averaging, except for q_A and q_B. This shows that the scattering processes visible in STM experiments are only a small subset of all processes occuring. Therefore, no visible scattering from defects in an STM experiment does not imply perfect transmission, since the absence of standing wave patterns can also be due to the fact that the features may be broadened upon integration over $k_\perp$, even for substantial scattering for each single $k_\perp$.

There are two key factors, which decide which q vectors dominate. Firstly, for a given $k_\perp$ there needs to be a high scattering between the initial (k_i) and final (k_j) states. This is the case if the spins in the two states are aligned and if the surface-PDOS for them is large. This, therefore, excludes bulk states and states with opposite spins. Secondly, for the features to remain prominent when integrated over $k_\perp$, it is necessary that there is an extended region in the BZ where these features are found more or less unchanged. This is true when the change of band structure along $k_\perp$ is small, which is the case close to a maximum or a minimum, i.e. when $\partial E/\partial k_\perp = 0$, and ideally when the band curvature is small ($\partial^2 E/\partial k_\perp^2$ is small). We have verified that the above two conditions are indeed satisfied for q_A and q_B. From the 12 layer slab band structure along $\bar{\Gamma} - \bar{K}$ [Fig. 6.1(c)] we identify two such features: the first is the minimum at about $k_\perp = \bar{\Gamma}$, and the second is the maximum at $k_\perp b = 0.16\pi$. In Figs. 6.3(a) and (b) we show the scattering wave vectors for these two $k_\perp$. We clearly identify the features leading to q_A and q_B. The remaining features in the FT disappear under averaging, since for these the aforementioned conditions are not satisfied. We note that a related study has been recently performed by Takane and Imura by using a low energy Dirac theory, where they find perfect transmission at all incidence angles for a hyperbolic step [87]. However, as noted by the authors, their analysis is valid in the long wave length regime, while we focus on atomic-scale terraces. Our results clearly demonstrate that there is scattering between states on the same Dirac cone for $k_\perp \neq 0$, which leads to the appearance of the q_A scattering vector. The fact that such a scattering vector is found prominently also in experiments indicates that for non-normal incidence the states are not perfectly transmitted, in agreement with our findings.

Finally, we create a step on the Sb(111) surface along the x-direction. In this case the slab consists of six bilayers, since simulating a 12 bilayer scattering region along this direction is beyond our computational resources. This direction is promising since there is an energy window [-60 meV to 20 meV in Fig. 6.1(b)] over which only a single spin-polarized surface state exists for $k_\perp = 0$ (note that in this case the transport direction is parallel to the $\bar{\Gamma} - \bar{K}$ line in reciprocal space), which is reminiscent of the prototypical topological insulator Bi_2Se_3. The $\mathcal{N}_{k_\perp}$ of the surface atoms for $k_\perp = 0$ is

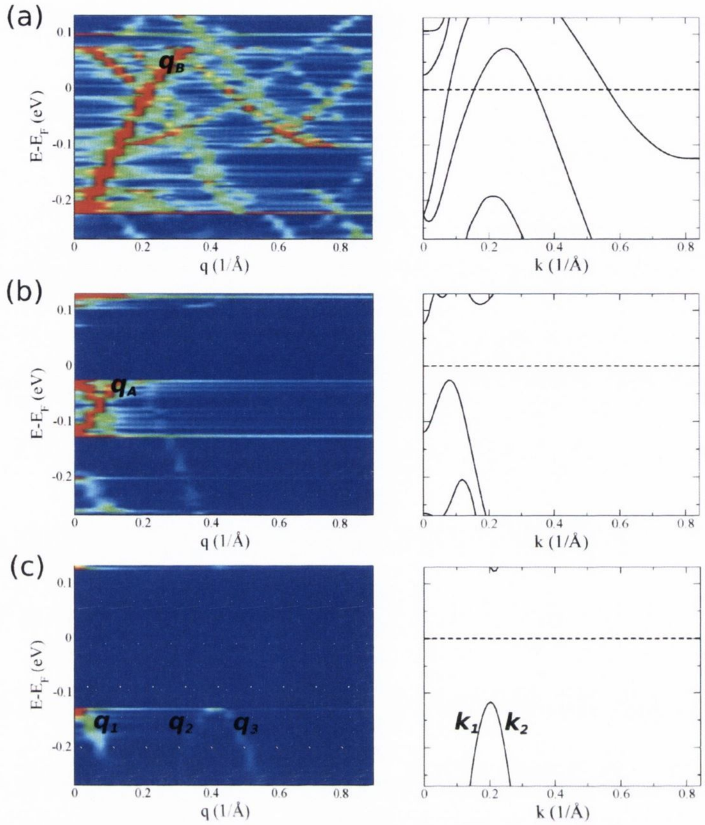

Figure 6.3: The allowed scattering wave-vectors obtained from the Fourier transform of PDOS data at (a) $k_\perp b = 0$, (b) $k_\perp b = 0.16\pi$ and (c) $k_\perp b = 0.50\pi$. The panels on the right show the corresponding band structures at the same $k_\perp$ for the 12 bilayer slab electrodes.

plotted in Fig. 6.4(a). In the energy range of a single spin-polarized state there is no scattering, which is the hallmark of a topological surface state. From -170 meV to 70 meV quantum well states are found as a result of superposition between the two surface bands, with a mechanism analogous to that in the first step orientation. Fig. 6.4(b) shows the transmission at $k_\perp = 0$ with and without the surface step. Remarkably, there is a perfect transmission in this energy window, despite the presence of the strong surface perturbation in the form of an extended single bilayer high surface step. This can be explained by invoking the general principle that disorder which does not break time reversal symmetry can not localize a single topologically protected surface state. Away from this energy region, there is substantial

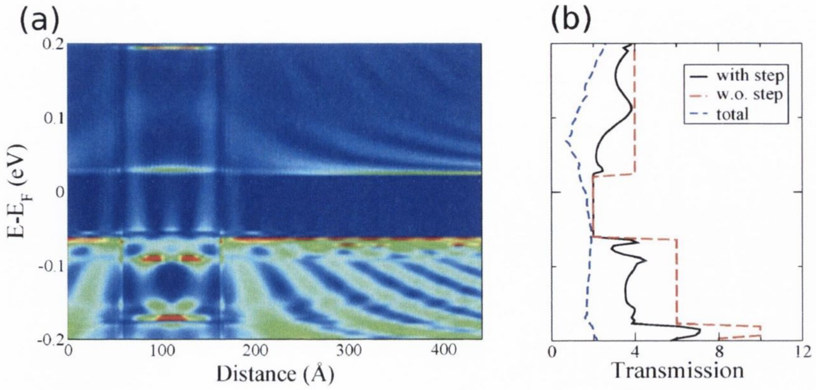

Figure 6.4: (a) PDOS at $k_\perp = 0$ for surface atoms with a single step adjacent to a flat region, with the step extending along the $\bar{\Gamma} - \bar{K}$ direction. There is an energy region from -60 to 20 meV with no scattering and hence no standing wave states. (b) Transmission at $k_\perp = 0$, indicating the perfect transmission around E_F even in presence of a surface barrier. Total transmission also shows minimal scattering in that energy range.

scattering caused by the step and the transmission drops down from the value in its absence. The total transmission averaged over all $k_\perp$-points is reduced for all energies, and one can expect that as the amount of disorder increases, the total transmission will be dominated by small $k_\perp$ contributions. We believe that these findings would provide a strong motivation for study of Sb surface with steps along $\bar{\Gamma} - \bar{K}$ direction.

6.1.3 Summary and Conclusions

In conclusion, we have performed an *ab initio* study of the topological surface states on the Sb(111) surface and their response to the presence of single bilayer high steps, showing excellent agreement with experimental observations. We have identified the various scattering processes possible and formulated general conditions that lead to the formation of the dominant scattering features. This enabled us to confirm the fascinating helical spin texture of the surface states. Resonant tunneling transmission across surface barriers, indicative of the extended nature of these states, was found. We identified phase shifts in the scattered PDOS at quantum well states energies and evaluated their life-times. The results demonstrate that it is possible to fully characterize the scattering properties of the barriers with first-principles calculations. Finally, we have shown that one can have minimal scattering along other high-symmetry directions even in presence of strong surface perturbations, which provides a unique signature for the topologically protected nature of these states. We believe that this finding can be readily tested in future experiments.

6.2 Ab initio transport across Bi_2Se_3 surface barriers

In recent years, there has been a rapid expansion in the number of STM experiments on $Bi_2Se_3(111)$ and the closely related $Bi_2Te_3(111)$ surface. Impurities on Bi_2Se_3 have been imaged and scattering mediated by bulk states has been observed [88, 89, 90, 91]. Furthermore, there have been studies of dopants on bismuth telluride surface [92, 93]. Interestingly a bound state at a surface step on Bi_2Te_3 has also been found [94]. On the theoretical front, there have been efforts to model scattering of these surface states from perturbations by employing Dirac-like model Hamiltonians and imposing symmetry considerations [95, 96, 97]. Furthermore, a study of the robustness of the surface states against on-site disorder by employing first-principles calculations was also reported [98]. In this section, we investigate the effect of step barriers on the $Bi_2Se_3(111)$ surface on the scattering properties of the topological states by means of *ab initio* transport calculations. We find that, due to the spin-polarized helical nature of the surface band, there is no scattering for normal incidence, since a reflection would entail a 180° backscattering. However, as one moves to non-normal incidence scattering is revealed. This is because the spins of the counter-propagating channels are no longer anti-parallel. An analysis of the local density of states reveals that the surface barrier strongly affects the spin of the surface state, in particular allowing an out of plane spin component, which is negligible in the absence of the barrier. We construct a potential barrier model for the surface step and solve it based on a simple Dirac Hamiltonian for the surface states. A comparison is then made with our first-principles calculations. We note in passing that, although our *ab initio* calculations have been performed in particular for Bi_2Se_3, we expect that the qualitative features found would also hold for step edges perpendicular to directions without hexagonal warping in Bi_2Te_3 and other related materials like Bi_2Te_2S and $TlBiSe_2$.

6.2.1 Computational Details

The transport calculations were performed using the SMEAGOL code including spin-orbit interaction, as described in Chapter 3. The generalized gradient approximation (GGA) to the exchange-correlation functional was employed. We have used a double-ζ polarized basis set and a real space mesh cutoff of 300 Rydberg. For slab calculations a minimum vacuum region of 25 Å has been included to prevent spurious interaction between periodic replicas. We use $3 \times 1 \times 1$ k-point mesh to obtain the self-consistent potential (here x is the direction perpendicular to the transport direction in the plane of the slab, y is along the slab height and z is the direction along transport). For calculating the integrated transmission and density of states we use 101 k-points along the x direction. Periodic boundary conditions have been considered in directions orthogonal to the transport direction, while using open boundary conditions along the transport direction allows us to simulate a single scatterer, which, in this particular case is a surface step.

6.2.2 Results

The unit cell for the leads used is shown in Fig. 6.5(a). It consists of a 3-QL thick slab terminated on both sides by Se atoms, as found experimentally. We use experimental lattice constants. The corresponding band structure is shown in Fig. 6.5(b). Note that there is band folding as a consequence of doubling the primitive Bi_2Se_3 unit cell. We find the Dirac cone and the helical states consistent with earlier studies [14]. It should also be noted that there is a small but finite gap (of the order of 0.01 eV) at the Γ point in the cone due to an interaction between the two surfaces of the slab. However, this does not affect our analysis of the topological states at higher energies, since the tunneling to the bottom surface is negligible.

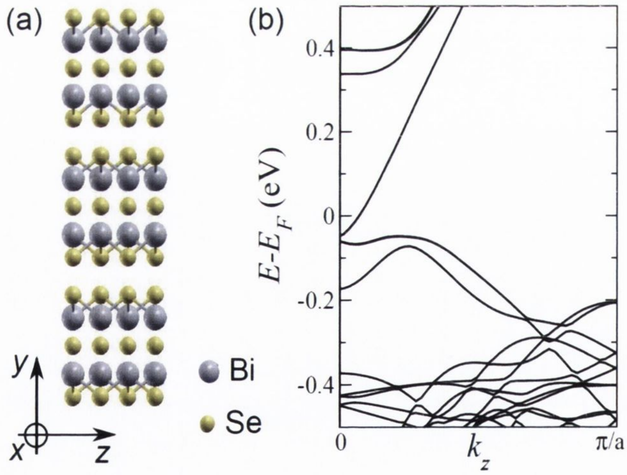

Figure 6.5: (a) Unit cell of the 3-QL slab leads used in the transport calculations. The yellow and purple spheres represent selenium and bismuth atoms, respectively. (b) The band structure along direction of transport (z) is shown at $k_x = 0$. The surface bands in the energy window of -0.05 to 0.30 eV have a helical spin texture.

The transport setup for single and double barrier scattering is shown in Fig. 6.6(a) and (b). We consider a single quintuple (QL) layer high barrier on a 3-QL thick slab. The step edge is extended along the $\Gamma - M$ direction and the transport is along the orthogonal $\Gamma - K$ direction of the primitive Brillouin zone of Bi_2Se_3. The scattering region has a length of 198.87 Å. For the single barrier case the 4-QL region extends over about half the length of the scattering region. For the double barrier setup we investigate two barrier lengths, where the step extends over a region of 49.72 Å in the shorter case and is 149.16 Å for the longer one.

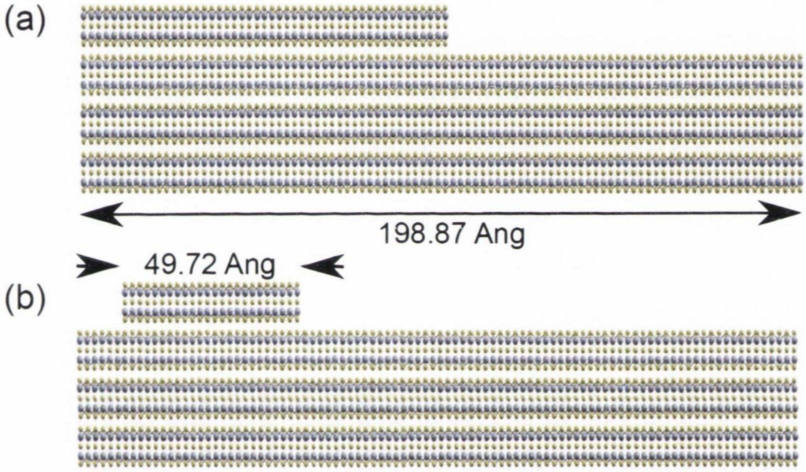

Figure 6.6: Transport setup for the scattering problem is shown for (a) single barrier and (b) double barrier. In both cases we add an extra single quintuple layer high barrier on the 3-QL thick slab. Note that same self-energies for semi-infinite 3-QL leads are attached on the left and right sides of the scattering region in (b), while different left and right electrodes corresponding to 4-QL and 3-QL slabs are needed in (b).

Scattering from a single barrier

We begin our analysis by looking at the transport across a single surface barrier [see Fig. 6.6(a)], for which the transmission function is shown in Fig. 6.7(a) as a function of energy and for different values of the x component of the wave-vector. At normal incidence ($k_x = 0$), the surface states are perfectly transmitted, $T = 2$, due to their helicity. As such, our first-principles calculations confirm Klein tunneling [99]. The transmission of bulk states, however, is reduced by the presence of the step edge. In contrast, as soon as one moves away from normal incidence, the transmission is no longer integer-valued. In particular it dips below $T = 2$, indicating substantial scattering. Note that the drop in transmission at $k_x = 0$ at $E - E_F = -0.05$ eV is merely due to the small gap in the band structure due to the finite thickness of the slab. Fig. 6.7(b) shows the total transmission obtained by integrating $T(E, k_x)$ over all angles of incidence, namely $T_{\text{total}} = \frac{1}{\Omega_{\text{BZ}}} \int_{k_x} T(E, k_x) dk_x$, where Ω_{BZ} is the length of the Brillouin zone. Notably T_{total} retains the characteristic "V-shape" associated with the linear Dirac cone-like bands, despite the presence of the barrier. Overall we can conclude that the total transmission in presence of the barrier is quite close to the one for the unperturbed slab [compare the red and black curves in Fig. 6.7(c)]. For comparison, we have also performed calculations for steps running along the $\Gamma - K$ direction (with transport along $\Gamma - M$). Since the hexagonal warping effect, particularly at energies close to the Dirac crossing, is quite small in Bi_2Se_3, we find results, which are very similar to the ones obtained for steps along the $\Gamma - M$ direction. Hence, in the rest of this section we focus our attention on the latter.

At non-normal incidence the spin projections of the surface states counter-propagating at a given edge are no longer anti-parallel and thus backscattering becomes allowed, even in the absence of a perturbation that breaks time-reversal symmetry. We note that, although spin-orbit coupling mixes the spin components, one can still define spin components along different directions by using a projection onto the three Pauli matrices $\{\sigma_x, \sigma_y, \sigma_z\}$ and the identity matrix I. The situation is schematically illustrated in Fig. 6.7(d), and its consequences are demonstrated in Fig. 6.7(c), where we plot the transmission across the surface barrier as a function of k_x at different energies. Clearly $T(E, k_x)$ is reduced as k_x increases, which is expected from argument related to the spin projections of the two counter-propagating surface states. At larger incidence angles the transmission tends towards the residual value of one, since a perfectly transmitted surface state is present at the opposite side of the slab (no scattering center is present on the opposite surface). If one increases k_x even further, the band edge for the Dirac cone at both surfaces is reached, and the transmission abruptly goes to zero. It can be shown that the maximum scattering amplitude is proportional to $\frac{1}{2}(1+\cos\theta)$, where θ is the angle between the spin directions of the counter-propagating surface states [100]. Note that at higher energies, the transmission persists at values around the unperturbed one, $T = 2$, for larger incidence angles. This is because as one moves the Fermi level at higher energy, the Fermi circle gets larger. Consequently, the same k_x corresponds to a smaller incidence angle.

In STM experiments, one measures the oscillations in the electron density in order to study the scattering arising from surface modifications, for example from surface steps as studied in Ref. [101]. A Fourier transform of the density yields the characteristic frequencies of its oscillations, i.e, gives the scattering wavevectors, $q = |k_{\mathrm{inc}} - k_{\mathrm{ref}}|$ (k_{inc} and k_{ref} are incident and reflected wavevectors, respectively). In Fig. 6.8 we plot the density of states projected (PDOS) onto the surface atoms along the scattering region. At $k_x = 0$ no oscillations in PDOS are seen after reflection from the step edge. However, moving away from normal incidence, the above-mentioned oscillations begin to appear. The scattering vectors can be obtained by performing a Fourier transform of the DOS along the long flat region adjacent to the barrier, in a manner analogous to Sb(111) case studied in the previous section. At $k_x = 0$, expectedly there are no prominent scattering processes. As one moves to $k_x = 0.032$ Å^{-1}, there appears a dominant scattering wavevector in the Fourier transform starting at 0.1 eV and extending upwards

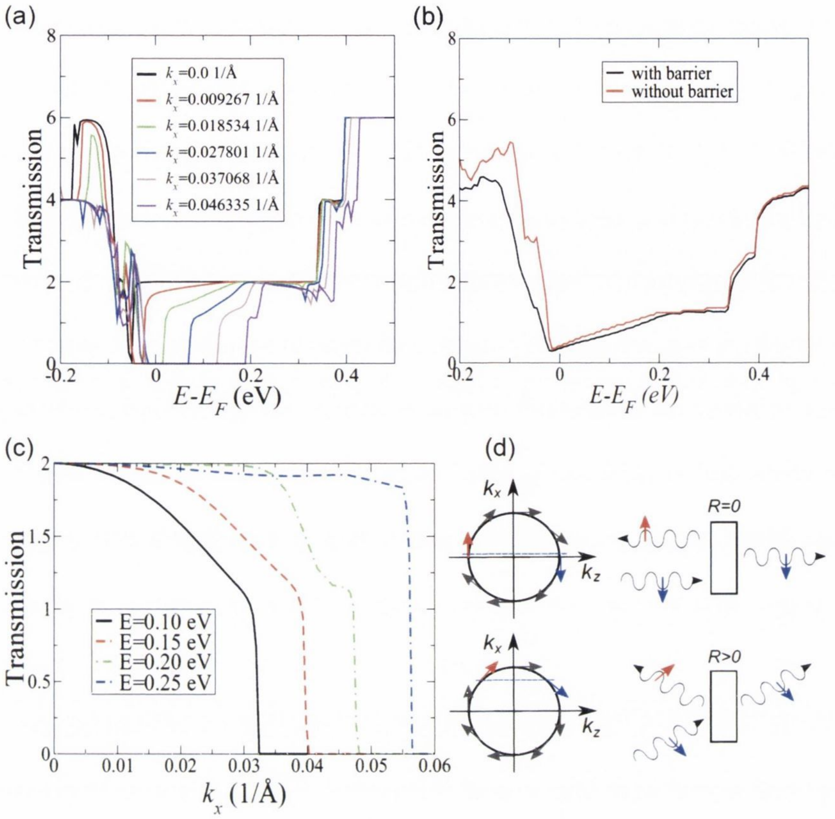

Figure 6.7: (a) Transmission across the surface barrier as a function of energy at different values of the x component of the wave-vector, orthogonal to the transport direction. Different curves correspond to different k_x. Note the perfect transmission at $k_x = 0$. At other incidence angles T is reduced. (b) The total transmission integrated over k_x in the presence (black curve) and absence (red curve) of the barrier. (c) The transmission as a function of k_x, at different constant energy cuts in the energy region of the surface states. Non-zero reflection at the barrier can be explained using the schematic diagram shown in (d).

in energy, as shown in Fig. 6.8(b). This corresponds to backscattering at a non-normal incidence angle. Furthermore, this can be mapped to band structure along the transport direction, where a band starting at the same energy is present. The average over k_x, however, reveals no scattering on this scale, even though there is a clear back scattering at individual k_x. In order to accurately resolve the small density oscillations above the average, one would need to consider many more k_x-points in the calculation. This is computationally prohibitively expensive for the system sizes considered here. For all three cases we also plot the transmission as a function of energy, for

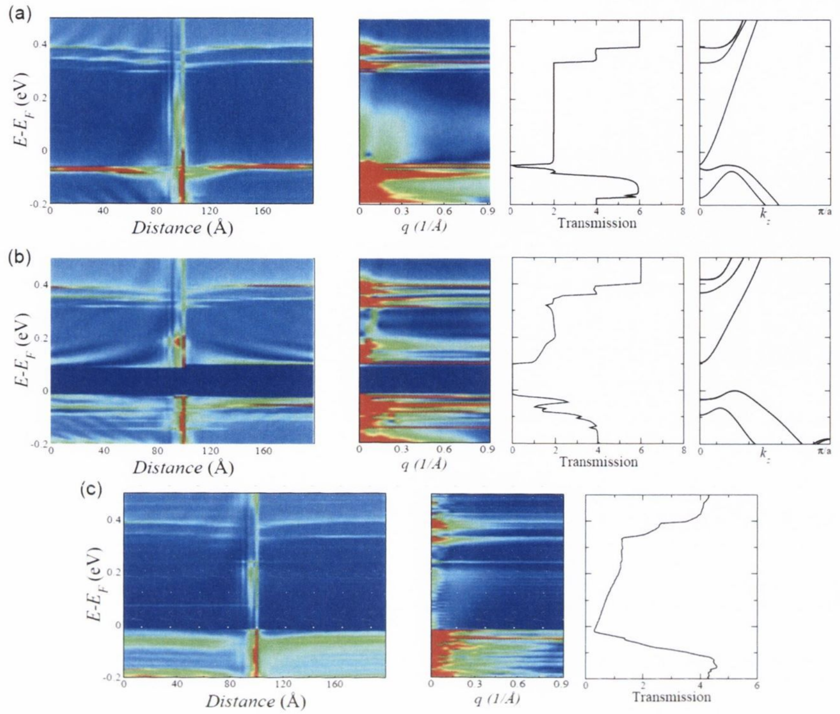

Figure 6.8: The DOS projected on the surface atoms along the scattering region at (a) $k_x = 0$, (b) $k_x = 0.032$ Å^{-1} and (c) integrated over all k_x. At $k_x = 0$ there are no oscillations. These start to emerge at $k_x = 0.032$ Å^{-1} but are not visible in the average. The second column of panels show the Fourier transform of the projected DOS in the flat region adjacent to the barrier, at the corresponding k_x. The scattering vector resulting from backscattering at non-normal incidence is clearly seen in (b). The average, however, reveals no scattering. The third column shows the transmission as a function of energy for the three cases. For $k_x = 0$ and $k_x = 0.032$ Å^{-1}, we also plot the band structure along transport direction for comparison.

comparison with the surface PDOS.

Figure 6.8 also makes apparent the band bending (of the order of 0.04 eV) introduced by the step. We will show in the next section that such band bending close to the step is a crucial ingredient for constructing a scattering model. Far enough from the step, however, the PDOS reverts to the unperturbed value within ~40 Å, consistent with experimental observation [102].

In contrast to similar steps on the Sb(111) surface [17, 103], in Bi_2Se_3 we find bound states close to the step edge and penetrating into the barrier (with an exponentially damped oscillating amplitude). These exist over the entire energy window in which the surface states are present. Similar features

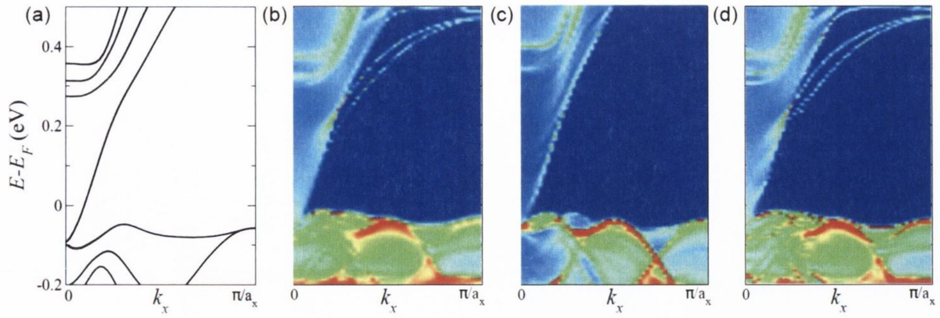

Figure 6.9: The energy dispersion along k_x (perpendicular to the transport direction) for (a) perfect periodic system comprising of 4-QL slab, (b) energy dispersion at the single barrier, and (c) 50 Å away from the single barrier. In (b), (c) and (d) color plots show the projected density of states on the atom present at the barrier, an atom 50 Å away from the barrier and the PDOS on the atom at the double barrier. In (b) and (d) note the additional pair of interface states outside the Dirac cone which merge with it around 0.2 eV.

with enhanced DOS have been measured by Alpichshev *et al.* [94] around surface barrier at the Bi_2Te_3 surface. Importantly such a bound state was not ascribed to the warped band structure of Bi_2Te_3. Our results point towards a similar bound state in Bi_2Se_3 as well. In the above mentioned experiment, no information could be obtained about the DOS on the lower side of the step. Our calculations in fact reveal that the state exists only on the higher side of the barrier, and the lower side has no such features. We have also calculated the energy dispersion of this state along the direction perpendicular to the transport. We plot the energy and k_x dependence of the PDOS on the Se atom at the barrier [shown in Fig. 6.9(b)] and on a surface atom 50 Å away from the barrier [Fig. 6.9(c)], and compare them to the band structure for the perfect periodic system [Fig. 6.9(a)]. For the atom present at the barrier we find additional pair of states outside the unperturbed Dirac bands, which however merge into the Dirac cone at $E - E_F \approx 0.2$ eV and produce an enhanced PDOS around that energy. Away from the barrier, however, the PDOS is very similar to that of the unperturbed system, consistent with the bound state being present only close to the barrier. We believe that these

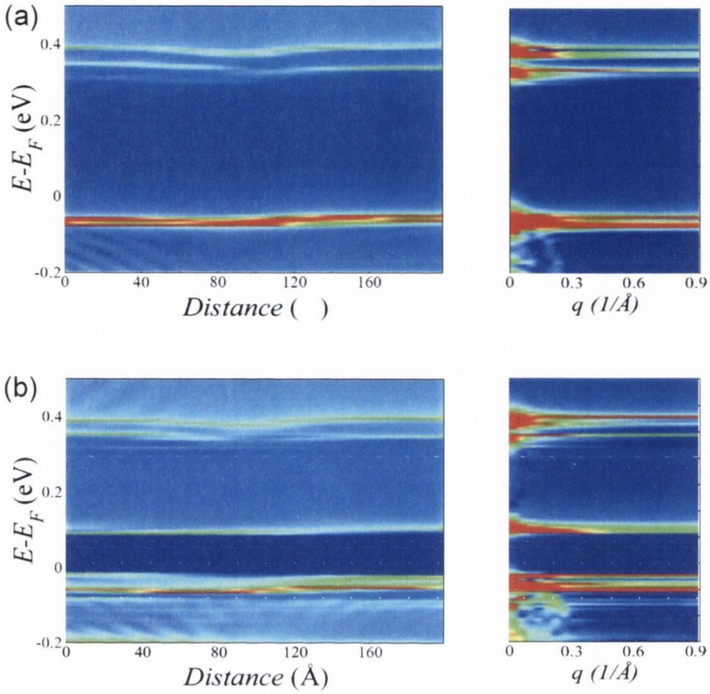

Figure 6.10: The DOS projected on the bottom surface atoms along the scattering region at (a) normal incidence $k_x = 0$, and (b) an oblique incidence $k_x = 0.032$ Å^{-1}. Note the absence of density oscillations in the bulk energy gap window, even at non-normal incidence. Panels on the right show the Fourier transform of the projected DOS in the flat region adjacent to the barrier. A comparison with Fig. 6.8 shows absence of both bound states as well as signature of dominant scattering vectors in the aforementioned energy range.

predictions of the bound state in Bi_2Se_3 and its energy dispersion may find verification in future experiments.

By analyzing the PDOS of the atoms at the bottom surface we have checked that significant scattering occurs only at the top one, i.e., it is caused by the presence of the step edge and not due to the tunneling back to the bottom surface. In Fig. 6.10 we plot the PDOS on the atoms present at the bottom surface at normal incidence and at a representative value of $k_x = 0.032$ Å^{-1} for oblique incidence. For both cases we can see absence of density oscillations in the energy range corresponding to the surface bands. Notably no signature of the bound state is also observed. Furthermore, we evaluate the Fourier transform of the PDOS in the flat region next to the step and find no features which may be mapped back to the scattering wavevector q, in contrast to the case of the top surface.

The local density of states (LDOS) associated to electronic states incoming from the left-hand side lead at 0.175 eV above the Fermi level are shown in Fig. 6.11 [104]. These clearly illustrate the three-dimensional nature of the path that electrons must traverse while crossing the barrier. The spin projections of the LDOS at $k_x = 0$ and $k_x = 0.032$ Å^{-1} are shown in the left and right panels, respectively. In contrast to pristine bismuth selenide the spins of the helical surface states are no longer confined to the plane of the slab. In the vicinity of the barrier they rotate out of the plane (the y component becomes finite). The LDOS at the bottom unperturbed surface provide a convenient comparison to the pristine surface, albeit with the spin directions reversed. At $k_x = 0.032$ Å^{-1}, the x and z components are dominant for the bottom surface, while the step edge introduces a component along the y direction comparable with the other two, at the top surface. A zoom close to the step shows a large DOS close to the step edge, which is due to the bound state.

A low-energy model

In order to compare to our *ab initio* results we construct a simple potential barrier model for the scattering problem. The surface states are described by a Dirac Hamiltonian [14]

$$\mathcal{H} = \epsilon_0 \mathbb{I}_{2\times 2} + \begin{pmatrix} V(z) & v(k_z - ik_x) \\ v(k_z + ik_x) & V(z) \end{pmatrix}, \tag{6.3}$$

where the potential profile $V(z)$ is shown in Fig. 6.12(a). The values of $\epsilon_0 = -0.05$ eV and $v = 4.58$ eVÅ, are obtained from our first-principles

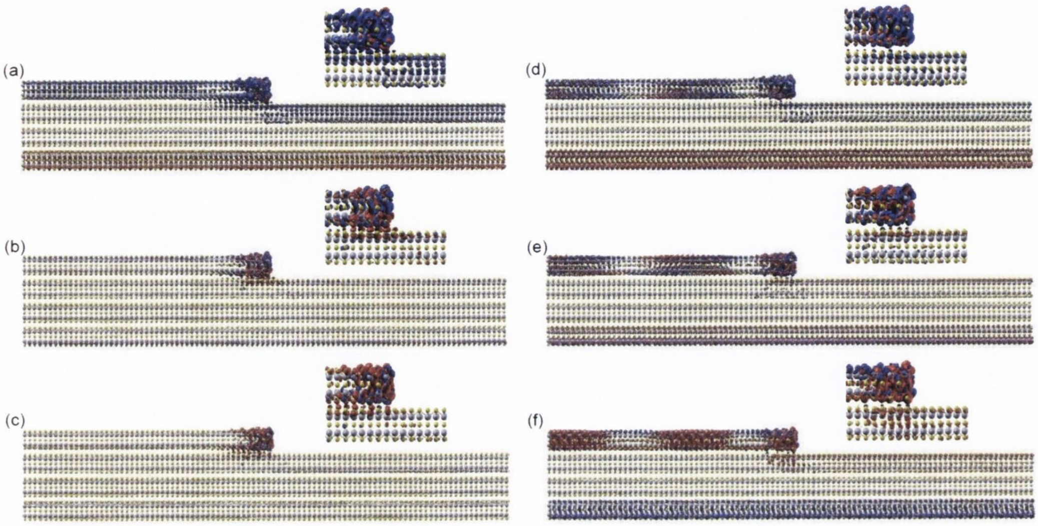

Figure 6.11: The spin-resolved local density of states incoming from the left lead at 0.175 eV with the spin projection along (a) x, (b) y and (c) z directions at $k_x = 0$. On the right hand side (d), (e) and (f) are corresponding plots for $k_x = 0.032$ Å^{-1}. Here red represents positive values while blue stands for negative values. Scattering at the step edge even at $k_x = 0$ allows the spin to rotate out of the plane of the slab resulting in a finite y and z components, in contrast to the unperturbed bottom surface where these are negligible. At non-normal incidence ($k_x = 0.032$ Å^{-1}) z component of spin-resolved LDOS becomes finite while the step edge introduces a non-zero y component. The insets are zooms around the step edge.

band structure. Here we consider only the upper part of the cone, i.e., $E = V(z) + \sqrt{k_z^2 + k_x^2}$. The corresponding eigenstate is given by,

$$\psi(k_x, k_z) = \frac{1}{\sqrt{2}} \begin{pmatrix} 1 \\ \frac{k_z + ik_x}{\sqrt{k_z^2 + k_x^2}} \end{pmatrix} e^{i\mathbf{k}.\mathbf{r}}. \tag{6.4}$$

One can then use the wave-function continuity conditions at the potential steps to solve for the transmission and reflection coefficients in a straightforward manner. The potentials in the 4-QL and 3-QL leads, respectively V_1 and V_4, are nearly identical and are set to zero. V_2 is the potential associated to the barrier and extends over a length d, while V_3 is the band bending, which is finite over a distance L. The calculated transmission curves are plotted in Fig. 6.12(b) for $V_3 = -0.02$ eV and in Fig. 6.12(c) for $V_3 = 0$. The shape of the transmission function is much closer to that obtained from the *ab initio* calculations for finite $V_3 = -0.02$ (this value of V_3 is chosen from our first-principles results), as compared to the situation where $V_3 = 0$. While this comparison does not provide definite evidence of importance of band bending, it serves as an illustration that it is one of the factors which need to be considered while performing a quantitative modeling of step edges on topological insulator surfaces. Although it appears that this simplified model can qualitatively reproduce the transmission obtained from first-principles, a more careful analysis shows that it neglects a number of important aspects of the scattering problem. It does not take into account the three-dimensional nature of the barrier, and as a consequence it cannot capture the change in spin orientation of the surface states near the barrier. Moreover it needs as an input the values of the scattering potentials, which an atomistic description is capable of providing, while also capturing the fine details of the scattering process. We also note that several models have been proposed to study topological states on a curved surface. These predict no backscattering at any angle from hyperbolic steps [87]. Unfortunately these models are not valid for atomic-scale abrupt steps that we have studied in this section.

Scattering from double barriers

We now analyze the scattering properties of double barrier structures constructed over the $Bi_2Se_3(111)$ surface. The scattering region is shown in Fig. 6.1(d) for the shorter surface barrier. This time the scattering structure is connected on both sides to two identical semi-infinite leads (3-QL slabs). As before, we begin by looking at the transmission across the surface as shown in Fig. 6.13(a). Again counter-propagating spin-momentum-locked states yield a perfect transmission at normal incidence. As discussed for the single barrier case, at finite k_x the transmission is then reduced. However, in

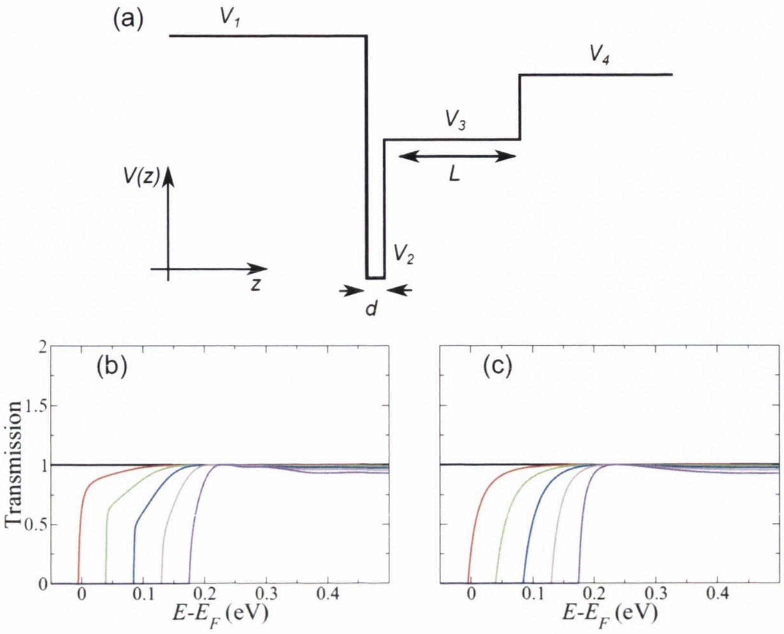

Figure 6.12: (a) Potential profile for the Dirac model. We use $V_1 = V_4 = 0$, $V_2 = -1.17$ eV, $d = 20$ Å and $L = 60$ Å. The transmission as a function of energy is shown choosing (b) $V_3 = -0.02$ eV and (c) $V_3 = 0.0$ eV. Different curves correspond to the same k_x points as Fig. 6.7(a).

contrast to the previous analysis, there are also resonant energies at which the transmission reaches up the value of two, i.e., there is no reflection. At these particular energies the system displays Fabry-Perot resonances, which are characteristic of one-dimensional scattering from double potential barriers. In Fig. 6.13(b) we plot the transmission as a function of the incident k_x for different energies. Away from the resonances the transmission shows again a cosine-like behavior with transmission going down to $T = 1$ as the incidence angle increases (k_x gets larger). At even larger k_x (not shown) the transmission drops down to zero when the band edge for the Dirac cone is reached at the bottom surface, similar to the case of single barrier.

The k_x-resolved and total DOS projected on the surface atoms is plotted in Fig. 6.14, where the bound state can be clearly seen in the 4-QL region extending from 10 Å to 60 Å. The DOS associated to such bound state oscillates and decays towards the center of the quantum well defined by the

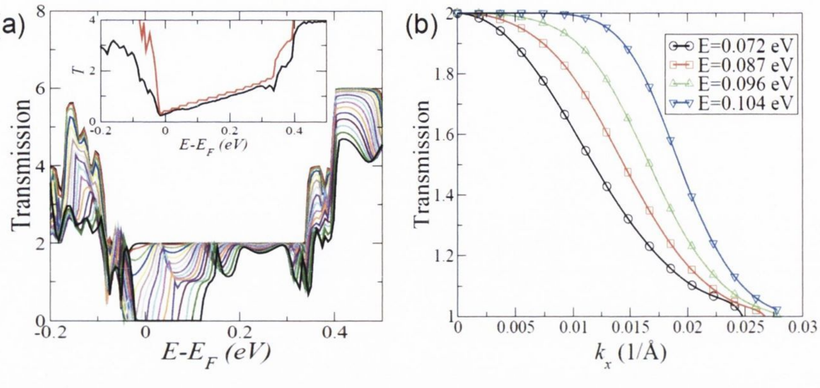

Figure 6.13: (a) Transmission across the double barrier on the surface at different k_x. Note the Fabry-Perot type oscillations in transmission in contrast to Fig. 6.7(a). Different curves correspond to the same k_x points as Fig. 6.7(a). Integrated transmission with (black curve) and without (red curve) the barriers is plotted in the inset. Transmission as a function of k_x at different constant energy cuts is shown in (b).

two barriers at the step edges. A band bending similar to that observed for the single barrier is also seen for this particular barrier configuration. The interaction between the bound states localised at the two barriers splits them in energy, creating alternating high and low DOS as one moves up along the energy axis. Another noticeable feature is a state localized in the 4-QL region at around 0.1 eV [see Fig. 6.14(b)]. This is an additional state in the 4-QL slab, which is decoupled from the 3-QL leads. The same state is absent in the case of a single barrier produced by a step edge between a 3-QL and a 4-QL semi-infinite lead. The Fourier transforms of the DOS display similar features as those shown in Fig. 6.8. However, in the double barrier case the resolution is improved over that of the single barrier structure since we now have more atoms along the flat region next to the barrier.

We also study the energy dispersion of the quasi-bound state obtained at the barrier, by calculating the PDOS on the Se atom at the barrier, as a function of $E - E_F$ and momentum along the step (k_x). This is shown in Fig. 6.9(d), with a comparison to the band structure of the unperturbed periodic system. Apart from the Dirac bands, additional states, dispersing along k_x are visible at the interface. These have a dispersion very similar to the case of a single barrier [see Fig. 6.9(b)]. However, some additional features are seen when this pair of states mixes with the Dirac bands, with an alternating pattern of higher and lower PDOS being visible. This is due to the interaction between the bound states at the two barrier edges. Away from the interface the PDOS and the dispersion reverts to that of the pristine system with only the Dirac bands being present.

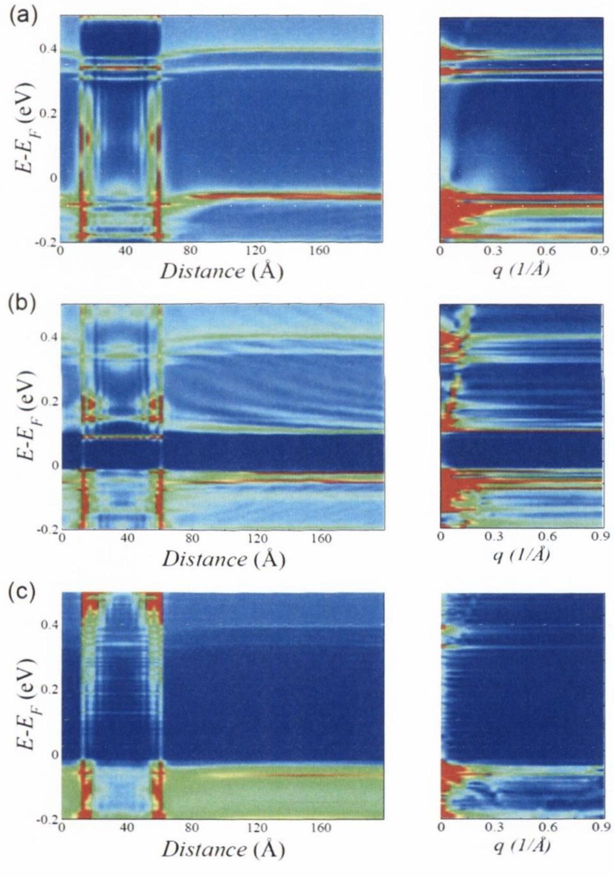

Figure 6.14: PDOS on surface atoms along the double barrier scattering region at (a) $k_x = 0$, (b) $k_x = 0.032$ Å^{-1} and (c) integrated over all k_x. Note the absence of density oscillations for $k_x = 0$ and integrated figures. Incidence at finite k_x leads to density oscillations clearly seen in the long flat region adjacent to the barrier as shown in (b). The panels on the right are the corresponding Fourier transforms.

Note that for this particular chosen length of the double barrier there are no quantum well states formed inside the 4-QL region. However, for a longer barrier the quantum well states appear, as demonstrated by the PDOS on

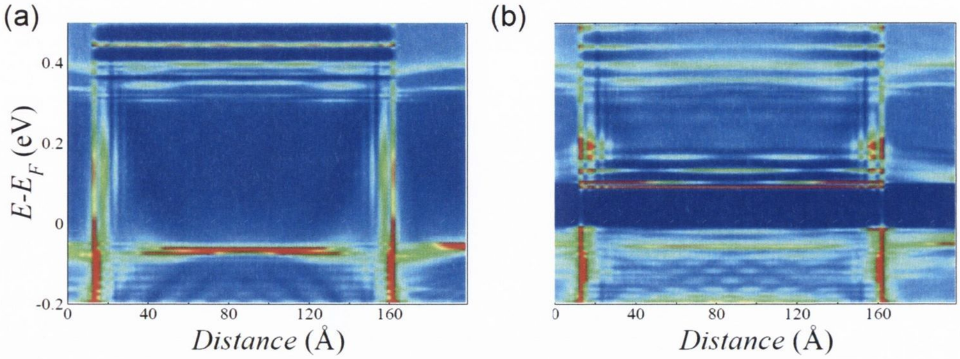

Figure 6.15: PDOS on the surface atoms for a double barrier of length 149.16 Å at (a) $k_x = 0$ and (b) $k_x = 0.032$ Å^{-1}. Note the absence of quantum well states in (a). In (b) quantum well states interact with the bound state at the two barriers leading to energy splitting of the bound state.

the surface atoms at two different k_x for a barrier of length 149.16 Å (see Fig. 6.15). At normal incidence no quantum well states can be formed in the energy window of the surface state, since the two surface states have opposite spin projections leading to no interference. In contrast, at finite k_x quantum well states appear (e.g. a nodeless state at around 0.13 eV and a single-node state at around 0.16 eV). However, the behavior of these states near the edges of the barrier is different from usual because of the presence of the bound state. In fact, these quantum well states interact with the bound states at the edges of the barrier resulting in an energy splitting of the bound state. We observe splitting of the bound states in both the short and the long double barrier, in the former case due to the interaction between the bound states located at the two edges of the 4-QL region, while in the latter due to the bound state interacting with the quantum well state within the barrier.

6.2.3 Summary and Conclusions

To conclude, we have used *ab initio* transport theory to study scattering of topological surface states on $Bi_2Se_3(111)$ surface from both single and double barriers. We have studied the dependence of the transmission on the angle of incidence and electron energy. At normal incidence our first-principle calculations have confirmed Klein tunneling. Furthermore, we have calculated the density of states on the surface atoms and found bound states occuring only on the higher side of the barrier. Our local density of states plots have made apparent the three-dimensional nature of the scattering problem, in which the spins of the surface states are no longer confined to the plane of the topological insulator slab. We have also constructed a simplified potential barrier model using linear Dirac bands to compare with our first-principles calculations. Throughout the study we have placed our results in the context of recent experimental works.

Chapter 7

Single atom magnetoresistance on topological insulator surface

Conventional magnetoresistance (MR) devices utilize two magnetic materials as electrodes, one as polarizer and the other as analyzer, separated by a spacer. Recently, Burkov and Hawthorn found a new kind of MR on topological insulator surface, which requires only one ferromagnetic electrode [105]. A spin-valve on topological insulator surface, which shows an anomalous MR, has also been studied by model calculations [106].

In this Chapter, based on *ab initio* electron transport calculations, we report an anisotropic single atom magnetoresistance on the topological insulator surface, stemming from an interplay between the helical surface states and the spin anisotropy of the magnetic adatom. This is a novel type of MR, which does not need any magnetic electrodes, but requires a magnetic adatom, or more generally adsorbed magnetic clusters or magnetic thin films. Crucially, our proposal does not rely on opening a band gap in the surface states, which requires establishing ferromagnetic order on the topological insulator surface. Instead we focus on the magnetic anisotropy of adatoms on topological insulator surfaces, which is known to be significant (a few meV) both from first-principles calculations [107] and magnetic circular dichroism measurements [108]. Moreover a controllable magnetic doping of Bi_2Se_3 surface state has already been achieved [109].

In the presence of magnetic impurities, the spin of surface electrons may be flipped and it is expected that scattering should not be forbidden. However, there are experimental reports, which have found apparently contradicting conclusions and it is not clear whether this scattering is observed or not [88, 110]. Our results provide a possible explanation to reconcile these observations. We show that in the presence of magnetic impurities new backscattering channels are opened. These, however, are found only at those energies where the impurity presents a large density of states, and hybridizes with the underlying topological insulator surface states. Away from these energies the transmission is close to the unperturbed value and no signature of the magnetic dopant is seen in the transmission. We find that at those energies the conductance depends strongly on the orientation of the local moment on the magnetic adatom, which implies a large magnetoresistance. Our large-scale calculations also allow us to probe the real-space spin texture around the magnetic adatom. The inclusion of atomistic details, without any free parameters, reveals significant differences from previous model based calculations [56, 97].

7.1 Anisotropic magnetoresistance on topological insulator surface

7.1.1 Computational Details

First-principles transport calculations were performed employing the SMEAGOL code, in a manner similar to the work presented in Chapter 6. We use a double-ζ polarized basis, with a real space mesh cutoff of 300 Ry. The generalized gradient approximation for the exchange-correlation functional is used. We treat the Bi 6s and 6p, Se 4s and 4p and Mn 3d and 4s as valence electrons, while norm-conserving Troullier-Martins pseudopotentials are used to describe the core electrons. The Mn adatom is placed in the on-top Bi geometry, which is the most stable binding site [107]. One may expect changes in details of scattering by changing the adsorption site, however the basic principle of single atom MR is expected to be valid for any adsorption site. For atomic relaxations, all the atoms in the top quintuple layer (QL) are allowed to move and the structures are relaxed until the forces are less that 0.001 eV/Å. For transport calculations, semi-infinite electrodes comprising of 3 QL slabs of Bi_2Se_3 are attached to the left and the right of the scattering region (shown in Fig. 7.1). A minimum vacuum region of 25 Å is included along the slab thickness (y-direction). We use a $3\times1\times1$ k-point grid for converging the charge density, while a much denser grid of at least 80 k_x-points is employed to evaluate the transmission, reflection amplitudes and densities of states.

7.1.2 Results

The transmission coefficient for different orientations of the Mn magnetic moment is shown in Fig. 7.2. For $k_x = 0$ [normal incidence, Fig. 7.2(a)]

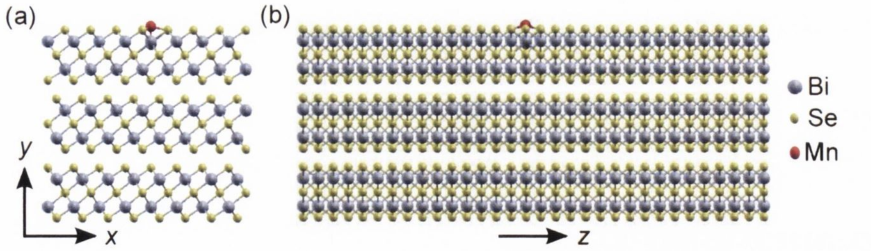

Figure 7.1: Transport setup with Mn atom adsorbed on 3 quintuple layer Bi_2Se_3 slab, (a) viewed in the plane perpendicular to and (b) along the transport direction (z). The scattering region supercell consists of 8 primitive unit cells of Bi_2Se_3 in the xy plane and 16 unit cells along z, giving a concentration of 1 Mn atom in 1920 bismuth selenide atoms ($\approx 0.05\%$) allowing us to reach dilute concentrations comparable to experiments.

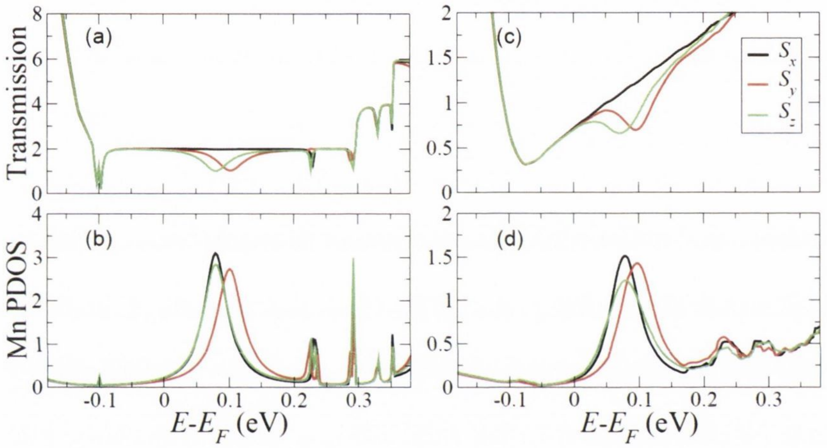

Figure 7.2: Transmission and projected density of states on Mn for different Mn spin directions (a) and (b) at $k_x = 0$, and (c) and (d) averaged over all incidence angles. For Mn spin along x, transmission is unperturbed, while reduced transmission occurs for other directions, resulting in a single atom anisotropic magnetoresistance.

and the Mn spin aligned along the x-axis, which is the spin direction of the incoming electron's traveling along the positive z-axis, the transmission is close to two in the energy window of the topological state (approximately -0.1 eV to 0.3 eV), i.e., there is a unity contribution from each surface. In contrast, for the two orthogonal Mn spin directions, a dip in transmission occurs in the energy range, where a peak in the Mn projected density of states (PDOS) is found. When the Mn spin is along x, there is no reduction in transmission, even though there is a peak in Mn PDOS with a height comparable to the case of the other two directions. In all the three cases we find the Mn adatom having a moment close to 4.5 μ_B, in agreement with previous reports [107]. Furthermore, we find a substantial in-plane magnetic anisotropy of 6 meV, a value which we have also verified from plane wave calculations using VASP code for a smaller $3\times1\times3$ supercell. After integrating over the entire Brillouin zone for all k_x values a similar picture is obtained [see Figs. 7.2(c) and 7.2(d)]. Thus, we find that at the energies of the Mn states there emerges an *anisotropic* MR, depending upon the spin orientation of the magnetic adatom. We find a MR, MR $= (T_{x,s} - T_{\alpha,s})/T_{\alpha,s}$, of 670% (here $T_{x,s}$ is the transmission at the top surface with the Mn spin along x and $T_{\alpha,s}$ is the surface transmission for the other two Mn spin directions $\alpha = y, z$).

We emphasize that this mechanism for MR does not involve opening a band gap in the surface state spectrum. In this particular setup the transport is along the z direction and, for normal incidence, the spin-momentum relation locks the spin of the surface state along x. If the Mn impurity spin points along this direction, then electrons suffer minimal scattering and the resistance is low, while for other Mn spin directions we find a high resistance state. In contrast, if the electrodes are positioned in the orthogonal configuration, such that transport is along x, then the propagating electron spin will be along z. In this case the low resistance state will be obtained for the Mn spin parallel to the direction of propagation, z, while the other two directions will yield a high resistance state [see Fig. 7.4(e)]. Since the resistance is given by the orientation of the local magnetic moment with respect to the transport direction, this MR is also anisotropic.

From the previous results it is not possible to unequivocally distinguish whether the scattering occurs due to spin-flip between states on one surface or if the MR is an artifact of inter-surface scattering caused by the finite Bi_2Se_3 slab thickness. We clarify this issue by calculating the full scattering matrix

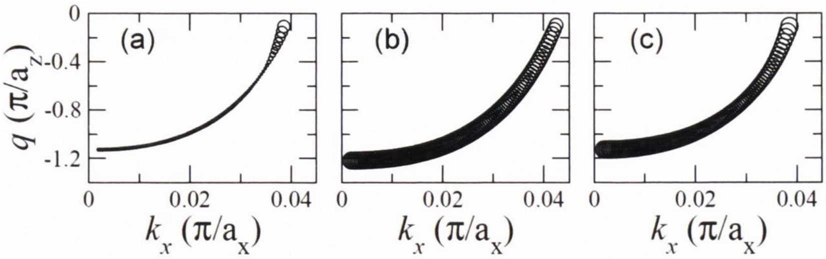

Figure 7.3: Scattering vectors (q) as a function of the incident wave vector (k_x) for Mn spin along (a) x, (b) y, and (c) z directions. The size of circles is proportional to the reflection amplitude. The curves are plotted at energies corresponding to peaks in Mn density of states, $E - E_F =$ 0.08, 0.10 and 0.08 eV, for Mn spin along x, y and z, respectively. Here a_x and a_z are lengths of electrode unit cell along x and z directions.

and evaluating the transmission and reflection amplitudes for the individual scattering states on the top and bottom surfaces [111]. We obtain inter-surface reflection and transmission amplitudes always smaller than 0.008. For intra-surface scattering, in contrast, these quantities reach values up to 1, which confirms that the slab is thick enough to prevent significant coupling between opposite surfaces.

A deeper analysis is provided by studying the scattering wave vectors, q, and the reflection amplitudes, r, on the top surface of the topological insulator slab at the peak energy in Mn PDOS, as a function of the wave vector k_x along the direction perpendicular to transport. Here $q = k_{z,\mathrm{out}} - k_{z,\mathrm{in}}$ is the difference between the outgoing, $k_{z,\mathrm{out}}$, and incoming, $k_{z,\mathrm{in}}$, z-components of the scattering wave vectors. Since in the bulk gap both $k_{z,\mathrm{in}}$ and $k_{z,\mathrm{out}}$ for the topological surface states are functions of k_x, we can evaluate q as function of k_x. The result is presented in Fig. 7.3, with the size of the circles denoting the reflection amplitude $r(k_x)$. Since the constant energy surface in the energy range of the topological states is approximately circular, we also find the corresponding q-k_x plot having a circular shape. For the Mn spin along x and for small k_x the reflection amplitude is vanishingly small, while it becomes larger when k_x increases. This is because the overlap between the

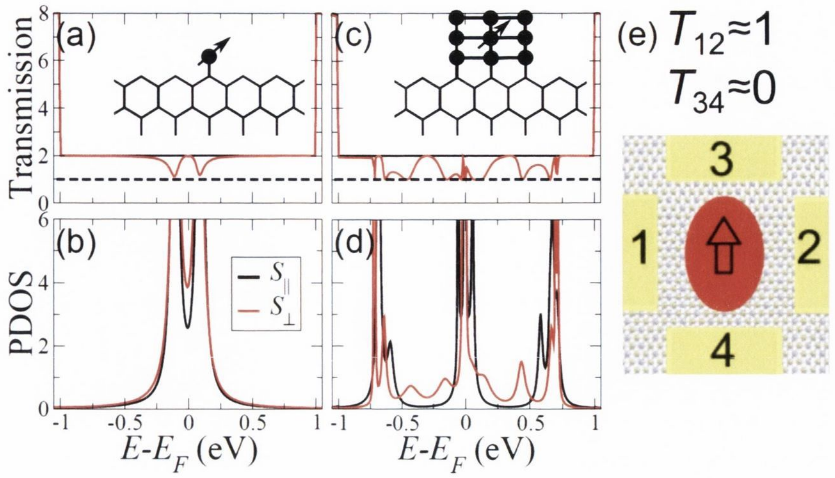

Figure 7.4: (a) Transmission and (b) adatom projected density of states for the two-dimensional model, with adatom spin pointing parallel and perpendicular to electron spin. (c) Transmission and (d) average projected density of states for magnetic cluster in the two spin configurations. The insets are schematic of the two setups and dashed lines indicate transmission of one from the unperturbed edge. Here we set adatom onsite energy to 0.1, hopping elements to ribbon as 0.3, hopping between magnetic atoms to 0.5 (in units of the nearest neighbor hopping) and other parameters are same as chosen in Ref. [72]. (e) Schematic of four-probe geometry to measure the anisotropic magnetoresistance.

two counter-propagating surface states get larger when k_x increases. Thus, when the Mn spin is along x the impurity behaves as a non-magnetic scattering center [112]. In contrast, for the other two directions a large reflection is present even for $k_x = 0$, which persists at larger k_x. The total reflection is obtained by integrating this function over all k_x, so that the underlying difference in reflection amplitude for small k_x is what yields the anisotropic MR.

Recent scanning tunneling microscopy studies of magnetic adatoms on topological insulator surfaces have observed either new scattering channels, to be ascribed to magnetic scattering [110], or found the scattering independent of the magnetic nature of the adatom [88]. Our calculations provide a possible explanation for these conflicting observations. The transmission coefficients show that a new backscattering channel is created only at the energy of the adatom PDOS, while at all other energies where the topological state exists, no fingerprint of the magnetic adatom is visible. Thus, a likely explanation

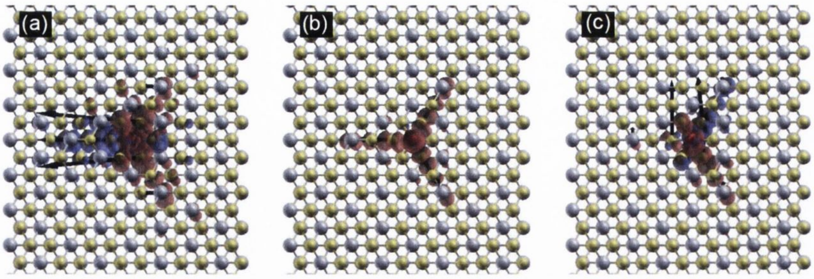

Figure 7.5: A combination of projected and local density of states showing real space spin texture around the magnetic adatom with its spin pointing along (a) x, (b) y, and (c) z directions, at the energy of peak in Mn density of states. The arrows denote the in-plane spin components obtained from atom-projected density of states. The isosurfaces correspond to the local density of states projected along the direction normal to the plane, with red denoting positive values and blue representing negative values. The effect of adatom spin in not limited to the top surface Se atoms, but is distributed over the first quintuple layer.

to reconcile experiments is that the adatom should not only hybridize with the topological insulator surface, but also present peaks in density of states at relevant energies for being detected in the transmission spectra. These depend on the specific magnetic atom and the adsorption site and therefore can differ in different experiments.

The anisotropic MR can be understood by considering the impurity as the source of an effective local magnetic field. If the spin of the adatom is parallel to the spin of the propagating electron such an effective field provides a collinear scattering potential, thus precluding spin mixing and backscattering. However, if the local spin forms an angle with that of the itinerant electrons, opposite spin electrons will couple and thus backscattering between helical states will become possible. A minimal two-dimensional model can be used to verify the generality of the MR. We use the Kane-Mele model [27] for a ribbon with a magnetic adatom or a magnetic cluster placed at the ribbon edge and an exchange coupling between the electron spin and the impurity [72]. The edge electrons in this model capture the essential physics of the $k_x = 0$ case of three-dimensional topological insulators, which is responsible for the anisotropic MR. The results are shown in Fig. 7.4. The transmission is high for the adatom spin parallel to the electron spin, while it is low for other angles, thus the model calculations confirm our first-principles results. Furthermore, for the magnetic cluster the MR is obtained over an energy range larger than that of the single adatom. The fact that the anisotropic MR is independent of the details of adatom means that one can select other magnetic ions to tailor the anisotropy direction. For instance, Cr and Co on Bi_2Se_3 exhibit an out-of-plane easy axis, while Mn and Fe present an in-plane one [107].

In addition to a two-terminal device the anisotropic MR can be measured in a four-probe setup [Fig. 7.4(e)]. When the impurity spin points in the direction shown (e.g. due to the magnetic shape anisotropy), then a measurement of the resistance between the electrodes 1 and 2 yields a low resistance state, while high resistance is measured between 3 and 4. If a thin film with in-plane magnetization is used, then a MR will be obtained depending on the in-plane orientation of the magnetization. Out-of-plane magnetization, in contrast, always yields a high resistance state. In general, when the impurity spin points parallel to the helical electron spin the resistance is low, while other angles between the two spins will result in a higher resistance. A large magnetic anisotropy also implies the likely absence of Kondo-type features, which occur with degenerate ground states. Furthermore we expect the spin-flip of the impurity to be negligible as long as the bias is smaller than the magnetic anisotropy [73]. Going a step further, we have found the same anisotropic MR for magnetic clusters, in which the aforementioned effects will be even smaller and the magnetic anisotropy may be engineered to be large.

Since our *ab initio* calculations employ extremely large supercells, we are in the position to probe the real-space spin texture around the isolated magnetic impurity. This has been previously studied with Dirac-like effective Hamiltonians [56, 97], but here the full details of the electronic structure are included. A combination of atom projected DOS and local DOS is shown in Fig. 7.5 for the three different orientations of the Mn spin at the energy corresponding to the peak in Mn PDOS of any given orientation. The induced spins on the atoms around Mn are predominantly along the direction of the Mn spin. For Mn spin pointing along y, we find a hedgehog-like in-plane spin texture, with the spins pointing outwards from the impurity site. This contrasts continuum models, which yield a vortex-like in-plane structure [56, 97]. The out-of-plane spin points along the positive y direction, in agreement with the model results. This spin is induced over the first QL. For Mn spin along y, the spin texture exhibits a three-fold rotational symmetry of the underlying lattice, which is not captured by the continuum low-energy model. For the other two directions, this lattice symmetry is broken by the Mn spin and the neighboring atoms exhibit a spin along the impurity spin direction. We have also investigated the spin texture at other energies and found similar directions as those presented in Fig. 7.5, although the magnitude of the induced spin decreases at energies away from Mn PDOS peak. Our spin texture predictions naturally call for an experimental corroboration via spin-polarized scanning tunneling microscopy [113, 62].

7.1.3 Summary and Conclusions

In conclusion, we have discovered single-atom anisotropic magnetoresistance on topological insulator surfaces decorated with magnetic adatoms. This effect is a consequence of the spin-momentum locking of topological insulator surface states interacting with the adatom spin. The MR does not originate from the opening of a gap in the surface band structure, nor from spin injection. Our results provide a possible explanation for the conflicting observations concerning scattering from magnetic atoms on topological insulator surfaces. Our order-N code allowed us to study the real space spin texture around the adatom, which has differences from previous model calculations. Based on these findings we propose a class of magnetoresistive devices with potentially large MR, utilizing either single magnetic atoms or thin film nanodots incorporated between two non-magnetic electrodes, using an in-plane rotation of the thin film magnetic moment.

Chapter 8

Topological tuning of two and three dimensional Dirac semimetals

A particularly intriguing prospect is that of using the interaction between different materials to create hybrid interfaces with topological properties. For instance depositing normal semiconductors on top of three-dimensional topological insulators may result in a structure that under certain conditions exhibits topologically protected interface states [114]. An even more attractive prospect is that of using this protocol for transferring topologically protected states to graphene. Since graphene-based transistors have been already demonstrated [115], one could then speculate on having graphene logic elements connected by topological-graphene interconnects, i.e., on realizing an all graphene high-performance logic circuitry. A major advantage of such a strategy is that it is fully compatible with two-dimensional patterning. In the first section of this chapter we propose and show that a topological phase can be transferred to graphene by proximity with the three-dimensional topological insulator Bi_2Se_3. By using density functional and transport theory we prove that, at the verge of the chemical bond formation, a hybrid state forms at the graphene/Bi_2Se_3 interface. The state has Dirac-cone-like dispersion at the Γ point and a well-defined helical spin-texture, indicating its topologically protected nature.

Motivated by the two-dimensional Dirac-like semimetallic state in graphene, Dirac semimetals in three dimensions were theoretically proposed recently [125]. Using first-principles calculations, Wang and co-workers predicted sodium bismuthate (Na_3Bi) and cadmium arsenide (Cd_3As_2) to be three-dimensional Dirac semimetals [126, 127]. Their experimental realization was not far behind and the prediction has been verified by means of angle resolved photoemission measurements in a remarkably rapid flurry of activity by a number of groups [128, 129, 130, 131, 132]. Interestingly, a Dirac semimetal state was also found in zinc blende compounds [133]. Apart from hosting a bulk Dirac cone, both Na_3Bi and Cd_3As_2 also show a band inversion at the center of the Brillouin zone. This means that they exhibit a surface Dirac spectrum when confined to a slab geometry, analogous to conventional topological insulators [14]. Given their unique electronic structure they open up an exciting platform to study topological phase transitions, interweaving two and three-dimensional Dirac states. In the second half of this chapter we study the interplay of bulk and surface Dirac fermions in three-dimensional Dirac semimetals using first-principles calculations. By combining density functional theory with the coherent potential approximation we reveal a topological phase transition in the alloy $Na_3Bi_{1-x}Sb_x$, where the system goes from a Dirac semimetal to a trivial insulator upon changing the Sb concentration. This tuning of composition allows one to engineer the position of the bulk Dirac points in the reciprocal space. Interestingly, the phase transition coincides with a reversal of the band ordering between the conduction and valence bands.

8.1 Proximity induced topological state in graphene

Several proposals have been already brought forward for making graphene a topological insulator. Indeed, one of the first topological insulator model was based on a staggered hexagonal lattice with helicity-dependent complex hopping parameter, simulating spin-orbit interaction, i.e., the Kane-Mele model, which we have encountered several times in this thesis [27, 28]. However, since spin-orbit coupling in graphene is tiny, a topological phase may be induced only by strongly perturbing the graphene electrostatic potential, for instance by adsorbing heavy ions on top of the sheet [116]. Importantly, although theoretically sound, such proposal requires ultra-accurate fabrication precision and appears rather challenging in practice. Here we suggest a completely different approach: we introduce topologically protected states in graphene by proximity with a lattice-commensurate three-dimensional topological insulator. This happens at the graphene/Bi_2Se_3 interface, a composite which was synthesized about two years ago [117, 118, 119], but whose electronic structure still remains unclear.

8.1.1 Computational Details

Calculations were performed by density functional theory (DFT) as implemented in the VASP code [81]. We used the Perdew-Burke-Ernzerhof form of the generalized gradient approximation and the core electrons were described by projector-augmented-wave pseudopotentials. The k-space integration spans a $11 \times 11 \times 1$ Monkhorst-Pack mesh in the irreducible Brillouin

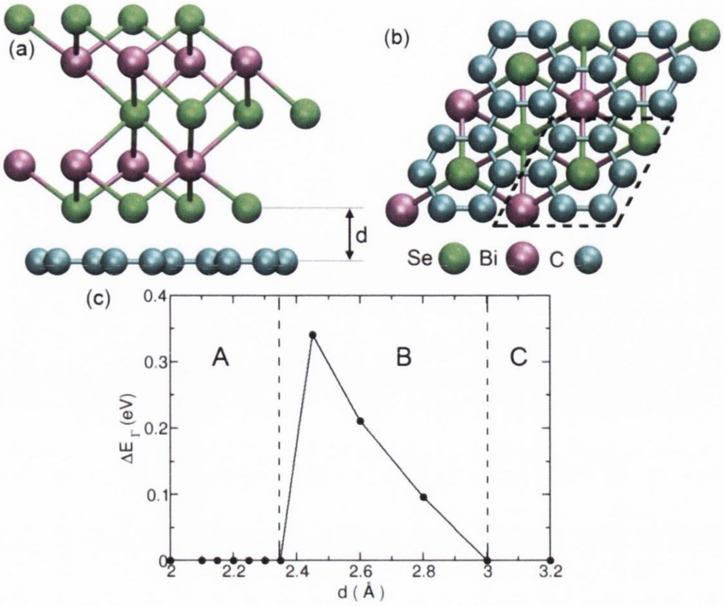

Figure 8.1: Side (a) and top view (b) of the graphene/Bi_2Se_3 interface. The graphene-Bi_2Se_3 separation is d. In panel (c) we report the graphene electronic band gap as a function of d.

zone and the plane waves cutoff is 400 eV.

The geometry of the structure investigated is shown in Fig. 8.1. We consider a Bi_2Se_3 slab containing three quintuple layers (QLs), for which the tensile stress is minimal among the experimentally investigated Bi_2Se_3/graphene composites [117]. The Bi_2Se_3 unit cell is commensurate with three graphene unit cells, hence the elementary unit cell of the composite contains an entire carbon ring. The contacting Se atom is placed at the graphene hollow site (in the center of the ring). The in-plane lattice parameter is 4.26 Å, which is only 2.3% larger than the lattice parameter of bulk Bi_2Se_3; the one perpendicular to the interface is instead 40 Å (there is a vacuum region of at least 10 Å between cells periodic replica). We have also investigated a second geometry where the carbon atoms are on top of Se. This configuration, however, is not energetically favorable and it has not been considered in the rest our analysis. Interestingly both interface structures present rather similar trends in the electronic structure properties.

8.1.2 Results

We begin by investigating the evolution of the graphene band gap with the graphene/Bi_2Se_3 distance, d. We assign an electronic band to a given material by projecting the energy and k-dependent wave function onto spherical harmonics centered around particular atoms. We define the graphene electronic band gap from those bands located near the charge neutral point of free-standing graphene and having dominant C character. In Fig. 8.1(c) one can identify three different regions. For $d > 3$ Å (region C) graphene has no band gap. This is expected since for large separations the interaction is weak and the band structure of the composite is a superposition of those of the constituents. As such graphene remains a zero-gap semiconductor. Region B is characterized by the opening of the graphene band gap. The gap increases monotonically from $d = 3$ Å and it reaches a maximum (0.34 eV) for $d = 2.45$ Å. A further reduction in d (region A) closes the gap, which remains closed up to $d = 2$ Å.

Next we analyze in Fig. 8.2 the nature of the graphene bands around the Fermi level, E_F, as a function of d. For $d > 3$ Å [Fig. 8.2(a)] the composite features two superimposed band structures corresponding to those of graphene and Bi_2Se_3, respectively. At such large separation there is no wave function overlap between graphene and Bi_2Se_3, leaving the two materials electronically decoupled. Graphene's linearly dispersive bands (in blue in Fig. 8.2) at each of the valleys (Dirac K-points) are two-fold spin-degenerate, with the π ($E < E_F$) and π^* ($E > E_F$) bands just touching each other. The Bi_2Se_3 surface states (green bands in Fig. 8.2) cross E_F at the Γ point.

Decreasing d below 3 Å causes a band gap opening between the π and π^* bands [see Fig. 8.2(b), $d = 2.6$ Å]. Now the graphene valleys are placed together with the Bi_2Se_3 surface states around the Γ point due to the bands

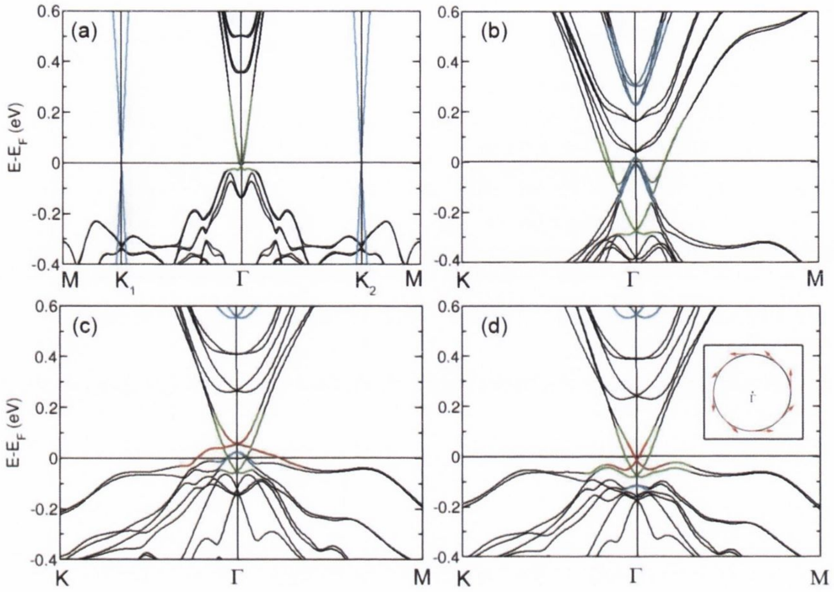

Figure 8.2: Evolution of band structure of the graphene/Bi_2Se_3 composite as a function of the separation d between the two constituents. In panels (a), (b), (c) and (d) we present the band structure for $d = 3.0$ Å, 2.6 Å, 2.3 Å and 2.2 Å respectively. Black and green bands are bulk and surface states of Bi_2Se_3, blue bands are graphene bands, while the red ones represent hybrid states. The inset in the panel (d) illustrates the spin-texture of the mixed state at 0.05 eV above E_F. Note the different k-point sampling for $d = 3.0$ Å.

folding in the supercell structure. As the graphene electronic gap increases further upon a reduction of d [see $d = 2.4$ Å, Fig. 8.2(c)], the π^* cone lifts up in energy but the tip of the π one remains pinned at E_F. The topologically protected surface states of Bi_2Se_3 (one per surface) are positioned in the vicinity of the tip of the π cone. For separations $d > 2.6$ Å these surface states form a doubly-degenerate state since the two surfaces are equivalent for the unperturbed topological insulator slab. For distances $d \leq 2.6$ Å the symmetry of the topological insulator slab breaks due to the vicinity of the graphene layer and the degeneracy of the surface states is lifted. The topological surface state in contact with graphene moves up in energy at Γ by about 0.11 eV for $d = 2.3$ Å. Importantly, the graphene states that are pinned at E_F start to couple with the surface state and, for $d \leq 2.3$ Å, the 4-fold degeneracy of the π cone is lifted. Here the pure graphene bands forming the π cone are pushed down in energy and only the mixed graphene/Bi_2Se_3

band [red in Fig. 8.2(d)] and the Bi_2Se_3 surface state at the opposite side of the interface (placed directly beneath the mixed band at Γ) cross E_F.

Intriguingly, such newly formed mixed graphene/Bi_2Se_3 band presents a helical spin-texture, demonstrated in the inset of Fig. 8.2(d). This is a sufficient condition for disabling back-scattering of charge carriers, and it is not the case in a pristine graphene sheet. In fact, defects in graphene allow hopping of charge carriers between two valleys, which causes back-scattering due to their opposite winding numbers. In contrast, hopping is impossible in systems with only one valley and a helical spin-texture, which is the case for graphene/Bi_2Se_3 heterostructure.

The supercell structure causes the folding of the second Brillouin zone (BZ) of primitive graphene into the first and consequently the migration of the graphene valleys from K to Γ. Thus, two 4-fold degenerate cones touching at E_F are formed. The bands from the two valleys have opposite topological charges, which causes their mutual annihilation [120]. This manifests itself in the opening in graphene of a band gap [see Fig. 8.2(b) and (c)], much larger than that estimated for thallium adatoms deposition [116].

After having determined the emergence of a mixed graphene/Bi_2Se_3 band, we now analyze in detail its electronic properties. The electron density integrated over a narrow energy region around E_F and projected over the mixed state is shown in Fig. 8.3(b). This is clearly localized over graphene and, to a smaller degree, over the Se atoms in contact to graphene. Since such state presents a dominating C-p_z and Se-p_z orbital contribution and it is delocalized in the plane of the interface, it presents π conjugation. A more quantitative insight is obtained by plotting the charge density averaged over planes parallel to the interface [Fig. 8.3(c)]. This shows that, while the contribution to the electron density originating from the bulk is small, a much larger por-

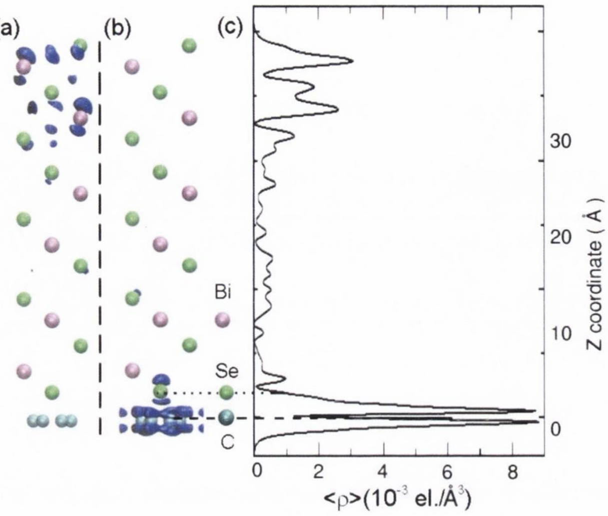

Figure 8.3: Charge density associated to the Bi_2Se_3 surface opposite to the graphene/Bi_2Se_3 interface (a) and the mixed interface state (b) obtained for $d = 2.2$ Å at Γ. Panel (c) shows the sum of the two charge densities averaged over a plane parallel to the interface.

tion is provided by the two surface states at both sides of the composite. At the free Bi_2Se_3 surface the surface state is distributed mainly over the first four atomic layers [Fig. 8.3(a)]. In contrast, at the graphene/Bi_2Se_3 interface the electron density migrates from the topological insulator to graphene. Notably this feature resembles closely the one reported for the interface between the normal metal Sb_2Se_3 and the topological insulator Bi_2Se_3 [121]. This behavior is similar to the topologization of ZnM (M=S, Se, Te) upon deposition on Bi_2Se_3 [114].

We now spend a few words on the possibility of inducing a topological state in graphene due to its proximity and bonding to Bi_2Se_3. Firstly, we wish to point out that our results do not indicate that graphene converts into a two-dimensional topological insulator upon its deposition on Bi_2Se_3, but simply that a topologically-protected hybrid state is formed. Here the Fermi surface of graphene undergoes a transition from a zero-band gap semiconducting phase (region C), prone to gap opening due to defects and impurities, to a topologically protected metallic phase (region A) via an insulating phase (region B). A fundamental property of three-dimensional topological insulators is the existence of an odd number of surface bands around E_F. Another property is that the topology of the surface states is such as to connect the bulk valence band to the conduction one due to the parity inversion originated by the strong spin-orbit coupling. In the graphene/Bi_2Se_3 complex only one conical band is present at the Fermi level. Importantly this band belongs to the surface state of Bi_2Se_3 with considerable contribution of graphene around E_F, while the other parts of the state (in particular the ends that connect to the valance and the conduction bulk topological states) still fully belong to Bi_2Se_3. Thus, the topologically protected surface state can be understood as a carrier of the induced graphene states, and the intrinsic topological protection of this state provides the robustness to graphene as well. Furthermore, the topologically-protected hybrid state does not simply correspond to the penetration of the one of the Bi_2Se_3 edge states into graphene. In that situation interaction between Bi_2Se_3 and graphene is not present. In contrast here the interaction is strong and, in fact, as d decreases first it is responsible for the opening of a band gap in graphene and then for creating the topologically-protected hybrid state. This behaviour is very similar to that of the Sb_2Se_3/Bi_2Se_3 [121] and the ZnM/Bi_2Se_3 (M=S, Se, Te) [114] interfaces, in which a topological state is transferred to the normal material because of proximity.

As a final characterization of the hybrid state we have probed its scattering properties. In particular, we have performed transport calculations, with the SMEAGOL code [77, 78, 79], for the composite along the direction parallel to the graphene sheet. Note that SMEAGOL provides an electronic structure for the composite essentially identical to that obtained with VASP.

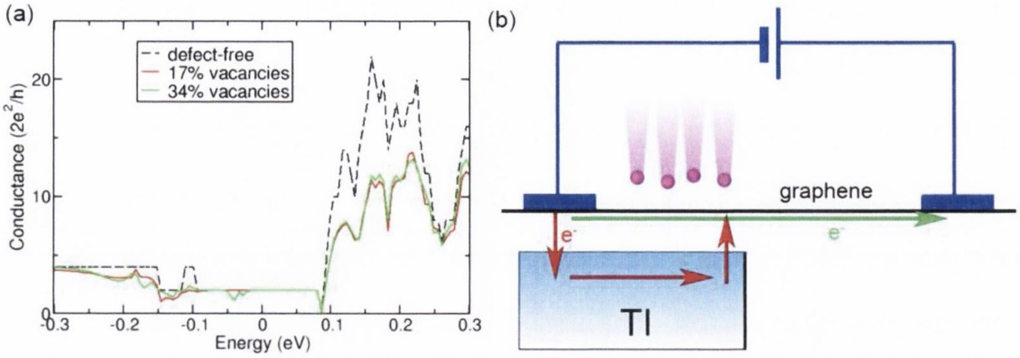

Figure 8.4: (a) Conductance of a Bi_2Se_3-contacted graphene sheet when either 17% or 33% C vacancies are introduced in graphene as compared to the conductance of a defect-free layer. (b) Schematic overview of a proposed experimental setup, which may prove the transfer of a topologically protected state from Bi_2Se_3 to graphene.

We have then calculated the system conductance for a defect-free system and for a the case where approximately 17% or 33% vacancies per supercell are introduced along the direction perpendicular to the transport [see Fig. 8.4(a)]. Note that these are extremely large concentrations and here they serve the purpose to prove the topological protection of the surface state. From Fig. 8.4(a) one can observe that 17% of vacancies do not affect the conductance around E_F indicating that the state is indeed strongly protected against back-scattering. Even for a 33% concentration little reduction of the conductance is found at around E_F, although the graphene layer is almost cut in two parts. Note, however, that the inclusion of impurities reduces significantly the conductance for energies away from the Fermi level, i.e., away from the topologically protected part of the graphene spectrum. This demonstrate that the transport is indeed through graphene and it is protected against back-scattering at around the Fermi level.

In concluding we would like to propose an experiment, which may prove the transfer of the topologically protected state to graphene. A schematic view of the proposed setup is shown in Fig. 8.4(b), in which a graphene sheet is contacted only in part to Bi_2Se_3 while the rest remains free-standing. Defects are then introduced in graphene only at the contacting region for instance by electrons or ions irradiation [122]. If there exists topological protection in graphene at the contact region, the electronic transport through such system will not show a conductance reduction relative to that of the defect-free case. One may still argue that the transport through the irradiated region is via the topologically protected surface state of Bi_2Se_3 rather than through the defective graphene. However, in this case the charge carriers need to hop between the topological insulator and the contacting graphene [red arrows in Fig. 8.4(b)] in order to continue their flow through the bare graphene and close the electric circuit. This will degrade the conductance. In contrast if the transport is carried solely by states of graphene (with defects) the effects of hopping will be eliminated by the proposed geometry setup.

Throughout this section we have presented results as a function of the graphene/Bi_2Se_3 distance, therefore we would like to close by briefly discussing what equilibrium distance one can expect. Unfortunately this turns out to be a difficult problem. The exact binding distance is determined by a balance between covalent and van der Waals forces. These latter ones are not captured by DFT local/semi-local exchange and correlation functionals and in fact we find that the two materials do not bind when the calculation is done at the generalized gradient approximation level. This contrasts reality where graphene/Bi_2Se_3 exists as it has been experimentally fabricated by few groups [117, 118, 119]. The inclusion of van der Waals forces at the level of local DFT [123] does not improve the situation, as screening prevents an accurate evaluation of the binding energy in layered compounds [124]. However we expect the equilibrium graphene/Bi_2Se_3 distance to be close to the sum of Se and C covalent radii, which amounts to 2 Å. This is within region A [see Fig.8.1(c)], i.e., when the hybrid surface state forms. Moreover external pressure may be introduced for tuning the desired separation.

8.1.3 Summary and Conclusions

In conclusion, we have investigated the electronic properties of graphene in contact with Bi_2Se_3. Three phases have been identified, depending on the graphene/Bi_2Se_3 separation. For $d > 3.0$ Å, the electronic structure of the composite is simply the superposition of those of the constituents. The second phase, obtained for 2.4 Å $\leq d \leq 3.0$ Å, witnesses the opening of a band gap in graphene, due to the annihilation of graphene states with opposite winding numbers. The third phase, when graphene and Bi_2Se_3 chemically bind, is the most interesting, as a topologically protected state with charge distribution mostly localized on graphene forms. This backscattering-free state may be utilized in graphene-based devices, for instance as an interconnect. Our results also demonstrate the more general principle of engineering interfaces between normal and topological materials to obtain desired functionalities.

8.2 Topological phase transition in three dimensional Dirac semimetals

In this section we study the interplay of surface and bulk Dirac states using first-principles density functional theory calculations and *ab initio* derived tight-binding models. Based on our first-principles calculations, we predict that the bulk Dirac cone for Na_3Bi is formed only for films with thickness greater than 90 nm, while the surface Dirac state, originating from a bulk band inversion, becomes gapless for films with a thickness as small as 4.5 nm. Furthermore, by employing the coherent potential approximation

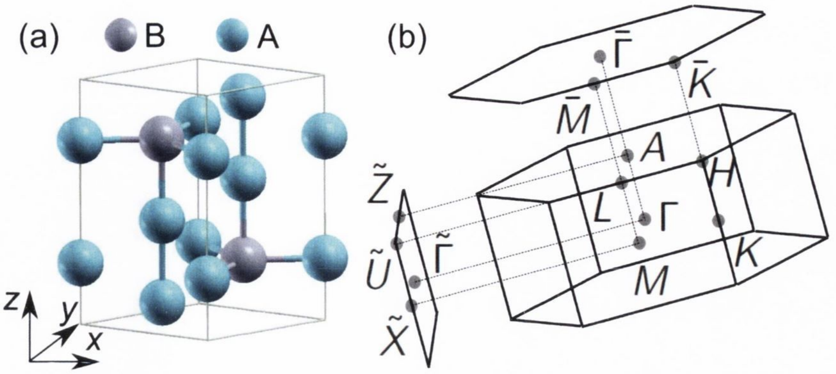

Figure 8.5: (a) Hexagonal unit cell for A_3B compounds, with A=Na, K, Rb and B=Bi, Sb. (b) Bulk and surface projected Brillouin zone for the structure with the high symmetry points marked. The three-dimensional Dirac crossing occurs along the $\Gamma - A$ direction.

in conjunction with DFT we uncover a topological phase transition in the $Na_3Bi_{1-x}Sb_x$ alloy. We propose a method to engineer the k space position of the bulk Dirac point by changing the Sb concentration. At a critical Sb concentration of $\approx 50\%$, this crossing reaches the Brillouin zone (BZ) center, meeting its time-reversed partner, whereupon they annihilate and render the bulk gapped. This topological phase transition is accompanied by a simultaneous loss of the inverted band character. Beyond this Sb concentration the alloy is adiabatically connected to the topologically trivial Na_3Sb.

8.2.1 Computational Details

We have carried out first-principles calculations using the projector augmented plane wave method as implemented in Vienna Ab initio Simulation Package (VASP) [81]. We have used the Perdew-Burke-Ernzerhof parameterization of the exchange-correlation functional. Spin-orbit coupling was included for all computations in the self-consistent calculation. The electronic structure simulations were performed with a plane wave cutoff of 600 eV on a $8\times8\times4$ Monkhorst-Pack k-point mesh. All A_3B compounds (A=Na, K, Rb, B=Bi, Sb) investigated here crystallize in the hexagonal structure,

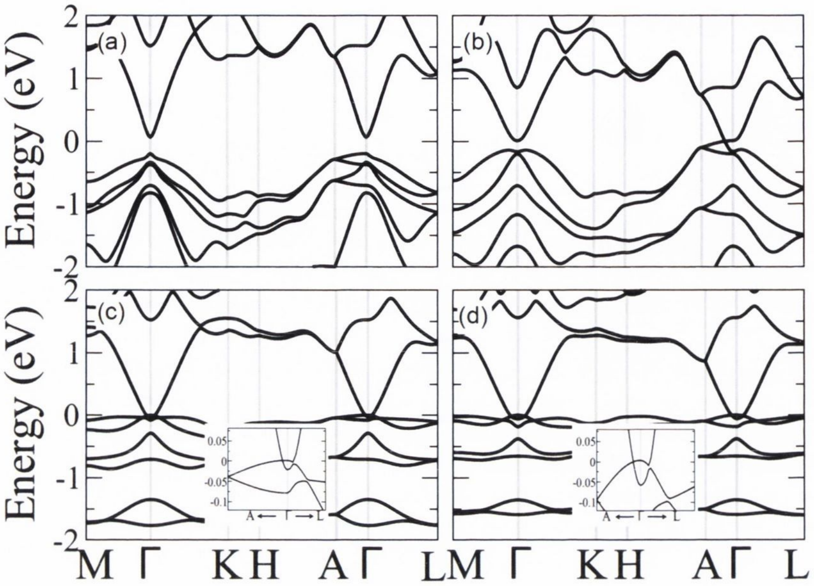

Figure 8.6: Bulk band structures including spin-orbit interaction for (a) Na_3Sb, (b) Na_3Bi, (c) K_3Bi and (d) Rb_3Bi. Note the Dirac crossing in (b)-(d). The insets in (c) and (d) show a zoom around Γ with the crossing along $\Gamma - A$.

as shown in Fig. 8.5. During structural optimization the atomic coordinates were allowed to relax until total energy differences were less than 1 meV. From the bulk first-principles results, we projected onto a basis of Na $3s$ and Bi $6p$ (Sb $5p$) orbitals by using a maximally localized wannier function scheme [134]. These tight-binding parameters were then used to study slab geometries. By combining this scheme with a coherent potential approximation (CPA) including self-energy corrections for disorder interaction, we have investigated the $Na_3Bi_{1-x}Sb_x$ alloy [135]. We note that this methodology has been recently used to predict the robustness of Dirac fermions in topological crystalline insulator alloys, as well as in ferroelectric Rashba semiconductor alloys [136]. In Appendix E of this thesis we provide a discussion of the Coherent Potential Approximation in the context of a tight-binding model.

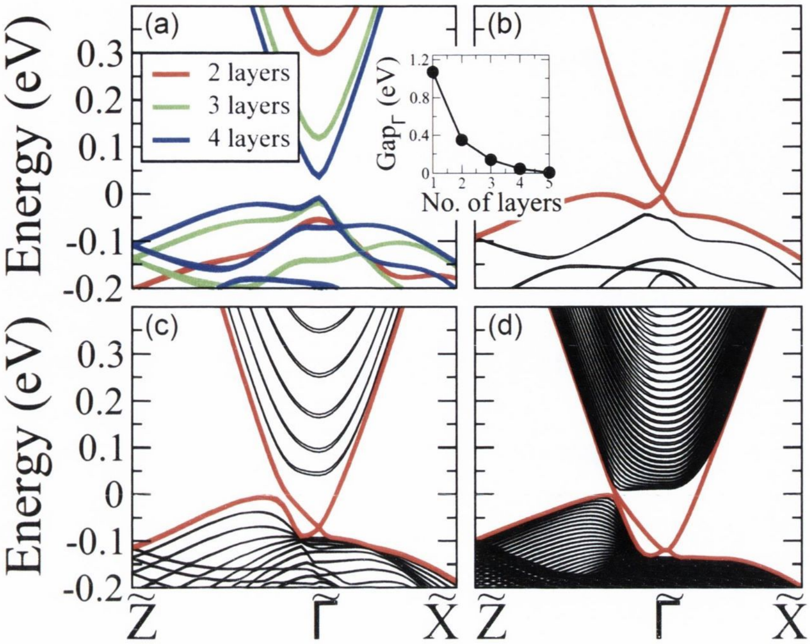

Figure 8.7: Band structures for Na_3Bi thin films of thickness (a) 2-4 layers, (b) 5 layers, (c) 20 layers and (d) 100 layers. Inset in (a)-(b) shows the energy gap at the center of the Brillouin zone for slabs of thickness 1 to 5 layers. In (b)-(d) Dirac crossings are highlighted in red.

8.2.2 Results

We begin our analysis by calculating the relativistic bulk band structures for the four materials Na_3Sb, Na_3Bi, K_3Bi and Rb_3Bi, as shown in Fig. 8.6. For Na_3Bi we find the three-dimensional Dirac crossing along the $\Gamma - A$ line, and a band inversion at the BZ center, which is consistent with the previous study of Wang *et al.* [126]. Na_3Sb, on the other hand, is a small gap insulator with a conventional band ordering. Our calculations reveal that on replacing Na in Na_3Bi with heavier atoms, the resulting compounds K_3Bi and Rb_3Bi are metallic with small electron pockets around Γ, however the crossing away from Γ is still present. The band structures for the two materials are shown in Fig. 8.6(c) and (d), along with a zoom around the BZ center in the insets.

Since Na_3Bi also shows an inverted band character around the Fermi level, one expects it to form surface states when confined into a two-dimensional geometry, similar to topological insulators. Therefore, we study the evolution of the spectrum of films of Na_3Bi oriented along the [010] surface, as a function of their thickness. For thickness from 1 to 4 layers, the films are gapped due to an interaction between the two surfaces, as shown in Fig. 8.7(a). This gap decreases monotonically, with the surface cone at $\widetilde{\Gamma}$ becoming gapless for a 5-layer-thick film. One can also notice the shoulder along the $\widetilde{\Gamma} - \widetilde{Z}$ direction, which rises upwards in energy to form the bulk Dirac crossing for thicker films. This bulk crossing is fully formed only for film thicknesses larger than 100 layers ($\approx$ 90 nm). Our predictions for the thickness dependence of the surface and bulk Dirac cones call for verification by angle resolved photoemission experiments. Indeed, such measurements with varying film thickness have been recently undertaken for topological insulator films [137, 138]. In the case of Na_3Bi [010] slabs, one should be able to see two gap-closing transitions at very different film thicknesses: one for the surface cone for a few layers slab, with the next gap-closing occurring in the bulk for a hundred layers slab. Very recently thin films of Na_3Bi have been grown by molecular beam epitaxy [139], a development which provides a clear route to verify our predictions.

Now we turn our attention to the $Na_3Bi_{1-x}Sb_x$ alloy. From the bulk band structures in Fig. 8.6, we observe that Na_3Sb is topologically trivial, having neither the bulk Dirac crossing nor a band inversion at the BZ center, as opposed to Na_3Bi. This opens up the intriguing possibility to obtain a quantum phase transition in $Na_3Bi_{1-x}Sb_x$ solid solutions. To this end, we have performed DFT+CPA calculations for the alloy. The spectral functions at different Sb concentration are shown in Fig. 8.8. With increasing Sb concentration, the bulk Dirac crossing along $\Gamma - A$ moves towards the BZ center. At around a critical concentration of $x_c = 0.5$ ($Na_3Bi_{0.5}Sb_{0.5}$), this crossing

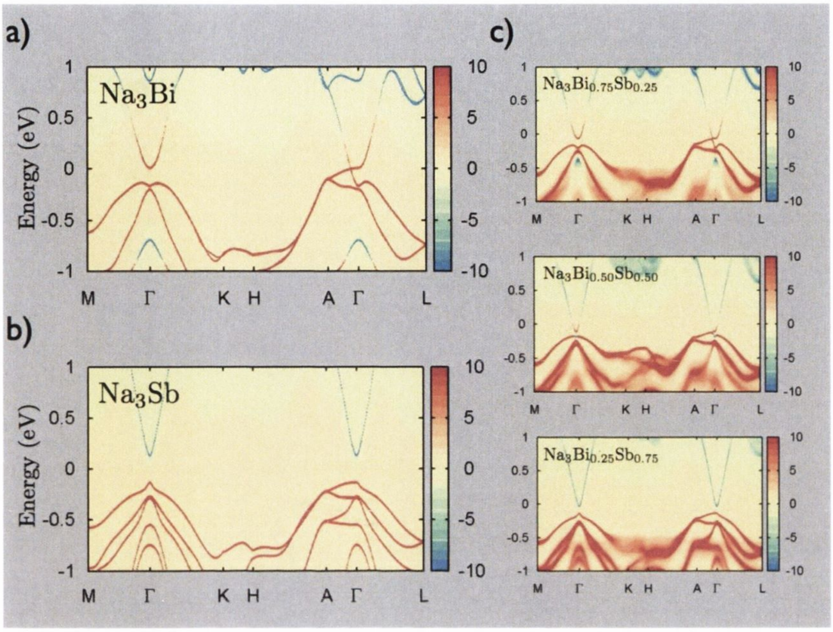

Figure 8.8: Spectral functions for pristine (a) Na$_3$Bi and (b) Na$_3$Sb. (c) Spectral functions for the alloy Na$_3$Bi$_{1-x}$Sb$_x$ with increasing Sb concentration ($x = 0.25, 0.50, 0.75$ from top to bottom). The color scale shows the orbital contribution, with red (positive values) denoting Bi/Sb p orbitals and blue (negative values) representing Na s orbital (in units of states/eV).

reaches close to Γ. Upon subsequent increase in Sb concentration, an energy gap appears. We note that this is the consequence of the annihilation between this Dirac cone and its time reversed partner along Γ to $-A$ direction. The Sb concentration therefore represents an efficient tool to manipulate the position of the bulk Dirac points in k space along the $\Gamma - A$ line. Interestingly, the disappearance of the bulk cone is accompanied by a loss of the inverted band character, as can be evidenced from the reversal in orbital character of the valence and conduction bands, before and after passing through the critical Sb concentration. From bulk-boundary correspondence, one can then infer that for slabs made of these alloys there would also be transition in the surface spectrum: below x_c the surface would display a Dirac crossing, while increasing Sb concentration beyond this value would lead to opening of a trivial gap. Thus, our calculations reveal a topological phase transition in the prototypical three-dimensional Dirac semimetal. Recently, such tunable phase transitions were experimentally reported for topological insulators and topological crystalline insulators [140, 141, 142, 143]. This makes us confident that our predictions can be verified in the near future. It is also worthy of consideration that our DFT+CPA calculations reveal a protection, against substitutional disorder, of the spectral features of three-dimensional Dirac semimetals around the Fermi level. We note, in fact, the absence of broadening of spectral features around the cone, as compared to other energies. Such a robustness, similar to what happens for topological crystalline insulators and Weyl fermion systems, arises from the three-dimensional nature of the Dirac cone [136], and in turn leads to the concrete possibility of experimental verification by means of spectroscopic techniques. As shown in Ref. [136], this is a consequence of a vanishing disorder self-energy around the crossing point. We also propose that a similar phase transition, and a similar robustness against disorder, would occur in the $Cd_3(As_{1-x}P_x)_2$ alloy, since the parent compounds Cd_3As_2 and Cd_3P_2 are Dirac semimetal and conventional insulator, respectively, with the former having an inverted band order and the latter having a normal band sequence.

8.2.3 Summary and Conclusions

In summary, we have studied the interplay of bulk and surface Dirac fermions in prototypical three-dimensional Dirac semimetals, using first-principles based tight-binding calculations. Furthermore, by means of density functional theory with coherent potential approximation simulations, we have revealed a topological phase transition in $Na_3Bi_{1-x}Sb_x$. The tuning of Sb the concentration provides an efficient way to engineer the reciprocal space position of the three-dimensional Dirac cone, with potential implications for technological devices benefiting from this additional degree of freedom. Intriguingly, the phase transition from a Dirac semimetal to an insulator is accompanied by a change in the bulk band ordering. This can be related, via the bulk-boundary correspondence, to a concomitant transition in the surface state spectrum. Around the Dirac crossing, we found a robustness of the spectral features against substitutional disorder. This indicates that our predictions could be readily verified using existing spectroscopic methods.

Chapter 9

Conclusions and outlook

In this thesis we studied different facets of topological states in two and three dimensions, employing both model Hamiltonians as well as material specific first principles calculations. Here we summarize our findings and discuss possible future directions.

Our discussion began in Chapter 2, where we introduced the basic notions of topology in the band picture. Here we also discussed the Kane-Mele model, the prototypical lattice model for $\mathbb{Z}_2$ topological insulator, which was used for some subsequent studies in this work. Chapter 3 provided an overview of the main methods used in this thesis: density functional theory to tackle the many body problem and the non-equilibrium Green's function approach to the quantum transport problem.

In Chapter 4, we presented our results for Andreev reflection at two-dimensional topological insulator-superconductor junction. We compared and contrasted our results for $\mathbb{Z}_2$ and Chern insulators. On the basis of this analysis, we proposed a tabletop transport experiment to distinguish between the two kinds of topological insulators.

Given the peculiar spin structure of the quantum spin Hall edge states, a natural question arises whether it can be used to manipulate magnetic objects. In Chapter 5 we answered this question in the affirmative. By using the non-equilibrium Green's function method for transport combined with a perturbative approach to spin-scattering from magnetic impurities, we showed that a magnetic impurity deposited at the edge of a $\mathbb{Z}_2$ topological insulator and presenting a uniaxial magnetic anisotropy, can be manipulated by the quantum spin Hall edge current. Furthermore, we showed that the topological nature of the edge states has profound consequences on the spin flip inelastic electron tunneling conductance spectrum. At low current intensity there is a complete suppression of the conductance steps appearing at the critical biases characteristic of the activation of an inelastic spin-scattering channel. In contrast, for currents large enough to produce spin pumping the spin of the magnetic impurity is driven away from the anisotropy axis. This breaks the topological protection of the helical edge states and the conductance steps reappear. We also proposed a four-terminal device designed to manipulate, by all electrical means, the spin of a magnetic adatom positioned at the edge of a two-dimensional $\mathbb{Z}_2$ topological insulator.

Next we moved on to *ab initio* transport investigations of topological materials. In Chapter 6 we reported our study of surface states on the Sb(111) surface. We calculated the transport properties across surface barriers and directly compared to scanning tunneling microscopy experiments. An excellent agreement was obtained, in particular, for lifetimes of quantum well states and the allowed scattering processes. We also presented our large scale *ab initio* calculations on analogous steps on Bi_2Se_3(111) surface, which revealed that backscattering is completely suppressed for normal incidence, while scattering is allowed at all other incidence angles. We also constructed a potential barrier model based on the often used Dirac Hamiltonian. A comparison with our first principles results revealed the shortcomings of such a model.

In Chapter 7 we presented our findings demonstrating a single atom anisotropic magnetoresistance on topological insulator surface. This stems from an interplay between the helical surface states and spin anisotropy of the magnetic adatom. This is a novel type of MR, which does not need any magnetic electrodes, but requires a magnetic adatom, or more generally adsorbed magnetic clusters or thin films. Our first principles calculations revealed the underlying mechanism and we complemented our findings with a two-dimensional model. This led us to propose a device setup suitable for experimental realization.

In Chapter 8 we turned our attention to two- and three- dimensional Dirac semimetals. We showed how the proximity to a topological insulator leads to a backscattering protected hybrid state in graphene. This state possesses helical spin momentum locking and a robustness to disorder, which we investigated by employing transport calculations. We reported our studies of the interplay between bulk and surface Dirac fermions in prototypical three dimensional Dirac semimetals. By means of density functional theory with coherent potential approximation computations, we revealed a topological phase transition in $Na_3Bi_{1-x}Sb_x$ alloy. We showed that changing the Sb concentration also provides a way to engineer the reciprocal space position of the three-dimensional Dirac cone, with possibilities for devices benefiting from this additional degree of freedom.

Finally we wish to mention a few possible directions, which can be investigated in future. For the Andreev reflection problem, an interesting extension would be to study it by taking into account the realistic electronic structure from first-principles. A first step along this direction has already been taken by implementing the phenomenology of Andreev reflection in the density functional theory based transport code SMEAGOL, employing an extended Blonder-Tinkham-Klapwijk model. This can be used to study Andreev reflection in three-dimensional variant of the problem as well. Finally this approach may also be used to model experimental setups in large spin-orbit nanowires, where possible signatures of Majorana fermions have been recently observed. For inelastic electron tunneling spectroscopy, a possible direction for future investigations would be coupling of more than one spin, both at the same edge as well as between different edges in narrow-width ribbons. Inelastic electron tunneling spectroscopy of three-dimensional topological insulators would also be a natural extension of the work presented in this thesis. Our analysis of unusual magnetoresistance obtained on topological insulator surface also points to interesting possibilities for spin transfer torque exerted by a topological insulator substrate on a magnetic layer. A large spin-orbit coupling along with a spin-momentum locking of surface electrons could possibly lead to interesting effects on the spin transfer torque, which warrant future studies. In the investigation of graphene/Bi_2Se_3 system, van der Waals interaction is expected to play a crucial role in determining the equilibrium geometry. A systematic study of the effect of van der Waals interaction in this system is lacking and merits further attention. The study of three-dimensional Dirac semimetals is a field that has been growing rapidly. At the time of the writing of this thesis, only two materials are known to harbour this bulk three-dimensional Dirac cone. A thorough search for more materials in this class would be worth pursuing in the future.

Appendix A

Quantization of the Chern number

In this Appendix we clarify how the Chern number may be viewed as an obstruction to a smooth gauge choice of the Bloch wavefunction in the Brillouin zone (BZ) and prove its quantization, following Ref. [18]. The Chern number is an integral of the Berry curvature over the BZ. The Berry curvature itself can be expressed as the curl of a Berry vector potential, $\mathbf{A}$. The BZ has no boundaries as it is a torus (a compact manifold). If one now applies Stokes' theorem, then the Chern number is written as the integral of $\mathbf{A}(k)$ over the boundary of the BZ. Since there is no boundary, it would identically be equal to zero, unless $\mathbf{A}(k)$ has singularities in the BZ.

Consider a $U(1)$ gauge transformation of the wavefunction of the n-th energy level

$$|n, k\rangle' = e^{if(k)}|n, k\rangle, \tag{A.1}$$

where f is a smooth function defined over the BZ. The transformed vector potential reads ($\mathbf{A}(k) = \langle\psi(k)|\nabla_{\mathbf{k}}|\psi(k)\rangle$):

$$\mathbf{A}_n(k)' = \mathbf{A}_n(k) + \nabla f(k). \tag{A.2}$$

Since the Chern number is directly proportional to the Hall conductance, which is an observable, it must be gauge invariant. Now, consider a specific gauge choice where we choose $f(k)$ such that the first component of the eigenvector $|n,k\rangle$ is real, i.e., we set $e^{if(k)} = ||n,k\rangle_1|/|n,k\rangle_1$. If such a smooth gauge could always be found then the Chern number would always be zero. When this first component of the Bloch eigenstate becomes zero, then clearly such a gauge choice is not possible. Suppose this happens at N points $k_s = k_1, ..., k_N$. Define neighbourhoods R_s^ϵ around these such that $|k - k_s| < \epsilon$. If one now picks a different phase convention in these regions: $|n,k\rangle_2$ is real. At the boundaries between such regions the wavefunctions are related as

$$\psi_2(k) = e^{i(g(k)-f(k))}\psi_1(k) = e^{i\chi(k)}\psi_1(k), \tag{A.3}$$

while the vector potentials are related as

$$\mathbf{A}_2(k) = \psi_2\nabla_{\mathbf{k}}\psi_2 = \psi_1\nabla_{\mathbf{k}}\psi_1 + i\nabla\chi(k) = \mathbf{A}_1(k) + i\nabla\chi(k). \tag{A.4}$$

The Hall conductance is then

$$\sigma_{xy} = \frac{e^2}{h}\frac{1}{2\pi i}\left(\int_{BZ-R_s^\epsilon} \nabla\times\mathbf{A}_1(k) + \int_{R_s^\epsilon} \nabla\times\mathbf{A}_2(k)\right), \tag{A.5}$$

and by applying Stokes' theorem we get

$$\sigma_{xy} = \frac{e^2}{h}\frac{1}{2\pi i}\left(\int_{\partial(BZ-R_s^\epsilon)} d\mathbf{k}\cdot\mathbf{A}_1(k) + \int_{\partial(R_s^\epsilon)} d\mathbf{k}\cdot\mathbf{A}_2(k)\right). \tag{A.6}$$

Since the torus does not have a boundary $\partial(BZ - R_s^\epsilon) = -\partial(R_s^\epsilon)$ and the Hall conductance simplifies to

$$\begin{aligned}\sigma_{xy} &= \frac{e^2}{h}\frac{1}{2\pi i}\int_{\partial(R_s^\epsilon)} d\mathbf{k}\cdot(\mathbf{A}_1(k) - \mathbf{A}_2(k))\\ &= \frac{e^2}{h}\frac{1}{2\pi i}\int_{\partial(R_s^\epsilon)} dk\cdot i\nabla\chi(k)\\ &= \frac{e^2}{h}n,\end{aligned} \tag{A.7}$$

where $n = \frac{1}{2\pi}\oint_{\partial(R_s^\epsilon)} dk\cdot\nabla\chi(k)$. For simplicity, consider the boundary of the R_s^ϵ regions as a circle $\partial(R_s^\epsilon) = k_s + \epsilon e^{i\theta}$ (where $\theta \in [0, 2\pi)$), then

$$n = \frac{1}{2\pi}\left[\chi(k_s + \epsilon e^{2\pi i - 0^-}) - \chi(k_s + \epsilon)\right]. \tag{A.8}$$

Here n has to be integer since along a complete path around the circular R_s^ϵ the wavefunction must come back to itself:

$$\begin{aligned}\psi_2(k_s+\epsilon) &= e^{i\chi(k_s+\epsilon)}\psi_1(k_s+\epsilon)\\ &= \psi_2(k_s+\epsilon e^{i(2\pi-0^-)})\\ &= e^{i\chi(k_s+\epsilon e^{i(2\pi-0^-)})}\psi_1(k_s+\epsilon e^{i(2\pi-0^-)})\\ &= e^{i\chi(k_s+\epsilon e^{i(2\pi-0^-)})}\psi_1(k_s),\end{aligned} \tag{A.9}$$

which requires that $\chi(k_s + \epsilon e^{i(2\pi-0^-)}) - \chi(k_s + \epsilon) = 2m\pi$.

Appendix B

A brief note on Pfaffians

The determinant of every skew-symmetric matrix can always be written as the square of a polynomial of the matrix elements.

$$\det(A) = [\mathrm{Pf}(A)]^2, \tag{B.1}$$

where $\mathrm{Pf}(A)$ denotes the Pfaffian of the matrix A. The sign of the Pfaffian is ambiguous due to the ambiguity in defining the sign of the square root. It is non-zero only for even dimensional matrices. For example:

$$\mathrm{Pf}\begin{pmatrix} 0 & a \\ -a & 0 \end{pmatrix} = a. \tag{B.2}$$

Using this, a recursion relation can be employed to find Pfaffians of any matrix

$$\mathrm{Pf}(A) = \sum_{j=2}^{2N} (-1)^j a_{1j} \mathrm{Pf}(A_{1j}), \tag{B.3}$$

where A_{ij} is the matrix A with first and j-th rows and columns removed. Some useful Pfaffian identities are:

$$\begin{aligned}\mathrm{Pf}[xAx^T] &= \det(x)\mathrm{Pf}(A)\\ \mathrm{Pf}[A^T] &= (-1)^N\mathrm{Pf}(A)\\ \mathrm{Pf}[\lambda A] &= \lambda^N\mathrm{Pf}(A),\end{aligned}\tag{B.4}$$

where x is any $2N \times 2N$ matrix and λ is a scalar. Finally,

$$\mathrm{Pf}\begin{pmatrix} 0 & \lambda_1 & 0 & 0 & \cdots & 0 & 0\\ -\lambda_1 & 0 & 0 & 0 & \cdots & 0 & 0\\ \vdots & \vdots & \vdots & \ddots & \vdots & \vdots & \vdots\\ 0 & 0 & 0 & 0 & 0 & 0 & \lambda_N\\ 0 & 0 & 0 & 0 & 0 & -\lambda_N & 0\end{pmatrix} = \lambda_1 \ldots \lambda_N. \tag{B.5}$$

These identities are used while deriving the $\mathbb{Z}_2$ invariant expression from time reversal polarization.

Appendix C

Blonder-Tinkham-Klapwijk model and Andreev reflection

Consider a normal (N) - superconductor (S) junction which is located at $z = 0$. Using the Bogoliubov-de Gennes equation

$$\begin{pmatrix} H - E_F & \Delta \\ \Delta^* & E_F - \mathcal{T}H\mathcal{T}^{-1} \end{pmatrix} \begin{pmatrix} u \\ v \end{pmatrix} = E \begin{pmatrix} u \\ v \end{pmatrix}, \tag{C.1}$$

where H is the particle Hamiltonian, E_F is the Fermi level, Δ is the pairing potential and $\mathcal{T}$ is the time-reversal operator (for a time-reversal symmetric system its action is to yield the complex conjugate of the Hamiltonian, i.e., $\mathcal{T}H\mathcal{T}^{-1} = H^*$). Here u and v are the particle and hole wavefunctions, respectively. The junction is modeled using a step function for the order parameter

$$\Delta(z) = \theta(z)\Delta e^{i\phi}. \tag{C.2}$$

If we assume that the system is separable along the transport (z) and perpendicular to the transport direction, then the wavefunction can be factorized as

$$\Psi(x,y,z) = \psi(z)\Phi(x,y). \tag{C.3}$$

The transverse modes satisfy

$$\left[-\frac{\hbar^2}{2m}\left(\frac{\partial^2}{\partial x^2}+\frac{\partial^2}{\partial y^2}\right)+V(x,y)\right]\Phi(x,y) = E_\perp\Phi(x,y). \tag{C.4}$$

Along transport direction we are left with a one-dimensional problem. In order to model the effects of a contact resistance at the interface include a $\Lambda\delta(z)$ potential, giving

$$\begin{pmatrix} -\frac{\hbar^2}{2m}\frac{\partial^2}{\partial z^2} - E_F + \Lambda\delta(z) & \Delta(z) \\ \Delta^*(z) & \frac{\hbar^2}{2m}\frac{\partial^2}{\partial z^2} + E_F - \Lambda\delta(z) \end{pmatrix}\begin{pmatrix} u(z) \\ v(z) \end{pmatrix} = E\begin{pmatrix} u(z) \\ v(z) \end{pmatrix}. \tag{C.5}$$

This is the Blonder-Tinkham-Klapwijk model [47]. On the normal side the equation reduces to

$$\begin{pmatrix} -\frac{\hbar^2}{2m}\frac{\partial^2}{\partial z^2} - E_F & 0 \\ 0 & \frac{\hbar^2}{2m}\frac{\partial^2}{\partial z^2} + E_F \end{pmatrix}\begin{pmatrix} u(z) \\ v(z) \end{pmatrix} = E\begin{pmatrix} u(z) \\ v(z) \end{pmatrix}, \tag{C.6}$$

whose solutions are

$$\Psi^e_\pm = \begin{pmatrix} 1 \\ 0 \end{pmatrix} e^{\pm ik_e z}, \quad \Psi^h_\pm = \begin{pmatrix} 0 \\ 1 \end{pmatrix} e^{\pm ik_h z}, \tag{C.7}$$

where $k_e = k_F\sqrt{1+E/E_F}$, $k_h = k_F\sqrt{1-E/E_F}$ and $k_F = \frac{\sqrt{2mE_F}}{\hbar}$. On the superconductor side, we have

$$\begin{pmatrix} -\frac{\hbar^2}{2m}\frac{\partial^2}{\partial z^2} - E_F & \Delta e^{i\phi} \\ \Delta e^{-i\phi} & \frac{\hbar^2}{2m}\frac{\partial^2}{\partial z^2} + E_F \end{pmatrix} \begin{pmatrix} u(z) \\ v(z) \end{pmatrix} = E \begin{pmatrix} u(z) \\ v(z) \end{pmatrix}. \tag{C.8}$$

For propagating waves ($E > \Delta_0$) the above yields,

$$\Psi^e_\pm = \sqrt{\frac{\Delta}{2E}} \begin{pmatrix} e^{\frac{1}{2}\cosh^{-1}(E/\Delta)} e^{i\phi/2} \\ e^{-\frac{1}{2}\cosh^{-1}(E/\Delta)} e^{-i\phi/2} \end{pmatrix} e^{\pm i q_e z}, \quad \Psi^h_\pm = \begin{pmatrix} e^{-\frac{1}{2}\cosh^{-1}(E/\Delta)} e^{i\phi/2} \\ e^{\frac{1}{2}\cosh^{-1}(E/\Delta)} e^{-i\phi/2} \end{pmatrix} e^{\pm i q_h z}, \tag{C.9}$$

where $q_e = k_F\sqrt{1 + \sqrt{(E^2 - \Delta^2)/E_F^2}}$, $q_h = k_F\sqrt{1 - \sqrt{(E^2 - \Delta^2)/E_F^2}}$ and $k_F = \frac{\sqrt{2mE_F}}{\hbar}$.

In contrast, for evanescent waves we have

$$\Psi^e_\pm = \sqrt{\frac{\Delta}{2E}} \begin{pmatrix} e^{\frac{i}{2}\cos^{-1}(E/\Delta)} e^{i\phi/2} \\ e^{-\frac{i}{2}\cos^{-1}(E/\Delta)} e^{-i\phi/2} \end{pmatrix} e^{\pm i q_e z}, \quad \Psi^h_\pm = \begin{pmatrix} e^{-\frac{i}{2}\cos^{-1}(E/\Delta)} e^{i\phi/2} \\ e^{\frac{i}{2}\cos^{-1}(E/\Delta)} e^{-i\phi/2} \end{pmatrix} e^{\pm i q_h z}, \tag{C.10}$$

where $q_e = k_F\sqrt{1 + i\sqrt{(\Delta^2 - E^2)/E_F^2}}$, $q_h = k_F\sqrt{1 - i\sqrt{(\Delta^2 - E^2)/E_F^2}}$. They have acquired an imaginary part in addition to the real part. The matching condition at the boundary is obtained by integrating the equation

$$-\frac{\hbar^2}{2m}\frac{\partial^2 u(z)}{\partial z^2} - E_F u(z) + \Lambda(z)u(z) + \Delta(z)v(z) = Eu(z), \tag{C.11}$$

around $z = 0$, to yield

$$\partial_z u(0^+) - \partial_z u(0^-) = \frac{2m\Lambda}{\hbar^2} u(0), \tag{C.12}$$

$$\partial_z v(0^+) - \partial_z v(0^-) = \frac{2m\Lambda}{\hbar^2} v(0). \tag{C.13}$$

The analysis of the scattering process proceeds by considering incidence from the normal side

$$\Psi_{inc}(z) = \frac{1}{\sqrt{2\pi\hbar v_e}} \begin{pmatrix} 1 \\ 0 \end{pmatrix} e^{ik_e z}. \tag{C.14}$$

The wave reflected back is a sum of left moving electron and a left moving hole

$$\Psi_{ref}(z) = \frac{r_{ee}}{\sqrt{2\pi\hbar v_e}} \begin{pmatrix} 1 \\ 0 \end{pmatrix} e^{-ik_e z} + \frac{r_{he}}{\sqrt{2\pi\hbar v_h}} \begin{pmatrix} 0 \\ 1 \end{pmatrix} e^{+ik_h z}. \tag{C.15}$$

The transmitted wave is a right moving electron and a right moving hole

$$\Psi_{trans}(z) = \frac{t_{ee}}{\sqrt{2\pi\hbar w_e}} \begin{pmatrix} u_0 e^{i\phi/2} \\ v_0 e^{-i\phi/2} \end{pmatrix} e^{+iq_e z} + \frac{t_{he}}{\sqrt{2\pi\hbar w_h}} \begin{pmatrix} v_0 e^{i\phi/2} \\ u_0 e^{-i\phi/2} \end{pmatrix} e^{-iq_h z}, \tag{C.16}$$

where $u_0 = \sqrt{\frac{\Delta}{2E}} e^{\frac{1}{2}\cosh^{-1}(E/\Delta)}$, $v_0 = \sqrt{\frac{\Delta}{2E}} e^{-\frac{1}{2}\cosh^{-1}(E/\Delta)}$ for propagating waves and $u_0 = \sqrt{\frac{\Delta}{2E}} e^{\frac{i}{2}\cos^{-1}(E/\Delta)}$, $v_0 = \sqrt{\frac{\Delta}{2E}} e^{-\frac{i}{2}\cos^{-1}(E/\Delta)}$ for evanescent waves. The coefficient r_{ee} denotes reflection from electron to electron, r_{he} denotes reflection from electron to hole, t_{ee} denotes transmission from electron to electron, and t_{he} denotes transmission from electron to hole. The wavefunctions are normalized by their group velocities

$$v_e = \frac{1}{\hbar}\frac{dE}{dk_e} = \frac{\hbar k_e}{m}, \quad v_h = \frac{1}{\hbar}\frac{dE}{dk_h} = \frac{\hbar k_h}{m}, \tag{C.17}$$

on the normal side. On the superconductor side we have

$$w_e = \frac{1}{\hbar}\frac{dE}{dq_e} = \frac{\hbar q_e}{m}, \quad w_h = \frac{1}{\hbar}\frac{dE}{dq_h} = \frac{\hbar q_h}{m}. \tag{C.18}$$

We also have the relations

$$w_{e/h} = \frac{\sqrt{E^2 - \Delta^2}}{E} v_{e/h} = (u_0^2 - v_0^2) v_{e/h}. \tag{C.19}$$

Continuity of the wavefunction and its derivative implies

$$u(0^+) = u(0^-), \quad v(0^+) = v(0^-), \tag{C.20}$$

and

$$\partial_z u(0^+) - \partial_z u(0^-) = \frac{2m\Lambda}{\hbar^2} u(0), \quad \partial_z v(0^+) - \partial_z v(0^-) = \frac{2m\Lambda}{\hbar^2} v(0). \tag{C.21}$$

Next we assume that

$$E, \Delta \ll E_F, \tag{C.22}$$

which is the Andreev approximation. This leads to the following simplifications

$$k_{e/h} \approx q_{e/h} \approx k_F, \tag{C.23}$$

$$v_{e/h} \approx v_F, \quad w_{e/h} \approx (u_0^2 - v_0^2) v_F, \tag{C.24}$$

where $v_F = \frac{\hbar k_F}{m}$. Simple, but tedious algebra yields

$$r_{ee} = \frac{(Z^2 + iZ)(v_0^2 - u_0^2)}{u_0^2 + Z^2(u_0^2 - v_0^2)}, \tag{C.25}$$

$$r_{he} = \frac{u_0 v_0}{u_0^2 + Z^2(u_0^2 - v_0^2)} e^{-i\phi}, \tag{C.26}$$

$$t_{ee} = \frac{(1 - iZ)u_0\sqrt{u_0^2 - v_0^2}}{u_0^2 + Z^2(u_0^2 - v_0^2)} e^{-i\phi/2}, \tag{C.27}$$

$$t_{he} = \frac{iZv_0\sqrt{u_0^2 - v_0^2}}{u_0^2 + Z^2(u_0^2 - v_0^2)} e^{-i\phi/2}. \tag{C.28}$$

Here $Z = \frac{\Lambda}{\hbar v_F}$ is a dimensionless parameter which measures the interface transparency. $Z \ll 1$ gives a very transparent interface while $Z \gg 1$ yields a low transparency. If we now simplify to the case of perfectly ideal interface, i.e., $Z = 0$. In this case

$$\begin{aligned} r_{he} = \frac{v_0}{u_0} e^{-i\phi} &= e^{-i\phi} e^{-i\cos(E/\Delta)} \quad E < \Delta \\ &= e^{-i\phi} e^{-\cosh(E/\Delta)} \quad E > \Delta. \end{aligned} \tag{C.29}$$

So, the probability amplitude $|r_{he}|^2 = 1$ for $E < \Delta$. This shows that for an ideal N-S interface, an injected electron is reflected back as a hole with unit probability. This phenomenon is called Andreev reflection [41, 48]. In contrast to usual reflection, where momentum is not conserved and charge is conserved, in Andreev reflection momentum is conserved (at least in the Andreev approximation), whereas charge is not conserved. For $E > \Delta$, the electron also has finite probability to be transmitted as an electron since there are states available in the superconductor, above the superconducting gap.

Appendix D

Perturbation expansion in electron-spin coupling

In Chapter 5, we discussed the possibility to manipulate the spin of an adatom at the edge of a two-dimensional topological insulator, based on a perturbation expansion in the electron-spin coupling. In this appendix we provide the details of such a perturbation expansion. The electron-spin interaction term in the Hamiltonian is

$$H_{e-sp} = J_{sd} \sum_{\alpha,\beta'} (c^{\dagger}_{\alpha}[\sigma]_{\alpha\beta} c_{\beta}) \cdot \mathbf{S} + \epsilon_0 \sum_{\alpha} c^{\dagger}_{\alpha} c_{\alpha}. \tag{D.1}$$

Here the first term is the interaction between the localized spin $\mathbf{S}$ and the conducting electrons, while the second term represents the elastic contribution to the scattering and is called the magnetoresistive elastic term. This interacting problem is insoluble directly. However, here we summarize the perturbation expansion used to tackle it. This was derived in Refs. [64, 66] following the procedure laid out in Ref. [67]. Considering zero temperature, the contour ordered spin-dependent single-body Green's function in the many-body ground state is defined as,

$$[G(\tau,\tau')]_{\sigma,\sigma'} = -i\langle|T_C\{c_\sigma(\tau)c^\dagger_{\sigma'}(\tau')\}|\rangle, \tag{D.2}$$

where T_C is the contour ordering operator and the average is performed over the interacting ground state, denoted by $|\rangle$. The above expression can be expanded to n-th order in the interaction Hamiltonian using

$$[G(\tau,\tau')]_{\sigma,\sigma'} = \sum_n \frac{(-i)^{n+1}}{n!}\int_C d\tau_1 ... \int_C d\tau_n \times \frac{{}_0\langle|T_C\{H_{e-sp}(\tau_1)...H_{e-sp}(\tau_n)c_\sigma(\tau)c^\dagger_{\sigma'}(\tau')\}|\rangle_0}{{}_0\langle|S(-\infty,\infty)|\rangle_0}, \tag{D.3}$$

where S is the time-evolution operator. Note that the average is now taken over the non-interacting ground state, $|\rangle_0$. The contour C goes from $-\infty$ to $+\infty$ and then back from $+\infty$ to $-\infty$. The first order term is a constant, while the second-order term reads

$$[G(\tau,\tau')]^{(2)}_{\sigma,\sigma'} = \frac{(-i)^3}{2!}J^2_{sd}\sum_{i,\alpha,\alpha',j,\beta,\beta'}\int_C d\tau_1\int_C d\tau_2 \times$$
$$ {}_0\langle|T_C\{c_\sigma(\tau)c^\dagger_\alpha(\tau_1)c_{\alpha'}(\tau_1)c^\dagger_\beta(\tau_2)c_{\beta'}(\tau_2)c^\dagger_{\sigma'}(\tau')\}|\rangle_0 {}_0\langle|T_C\{S^i(\tau_1)S^j(\tau_2)\}|\rangle_0[\sigma^i]_{\alpha\alpha'}[\sigma^j]_{\beta\beta'} \tag{D.4}$$

where the indices i and j run over the local spin operators. A contour ordered expansion is now performed on both the electron and spin brackets. For the electron part one obtains a total of six terms [64, 66].

Out of these six, two terms are Fock-like diagrams, while two Hartree-like terms are also obtained. The latter vanish due to spin selection rules. In addition one obtains two disconnected diagrams, which vanish under the averaging. The simplified expression then becomes

$$
\begin{aligned}
&{}_0\langle|T_C\{c_\sigma(\tau)c^\dagger_\alpha(\tau_1)c_{\alpha'}(\tau_1)c^\dagger_\beta(\tau_2)c_{\beta'}(\tau_2)c^\dagger_{\sigma'}(\tau')\}|\rangle_0 = \\
&2i^3\delta_{\sigma\alpha}\delta_{\alpha'\beta}\delta_{\beta'\sigma'}[G_0(\tau,\tau_1)]_{\sigma\sigma}[G_0(\tau_1,\tau_2)]_{\alpha'\alpha'}[G_0(\tau_2,\tau')]_{\sigma'\sigma'} \\
&+2i^3\delta_{\sigma\alpha}\delta_{\alpha'\sigma'}\delta_{\beta\beta'}[G_0(\tau,\tau_1)]_{\sigma\sigma}[G_0(\tau_1,\tau')]_{\sigma'\sigma'}[G_0(\tau_2,\tau_2)]_{\beta\beta}. \qquad \text{(D.5)}
\end{aligned}
$$

To expand the spin bracket consider the spin basis $|n\rangle$, where $n = -S, -S+1, ..., S-1, S$. These are used to rewrite the spin operators as

$$S^i(\tau) = \sum_{mn}\langle m|S^i|n\rangle d^\dagger_m(\tau)d_n(\tau), \qquad \text{(D.6)}$$

where $d^\dagger_n$ (d_n) creates (annihilates) a quasi-particle of the spin Hamiltonian. Considering only a single spin excitation at a time renders the choice of the quasi-particle statistics irrelevant. For simplicity, these operators are assumed to obey fermionic commutation relations. Now, the contour ordered Green's function for spin is defined to be

$$[D(\tau,\tau')]_{n,m} = -i\langle|T_C\{d_n(\tau)d^\dagger_m(\tau')\}|\rangle. \qquad \text{(D.7)}$$

By inserting the expressions for S^i and the spin propagator $D(\tau,\tau')$ into the spin bracket yields

$${}_0\langle|T_C\{S^i(\tau_1)S^j(\tau_2)\}|\rangle_0 = -\sum_{mn}\langle m|S^i|n\rangle\langle n|S^j|m\rangle[D_0(\tau_1,\tau_2)]_{n,n}[D_0(\tau_2,\tau_1)]_{m,m}, \qquad \text{(D.8)}$$

where D_0 is the unperturbed spin propagator. By using the two contributions from the electronic and spin brackets and the Dyson's equation, the second order contribution to the interacting self-energy can be written as

$$[\Sigma_{int}(\tau_1,\tau_2)]^{(2)}_{\sigma\sigma'} = -J_{sd}^2 \sum_{i,j,\beta} \{[\sigma^i]_{\sigma\beta}[\sigma^j]_{\beta\sigma'} + [\sigma^i]_{\sigma\sigma'}[\sigma^j]_{\beta\beta}\}$$
$$\times [G_0(\tau_1,\tau_2)]_{\beta\beta} \sum_{m,n} \langle m|S^i|n\rangle\langle n|S^j|m\rangle [D_0(\tau_1,\tau_2)]_{nn}[D_0(\tau_2,\tau_1)]_{mm}. \quad \text{(D.9)}$$

From the above expression the real-time quantities can be evaluated by using Langreth's rules. The final expressions read

$$[\Sigma^{\gtrless}_{int}(E)]^{(2)}_{\uparrow\uparrow} = -J_{sd}^2 \sum_{m,n} [G_0^{\gtrless}(E \pm \Omega_{mn})]_{\uparrow\uparrow}(\delta_{mn}\chi P_n S^z_{mn} + P_n(1-P_m)|S^z_{mn}|^2)$$
$$-J_{sd}^2 \sum_{m,n} [G_0^{\gtrless}(E \pm \Omega_{mn})]_{\downarrow\downarrow}] P_n(1-P_m)|S^+_{mn}|^2) \quad \text{(D.10)}$$

$$[\Sigma^{\gtrless}_{int}(E)]^{(2)}_{\downarrow\downarrow} = -J_{sd}^2 \sum_{m,n} [G_0^{\gtrless}(E \pm \Omega_{mn})]_{\downarrow\downarrow}(-\delta_{mn}\chi P_n S^z_{mn} + P_n(1-P_m)|S^z_{mn}|^2)$$
$$-J_{sd}^2 \sum_{m,n} [G_0^{\gtrless}(E \pm \Omega_{mn})]_{\uparrow\uparrow}] P_n(1-P_m)|S^-_{mn}|^2) \quad \text{(D.11)}$$

The unperturbed spin propagators $D_0^{\gtrless}(t_1,t_2)$ have been re-expressed in terms of the occupations of the spin levels, $P_n = d_n^\dagger d_n$. Here $\chi = \epsilon_0/J_{sd}$ and $S^\pm = S^x \pm iS^y$. The lesser (greater) self-energies describe the process where an incoming (outgoing) electron excites (relaxes) the spin system by an energy Ω_{mn} with spin level occupation dependent probabilities. Note the appearance of spin selection rules due to the factors of $S^\pm$ in the inelastic terms. The first term in both the expressions is the magnetoresistive elastic term and it preserves the electron spins during a scattering processes.

In order to calculate the non-equilibrium spin populations, consider first a non-interacting case when the conducting electrons do not interact with the local spins. Assume that the local spins are in equilibrium with a heat bath at temperature T, whose only effect is to generate a broadening k_BT to the spin eigenstates. The non-interacting spin propagator reads

$$[D_0^{\gtrless}(E)]_{m,n} = \frac{[\Pi_0^{\gtrless}(E)]_{m,n}}{(E-\epsilon_m)^2+(k_BT)^2}, \tag{D.12}$$

where $[\Pi_0^{>}]_{m,n} = \delta_{m,n}(1-P_m^0)k_BT$ and $[\Pi_0^{<}]_{m,n} = \delta_{m,n}P_m^0 k_BT$, and where P_m^0 is the ground state equilibrium population at zero temperature. Now, when the interaction is switched on, then from the first and second order contributions to the spin self-energy and using the equation of motion for the spin propagator, a master equation for the non-equilibrium populations can be derived as

$$\begin{aligned} \frac{dP_n}{dt} &= \frac{1}{\hbar}\sum_m \int_{-\infty}^{+\infty} dE\{[\Pi^{>}(E)]_{nm}[D_0^{<}(E)]_{mn} - [\Pi^{<}(E)]_{nm}[D_0^{>}(E)]_{mn}\}, \\ &= \frac{1}{\hbar}\sum_l [P_n(1-P_l)W_{ln} - P_l(1-P_n)W_{nl}] + (P_n^0 - P_n)k_BT, \end{aligned} \tag{D.13}$$

where the transition rates W_{nl} read

$$\begin{aligned} W_{nl} = -4\frac{(\rho J_{sd})^2}{\Gamma}\sum_{\eta\eta'}\zeta(\mu_\eta - \mu_{\eta'} + \Omega_{ln})\{\chi S_{nn}^z([\Gamma_\eta]_{\uparrow\uparrow}[\Gamma_{\eta'}]_{\uparrow\uparrow} - [\Gamma_\eta]_{\downarrow\downarrow}[\Gamma_{\eta'}]_{\downarrow\downarrow}) \\ +|S_{nl}^z|^2([\Gamma_\eta]_{\uparrow\uparrow}[\Gamma_{\eta'}]_{\uparrow\uparrow} + [\Gamma_\eta]_{\downarrow\downarrow}[\Gamma_{\eta'}]_{\downarrow\downarrow}) + |S_{nl}^+|^2[\Gamma_\eta]_{\downarrow\downarrow}[\Gamma_{\eta'}]_{\uparrow\uparrow} + |S_{nl}^-|^2[\Gamma_\eta]_{\uparrow\uparrow}[\Gamma_{\eta'}]_{\downarrow\downarrow}\} \end{aligned} \tag{D.14}$$

where $\zeta(x) = x/(1-e^{-x/k_BT})$, μ_η is the chemical potential in lead η and Γ_η is the broadening function of lead η.

Appendix E

A brief note on the Coherent Potential Approximation

The Coherent Potential Approximation (CPA) is widely used to study the electronic structure of alloys [135]. In this Appendix we outline the basic idea behind the CPA by using a single orbital tight-binding model for illustration. We closely follow the exposition by Mookerjee in Ref. [144]. We begin with a tight-binding Hamiltonian of the form

$$H = \sum_i \epsilon_i |i\rangle\langle i| + \sum_{ij} t_{ij} |i\rangle\langle j|, \tag{E.1}$$

with the onsite energy ϵ_i at site i and the hopping elements between sites i and j as t_{ij}. If ϵ_i are random, then the simplest approximation is to consider just the average value of the onsite energy $\langle\epsilon_i\rangle$, and replace it in the averaged Hamiltonian. This is the Virtual Crystal Approximation (VCA), and it clearly misses out on the random potential fluctuations around the average. One can go a step ahead and consider the Coherent Potential Approximation (CPA) as done by Soven [135]. The basic idea is to look for an effective Hamiltonian H^{eff} with the same translational symmetries as the underlying lattice and whose corresponding Green's function $G^{\text{eff}}(z) = (z - H^{\text{eff}})^{-1}$ is a good approximation to the average Green's function of the random Hamiltonian. For the above tight-binding model the effective Hamiltonian is of the form

$$H^{\text{eff}}_{ij} = \sum_i E(z)|i\rangle\langle i| + \sum_{ij} t_{ij}|i\rangle\langle j|. \tag{E.2}$$

From definition of CPA we have

$$\langle G(z)\rangle = G^{\text{eff}}(z), \tag{E.3}$$

One can write $E(z) = \langle\epsilon\rangle + \Sigma(z)$, and then the self-energy $\Sigma(z)$ is the correction to the virtual crystal approximation. In order to find $E(z)$, at site j replace the effective potential by the exact random potential ϵ_j. Then the Hamiltonian of the system is

$$H^{(j)} = H^{\text{eff}} + [\epsilon_j - E(z)]|j\rangle\langle j|. \tag{E.4}$$

From the above equation we have

$$G^{(j)}_{jj}(z) = \frac{G^{\text{eff}}_{jj}}{1 - [\epsilon_j - E(z)]G^{\text{eff}}_{jj}}. \tag{E.5}$$

For the CPA one needs to choose $E(z)$ such that it satisfies

$$\langle G^{(j)}(z)\rangle = G^{\text{eff}}(z), \tag{E.6}$$

which translates to

$$\left\langle \frac{\epsilon_j - E(z)}{1 - [\epsilon_j - E(z)]\langle G_{jj}(z)\rangle} \right\rangle = 0. \tag{E.7}$$

In the special case when ϵ_j has a binary distribution (i.e. for a binary alloy system) with onsite energies being ϵ_A or ϵ_B with probabilities x and y ($x+y=1$), respectively, we have

$$\Sigma(z) = \frac{xy(\epsilon_A - \epsilon_B)^2 \langle G_{jj}(z) \rangle}{1 - [\overline{\epsilon} - \Sigma(z)]\langle G_{jj}(z) \rangle}, \tag{E.8}$$

where $\overline{\epsilon} = y\epsilon_A + x\epsilon_B$. This is the self-consistent equation for the CPA self-energy, which needs to be iterated till self-consistency is reached. In the preceding discussion we outlined the application of CPA to the case of diagonal disorder. In fact CPA has been generalized to treat off-diagonal disorder in an analogous way [145]. This allows one to replace the hopping matrix by an effective CPA medium in a manner closely resembling the approach for the onsite term.

Appendix F

Publications stemming from this work

- Awadhesh Narayan and Stefano Sanvito, *Andreev reflection in two-dimensional topological insulators with either conserved or broken time-reversal symmetry*, Phys. Rev. B **86**, 041104(R) (2012).
- Awadhesh Narayan, Ivan Rungger, and Stefano Sanvito, *Topological surface states scattering in Antimony*, Phys. Rev. B **86**, 201402(R) (2012).
- Aaron Hurley, Awadhesh Narayan, and Stefano Sanvito, *Spin-pumping and inelastic electron tunneling spectroscopy in topological insulators*, Phys. Rev. B **87**, 245410 (2013).
- Awadhesh Narayan, Aaron Hurley, and Stefano Sanvito, *Gate controlled spin pumping at a quantum spin Hall edge*, Appl. Phys. Lett. **103**, 142407 (2013).
- Awadhesh Narayan and Stefano Sanvito, *Multiprobe quantum spin Hall bars*, Eur. Phys. J. B **87**: 43 (2014).
- Kapildeb Dolui, Awadhesh Narayan, Ivan Rungger, and Stefano Sanvito, *Efficient spin injection and giant magnetoresistance in Fe/MoS$_2$/Fe junc-*

tions, Phys. Rev. B **90**, 041401(R) (2014).

- Igor Popov, Mauro Mantega, Awadhesh Narayan, and Stefano Sanvito, *Proximity induced topological state in graphene*, Phys. Rev. B **90**, 035418 (2014).
- Awadhesh Narayan, Ivan Rungger, Andrea Droghetti, and Stefano Sanvito, *Ab-initio transport across bismuth selenide surface barriers*, Phys. Rev. B **90**, 205431 (2014).
- Awadhesh Narayan, Domenico Di Sante, Silvia Picozzi, and Stefano Sanvito, *Topological tuning in three-dimensional Dirac semimetals*, Phys. Rev. Lett. in press, (arXiv:1408.3509).
- Awadhesh Narayan, Ivan Rungger, and Stefano Sanvito, *Single atom anisotropic magnetoresistance on topological insulator surface*, submitted to New J. Phys., (arXiv:1405.2651).
- Awadhesh Narayan, Ivan Rungger, and Stefano Sanvito, *Phenomenology of Andreev reflection from first-principles transport theory*, submitted to Phys. Rev. B, (arXiv:1410.7178).
- S. Jakobs, A. Narayan, B. Stadtmueller, A. Droghetti, I. Rungger, Y.S. Hor, S. Klyatskaya, D. Jungkenn, J. Stoeckl, M. Laux, O.L.A. Monti, M. Aeschlimann, R.J. Cava, M. Ruben, S. Mathias, S. Sanvito, and M. Cinchetti, *Controlling the spin-texture of topological insulators with organic molecules*, submitted to Science.
- Andrea Droghetti, Awadhesh Narayan, Stefano Sanvito, and Ivan Rungger, *Correlated zero bias transport in graphene and 2D topological insulators nanostructures* (in preparation).
- Ivan Rungger, Awadhesh Narayan, Udo Schwingenschloegl, and Stefano Sanvito, *Scattering channel analysis of topological surface states* (in preparation).

Bibliography

[1] P.W. Anderson, *Basic Notions of Condensed Matter Physics* (Advanced Book Program, Addison-Wesley, Massachussets 1997).

[2] K. von Klitzing, G. Dorda and M. Pepper, Phys. Rev. Lett. **45**, 494 (1980).

[3] M.Z. Hasan and C.L. Kane, Rev. Mod. Phys. **82**, 3045 (2010).

[4] X.-L. Qi and S.-C. Zhang, Rev. Mod. Phys. **83**, 1057 (2011).

[5] M.Z. Hasan and J.E. Moore, Annual Review of Condensed Matter Physics **2**, 55 (2011).

[6] C.Z. Chang *et al.*, Science **340**, 167 (2013).

[7] B.A. Bernevig, T.L. Hughes and S.C. Zhang, Science **314**, 1757 (2006).

[8] M. König, S. Wiedmann, C. Brüne, A. Roth, H. Buhmann, L.W. Molenkamp, X.L. Qi and S.C. Zhang, Science **318**, 766 (2007).

[9] C.-C. Liu, W. Feng and Y. Yao, Phys. Rev. Lett. **107**, 076802 (2011).

[10] Y. Xu, B. Yan, H.-J. Zhang, J. Wang, G. Xu, P. Tang, W. Duan and S.-C. Zhang, Phys. Rev. Lett. **111**, 136804 (2013).

[11] D. Hsieh, D. Qian, L. Wray, Y. Xia, Y.S. Hor, R.J. Cava and M.Z. Hasan, Nature **452**, 970 (2008).

[12] L. Fu and C.L. Kane, Phys. Rev. B **76** 045302 (2007).

[13] J.C.Y. Teo, L. Fu and C.L. Kane, Phys. Rev. B **78** 045426 (2008).

[14] H. Zhang, C.-X. Liu, X.-L. Qi, X. Dai, Z. Fang, and S.-C. Zhang, Nat. Phys. **5**, 438 (2009).

[15] Y. Xia, D. Qian, D. Hsieh, L. Wray, A. Pal, H. Lin, A. Bansil, D. Grauer, Y.S. Hor, R.J. Cava, and M.Z. Hasan, Nat. Phys. **5**, 398 (2009).

[16] P. Roushan, J. Seo, C.V. Parker, Y.S. Hor, D. Hsieh, D. Qian, A. Richardella, M.Z. Hasan, R.J. Cava, and A. Yazdani, Nature **460**, 1106 (2007).

[17] J. Seo, P. Roushan, H. Beidenkopf, Y.S. Hor, R.J. Cava and A. Yazdani, Nature **466**, 343 (2010).

[18] B.A. Bernevig and T.L. Hughes, *Topological Insulators and Topological Superconductors* (Princeton University Press, Princeton 2013).

[19] S.-Q. Shen, *Topological Insulators: Dirac Equation in Condensed Matters* (Springer, Heidelberg 2012).

[20] M.V. Berry, Proc. R. Soc. Lond. A **392** 45, 1984.

[21] W.P. Su, J.R. Schrieffer, and A.J. Heeger, Phys. Rev. Lett. **42**, 1698 (1979).

[22] R. Jackiw and C. Rebbi, Phys. Rev. D **13**, 3398 (1976).

[23] R.D. King-Smith and D. Vanderbilt, Phys. Rev. B **47**, 1651 (1993).

[24] R. Resta, Europhys. Lett. **22**, 133 (1993).

[25] L. Fu and C.L. Kane, Phys. Rev. B **74**, 195312 (2006).

[26] L. Fu and C.L. Kane, Phys. Rev. B **76**, 045302 (2007).

[27] C.L. Kane and E.J. Mele, Phys. Rev. Lett. **95**, 146802 (2005).

[28] C.L. Kane and E.J. Mele, Phys. Rev. Lett. **95**, 226801 (2005).

[29] L. Fu, C.L. Kane and E.J. Mele, Phys. Rev. Lett. **98**, 106803 (2007).

[30] K. Capelle, arXiv:cond-mat/0211443.

[31] R.M. Martin, *Electronic Structure: Basic Theory and Practical Methods* (Cambridge University Press, Cambridge, 2004).

[32] C. Fiolhais, F. Nogueira, and M. Marques, *A Primer in Density Functional Theory* (Springer, Heidelberg, 2003).

[33] D.M. Cepereley and B.J. Alder, Phys. Rev. Lett. **45**, 566 (1980).

[34] S. Datta, *Electronic Transport in Mesoscopic Systems* (Cambridge University Press, Cambridge, 1997)

[35] I. Rungger, (2008), *Computational methods for electron transport and their application in nanodevices*, PhD thesis, Trinity College Dublin.

[36] L.I. Schiff, *Quantum Mechanics*, McGraw-Hill (1968).

[37] C. Li, A.J. Freeman, H.J.F. Jansen and C.L. Fu, Phys. Rev. B **42**, 5433 (1990).

[38] L. Fernández-Seivane, M.A. Oliveira, S. Sanvito and J. Ferrer, J. Phys.:Condens. Matter **18**, 7999 (2006).

[39] L. Kleinman, Phys. Rev. B **21**, 2630 (1980).

[40] F. Schwabl, *Quantum Mechanics*, Springer, Berlin, (2002).

[41] A.F. Andreev, Sov. Phys. JETP **19**, 1228 (1964).

[42] R.J. Soulen *et al.*, Science **282**, 85 (1998).

[43] P. Adroguer, C. Grenier, D. Carpentier, J. Cayssol, P. Degiovanni and E. Orignac, Phys. Rev. B **82**, 081303(R) (2010).

[44] A.M. Black-Schaffer, Phys. Rev. B **83**, 060504(R) (2011).

[45] Y. Tanaka, T. Yokoyama and N. Nagaosa, Phys. Rev. Lett. **103**, 107002 (2009).

[46] L. Fu and C.L. Kane, Phys. Rev. Lett. **100**, 096407 (2008).

[47] G.E. Blonder, M. Tinkham, and T.M. Klapwijk, Phys. Rev. B. **25**, 4515 (1982).

[48] M. Tinkham, *Introduction to Superconductivity* (Dover, New York, 2004).

[49] F.D.M. Haldane, Phys. Rev. Lett. **61**, 2015 (1988).

[50] T.-W. Chen, Z.-R. Xiao, D.-W. Chiou and G.-Y. Guo, Phys. Rev. B **84**, 165453 (2011).

[51] M. Büttiker, Phys. Rev. B. **38**, 9375 (1988).

[52] R.G. Mojarad and S. Datta, Phys. Rev. B **75**, 081301(R) (2007).

[53] Q.-F. Sun, Y.-X. Li, W. Long and J. Wang, Phys. Rev. B **83**, 115315 (2011).

[54] I. Knez, R.R. Du and G. Sullivan, arXiv:1106.5819v1 (unpublished).

[55] M. Büttiker, Phys. Rev. Lett. **65**, 2901 (1990).

[56] Q. Liu, C.-X. Liu, C. Xu, X.-L. Qi and S.-C. Zhang, Phys. Rev. Lett. **102**, 156603 (2009).

[57] Y. Yang, Z. Xu, L. Sheng, B. Wang, D.Y. Xing and D.N. Sheng, Phys. Rev. Lett. **107**, 066602 (2011).

[58] D.D. Awschalom, J. Warnock and S. von Molnár, Phys. Rev. Lett. **58**, 812 (1987).

[59] C.-X. Liu, X.-L. Qi, X. Dai, Z. Fang and S.C. Zhang, Phys. Rev. Lett. **101**, 146802 (2008).

[60] A.M. Lunde and G. Platero, Phys. Rev. B **86**, 035112 (2012).

[61] A.J. Heinrich, J.A. Gupta, C.P. Lutz and D.M. Eigler, Science **306**, 466 (2004).

[62] S. Loth, K. von Bergmann, M. Ternes, A.F. Otte, C.P. Lutz and A.J. Heinrich, Nature Physics **6**, 340 (2010).

[63] J. Maciejko, Phys. Rev. B **85**, 245108 (2012).

[64] A. Hurley, N. Baadji and S. Sanvito, Phys. Rev. B **84**, 035427 (2011).

[65] A. Hurley, N. Baadji and S. Sanvito, Phys. Rev. B **84**, 115435 (2011).

[66] A. Hurley, N. Baadji and S. Sanvito, Phys. Rev. B **86**, 125411 (2012).

[67] G.D. Mahan, *Many-Particle Physics*, (Plenum Press, New York, 1990).

[68] K. Yosida, *Theory of Magnetism* (Springer-Verlag, Berlin, 1998)

[69] M. Buttiker, Phys. Rev. B **38**, 9375 (1988).

[70] L. Sheng, D.N. Sheng, C.S. Ting, and F.D.M. Haldane, Phys. Rev. Lett **95**, 136602 (2005).

[71] F. Delgado and J. Fernandez-Rossier, Phys. Rev. B **82**, 134414 (2010).

[72] A. Narayan and S. Sanvito, Phys. Rev. B **86**, 041104(R) (2012).

[73] A. Hurley, A. Narayan, and S. Sanvito, Phys. Rev. B **87**, 245410 (2013).

[74] D. Pesin and A.H. MacDonald, Nat. Mater. **11**, 409 (2012).

[75] D. Hsieh, Y. Xia, L. Wray, D. Qian, A. Pal, J.H. Dil, J. Osterwalder, F. Meier, G. Bihlmayer, C.L. Kane, Y.S. Hor, R.J. Cava and M.Z. Hasan, Science **323**, 919 (2009).

[76] J.M. Soler, E. Artacho, J.D. Gale, A. Garcia, J. Junquera, P. Ordejón and D. Sánchez-Portal, J. Phys.:Condens. Matter **14**, 2745 (2002).

[77] A. R. Rocha, V. M. Garcia-Suarez, S. Bailey, C. Lambert, J. Ferrer, and S. Sanvito, Nat. Mater. **4**, 335 (2005).

[78] A. R. Rocha, V. M. Garcia-Suarez, S. Bailey, C. Lambert, J. Ferrer, and S. Sanvito, Phys. Rev. B **73**, 085414 (2006).

[79] I. Rungger and S. Sanvito, Phys. Rev. B **78**, 035407 (2008).

[80] B. Naydenov, M. Mantega, I. Rungger, S. Sanvito and J.J. Boland, Phys. Rev. B **84**, 195321 (2011).

[81] G. Kresse and J. Furthmuller, Phys. Rev. B **54**, 11169 (1996).

[82] S.-X. Wang, P. Zhang and S.-S. Li, arXiv:1201.1976.

[83] P.-F. Zhang, W. Duan, J. Wu and Z. Liu, Phys. Rev. B **85**, 201410(R) (2012).

[84] K. Sugawara, T. Sato, S. Souma, T. Takahashi, M. Arai and T. Sasaki, Phys. Rev. Lett. **96**, 046411 (2006).

[85] G. Bian, X. Wang, Y. Liu, T. Miller and T.-C. Chiang, Phys. Rev. Lett. **108**, 176401 (2012).

[86] K.K. Gomes, W. Ko, W. Mar, Y. Chen, Z.-X. Shen and H.C. Manoharan, arXiv:0909.0921.

[87] Y. Takane and K.-I. Imura, J. Phys. Soc. Jpn. **81**, 093705 (2012).

[88] H. Beidenkopf, P. Roushan, J. Seo, L. Gorman, I. Drozdov, Y.S. Hor, R.J. Cava, and A. Yazdani, Nat. Phys. **7**, 939 (2011).

[89] J. Wang, W. Li, P. Cheng, C. Song, T. Zhang, P. Deng, X. Chen, X. Ma, K. He, J.-F. Jia, Q.-K. Xue, and B.-F. Zhu, Phys. Rev. B **84**, 235447 (2011).

[90] Z. Alpichshev, R.R. Biswas, A.V. Balatsky, J.G. Analytis, J.-H. Chu, I.R. Fisher, and A. Kapitulnik, Phys. Rev. Lett. **108**, 206402 (2012).

[91] S. Kim, M. Ye, K. Kuroda, Y. Yamada, E.E. Krasovskii, E.V. Chulkov, K. Miyamoto, M. Nakatake, T. Okuda, Y. Ueda, K. Shimada, H. Namatame, M. Taniguchi, and A. Kimura, Phys. Rev. Lett. **107**, 056803 (2011).

[92] T. Zhang, P. Cheng, X. Chen, J.-F. Jia, X. Ma, K. He, L. Wang, H. Zhang, X. Dai, Z. Fang, X. Xie, and Q.-K. Xue, Phys. Rev. Lett. **103**, 266803 (2009).

[93] Z. Alpichshev, J.G. Analytis, J.-H. Chu, I.R. Fisher, Y.L. Chen, Z.X. Shen, A. Fang, and A. Kapitulnik, Phys. Rev. Lett. **104**, 016401 (2010).

[94] Z. Alpichshev, J.G. Analytis, J.-H. Chu, I.R. Fisher, and A. Kapitulnik, Phys. Rev. B **84**, 041104(R) (2011).

[95] X. Zhou, C. Fang, W.-F. Tsai, and J. Hu, Phys. Rev. B **80**, 245317 (2009).

[96] R.R. Biswas and A.V. Balatsky, Phys. Rev. B **83**, 075439 (2011).

[97] R.R. Biswas and A.V. Balatsky, Phys. Rev. B **81**, 233405 (2010).

[98] X.-F. Wang, Y. Hu, and H. Guo, Phys. Rev. B **85**, 241402(R) (2012).

[99] M.I. Katsnelson, K.S. Novoselov, and A.K. Geim, Nat. Phys. **2**, 620 (2006).

[100] I. A. Nechaev, M. F. Jensen, E. D. L. Rienks, V. M. Silkin, P. M. Echenique, E. V. Chulkov, and Ph. Hofmann. Phys. Rev. B **80**, 113402 (2009).

[101] M.F. Crommie, C.P. Lutz, and D.M. Eigler, Nature **363**, 524 (1993).

[102] M.L. Teague, H. Chu, F.-X. Xiu, L. He, K.-L. Wang, and N.-C. Yeh, Solid State Communications **152**, 747 (2012).

[103] A. Narayan, I. Rungger, and S. Sanvito, Phys. Rev. B **86**, 201402(R) (2012).

[104] A. Kokalj, Comp. Mater. Sci., **28**, 155 (2003).

[105] A. Burkov and D.G. Hawthorn, Phys. Rev. Lett. **105**, 066802 (2010).

[106] T. Yokoyama, Y. Tanaka, and N. Nagaosa, Phys. Rev. B **81**, 121401(R) (2010).

[107] L.B. Abdalla, L. Seixas, T.M. Schmidt, R.H. Miwa, and A. Fazzio, Phys. Rev. B **88**, 045312 (2013).

[108] J. Honolka, A.A. Khajetoorians, V. Sessi, T.O. Wehling, S. Stepanow, J.-L. Mi, B.B. Iversen, T. Schlenk, J. Wiebe, N.B. Brookes, A.I. Lichtenstein, Ph. Hofmann, K. Kern, and R. Wiesendanger, Phys. Rev. Lett. **108**, 256811 (2012).

[109] T. Schlenk, M. Bianchi, M. Koleini, A. Eich, O. Pietzsch, T.O. Wehling, T. Frauenheim, A. Balatsky, J.-L. Mi, B.B. Iversen, J. Wiebe, A.A. Khajetoorians, Ph. Hofmann, and R. Wiesendanger, Phys. Rev. Lett. **110**, 126804 (2013).

[110] Y. Okada, C. Dhital, W. Zhou, E.D. Huemiller, H. Lin, S. Basak, A. Bansil, Y.-B. Huang, H. Ding, Z. Wang, S.D. Wilson, and V. Madhavan, Phys. Rev. Lett. **106**, 206805 (2011).

[111] I. Rungger, A. Narayan, U. Schwingenschlögl, and S. Sanvito, (in preparation).

[112] A. Narayan, I. Rungger, A. Droghetti, and S. Sanvito, arXiv:1403.2607.

[113] C.F. Hirjibehedin, C.P. Lutz, and A.J. Heinrich, Science **312**, 1021 (2006).

[114] G. Wu, H. Chen, Y. Sun, X. Li, P. Cui, C. Franchini, J. Wang, X.-Q. Chen, and Z. Zhang, Sci. Rep. **3**, 1233 (2013).

[115] Y.-M. Lin *et al.*, Science **332**, 1294 (2011).

[116] C. Weeks, J. Hu, J. Alicea, M. Franz and R. Wu, Phys. Rev. X **1**, 021001 (2011).

[117] W. Dang, H. Peng, H. Li, P. Wang, and Z. Liu, Nano Lett. **10**, 2870 (2010).

[118] C.-L. Song, Y.-L. Wang, Y.-P. Jiang, Y. Zhang, C.-Z. Chang, L. Wang, K. He, X. Chen, J.-F. Jia, Y. Wang *et al.*, Appl. Phys. Lett. **97**, 143118 (2010).

[119] Y. Jiang, Y. Sun, M. Chen, Y. Wang, Z. Li, C. Song, K. He, L. Wang, X. Chen, Q.-K. Xue *et al.*, Phys. Rev. Lett. **108**, 066809 (2012).

[120] M. Vozmediano, M. Katsnelson, and F. Guinea, Phys. Rep. **496**, 109 (2010).

[121] Q. Zhang, Z. Zhang, Z. Zhu, U. Schwingenschloegl, and Y. Cui, ACS Nano **6**, 2345 (2012).

[122] A.W. Robertson, C. Allen, Y. Wu, K. He, J. Olivier, J. Neethling, A. Kirkland, and J. Warner, Nature Comm. **3**, 1144 (2012).

[123] M. Dion, H. Rydberg, E. Schroeder, D.C. Langreth, and B.I. Lundqvist, Phys. Rev. Lett. **92**, 246401 (2004).

[124] G. Cunningham, M. Lotya, C. Cucinotta, S. Sanvito, S. Bergin, R. Menzel, M. Shaffer, and J.N. Coleman, ACS Nano **6**, 3468 (2012).

[125] S.M. Young, S. Zaheer, J.C.Y. Teo, C.L. Kane, E.J. Mele, and A.M. Rappe, Phys. Rev. Lett. **108**, 140405 (2012).

[126] Z. Wang, Y. Sun, X.-Q. Chen, C. Franchini, G. Xu, H. Weng, X. Dai, and Z. Fang, Phys. Rev. B **85**, 195320 (2012).

[127] Z. Wang, H. Weng, Q. Wu, X. Dai, and Z. Fang, Phys. Rev. B **88**, 125427 (2013).

[128] Z.K. Liu, B. Zhou, Y. Zhang, Z.J. Wang, H.M. Weng, D. Prabhakaran, S.-K. Mo, Z.X. Shen, Z. Fang, X. Dai, Z. Hussain, and Y.L. Chen, Science **343**, 864 (2014).

[129] S.-Y. Xu, C. Liu, S.K. Kushwaha, T.-R. Chang, J.W. Krizan, R. Sankar, C.M. Polley, J. Adell, T. Balasubramanian, K. Miyamoto, N. Alidoust, G. Bian, M. Neupane, I. Belopolski, H.-T. Jeng, C.-Y. Huang, W.-F. Tsai, H. Lin, F.C. Chou, T. Okuda, A. Bansil, R.J. Cava, and M.Z. Hasan, arXiv:1312.7624.

[130] Z.K. Liu, J. Jiang, B. Zhou, Z.J. Wang, Y. Zhang, H.M. Weng, D. Prabhakaran, S.-K. Mo, H. Peng, P. Dudin, T. Kim, M. Hoesch, Z. Fang, X. Dai, Z.X. Shen, D.L. Feng, Z. Hussain, and Y.L. Chen, Nature Mat. **13**, 677 (2014).

[131] M. Neupane, S.-Y. Xu, R. Sankar, N. Alidoust, G. Bian, C. Liu, I. Belopolski, T.-R. Chang, H.-T. Jeng, H. Lin, A. Bansil, F.C. Chou, and M.Z. Hasan, Nature Commun. **5**, 3786 (2014).

[132] S. Borisenko, Q. Gibson, D. Evtushinsky, V. Zabolotnyy, B. Buchner, and R.J. Cava, Phys. Rev. Lett. **113**, 027603 (2014).

[133] M. Orlita, D.M. Basko, M.S. Zholudev, F. Teppe, W. Knap, V.I. Gavrilenko, N.N. Mikhailov, S.A. Dvoretskii, P. Neugebauer, C. Faugeras, A-L. Barra, G. Martinez, and M. Potemski, Nature Phys. **10**, 233 (2014).

[134] A. A. Mostofi, J. R. Yates, Y.-S. Lee, I. Souza, D. Vanderbilt and N. Marzari, Comput. Phys. Commun. **178**, 685 (2008).

[135] P. Soven, Phys. Rev. **156**, 809 (1967).

[136] D. Di Sante, P. Barone, E. Plekhanov, S. Ciuchi, and S. Picozzi, arXiv:1407.2064.

[137] Y. Zhang *et al.*, Nature Phys. **6**, 584 (2010).

[138] M. Neupane *et al.*, Nature Commun. **5**, 3841 (2014).

[139] Y. Zhang *et al.*, Appl. Phys. Lett. **105**, 031901 (2014).

[140] S.-Y. Xu, Y. Xia, L.A. Wray, S. Jia, F. Meier, J.H. Dil, J. Osterwalder, B. Slomski, A. Bansil, H. Lin, R.J. Cava, and M.Z. Hasan, Science **332**, 560 (2011).

[141] T. Sato, K. Segawa, K. Kosaka, S. Souma, K. Nakayama, K. Eto, T. Minami, Y. Ando, and T. Takahashi, Nature Phys. **7**, 840 (2011).

[142] P. Dziawa *et al.*, Nature Mater. **11**, 1023 (2012).

[143] S.-Y. Xu *et al.*, Nature Commun. **3**, 1192 (2012).

[144] A. Mookerjee, Chapter 3, *Introduction to augmented space methods*, in A. Mookerjee and D.D. Sarma (eds.) *Electronic Structure of Alloys, Surfaces and Interfaces*, (Taylor and Francis, London 2003).

[145] J.A. Blackman, D.M. Esterling, and N.F. Berk, Phys. Rev. B **4**, 2412 (1971).